2016

CHANNEL MODELING FOR FIFTH GENERATION CELLULAR NETWORKS AND WIRELESS SENSOR NETWORKS

Amir Torabi
Michigan Technological University, atorabi@mtu.edu

CHANNEL MODELING FOR FIFTH GENERATION CELLULAR NETWORKS AND WIRELESS SENSOR NETWORKS

By

Amir Torabi

A DISSERTATION

Submitted in partial fulfillment of the requirements for the degree of

DOCTOR OF PHILOSOPHY

In Electrical Engineering

MICHIGAN TECHNOLOGICAL UNIVERSITY

2016

This dissertation has been approved in partial fulfillment of the requirements for the Degree of DOCTOR OF PHILOSOPHY in Electrical Engineering.

Department of Electrical and Computer Engineering

Dissertation Advisor:	*Dr. Seyed A. (Reza) Zekavat*
Committee Member:	*Dr. Ossama Abdelkhalik*
Committee Member:	*Dr. Michael C. Roggemann*
Committee Member:	*Dr. Timothy J. Schulz*
Department Chair:	*Dr. Daniel R. Fuhrmann*

Dedication

For my parents *Hasan* and *Tahereh*

Contents

List of Figures . . . . . **xi**

List of Tables . . . . . **xvii**

Acknowledgments . . . . . **xix**

Abstract . . . . . **xxi**

1 Introduction **1**

1.1 Motivation 1

1.2 Channel modeling for near-ground wireless sensor networks 6

1.3 Channel modeling for fifth generation (5G) cellular networks 8

1.4 Overview of dissertation 11

2 Near-Ground Channel Modeling for Wireless Sensor Networks . **15**

2.1 Introduction 15

2.2 Derivation of the break points 20

2.3 Near-ground path loss model 27

2.3.1 Short-range communication 27

2.3.2 Medium-range communication 28
2.3.3 Long-range communication 32
2.3.4 Added features in urban settings 34
2.3.5 Foliage loss 35
2.4 Model validation and WSN connectivity analysis 36
2.4.1 Model validation and discussion 37
2.4.2 Connectivity in near-ground WSNs 41
2.5 Conclusion 47

3 Multiuser MIMO Channel Characterization over Random Rough Dielectric Terrain 49

3.1 Introduction 49
3.2 Mobile channel characterization 54
3.2.1 Small perturbation scattering model 54
3.2.2 Kirchhoff approximation 58
3.2.3 Ray tracing simulations 61
3.2.4 Soil parameters 63
3.3 Results and discussion 66
3.4 Conclusion 76

4 Millimeter Wave Directional Channel Modeling for Small Cells 81

4.1 Introduction 81
4.2 Problem definition 84

4.2.1 Geometry 84
4.2.2 Ray tracing algorithm 86
4.2.3 LOS and NLOS channel matrices 88
4.3 Theoretical evaluation 92
4.4 Numerical results and discussion 101
4.5 Conclusion 111

5 Conclusion and Future Work 113
5.1 Conclusion 113
5.2 Future work 117
5.2.1 Channel modeling for wireless sensor networks in layered media with rough boundaries 117
5.2.2 Channel modeling for WSN in inhomogeneous media with volumetric stratification 118

References 121

List of Figures

1.1 Schematic representation of a MIMO channel. 2

1.2 Delay spread in a multipath channel. 5

1.3 Frequency flat versus frequency selective channels. 5

1.4 Near-ground sensor networks have many applications such as environmental monitoring, planetary explorations, disaster relief operations, and battlefield surveillance. 6

1.5 Impact of wireless channel modeling on wireless radio design. 7

2.1 Family of Fresnel zones. An imaginary plane perpendicular to the LOS cuts the successive Fresnel ellipsoids in concentric circles. 20

2.2 Schematic representation of the first Fresnel zone and the diffraction zone in a radio link as the distance between two terminals increases. (a) First Fresnel zone is clear of obstructions; (b) First Fresnel zone touches the ground surface; (c) Diffraction zone is tangent to the ground surface. 21

2.3 Path loss versus terminal separation for free space model and two-ray model. Depiction of the break distance and dual-slope piece-wise linear regression fit in a microcellular propagation scenario assuming a flat perfectly conducting ground plane. 22

2.4 Comparison of the near-ground models predictions with measured data in open area. (a) Stationary measurements at distance of 75 m at 300 MHz ([42], Figure 12). Plots for h_t=0.87 m, h_t=1.15 m, and h_t=1.55 m are offset by 30 dB, 20 dB, and 10 dB, respectively, for illustration purposes; (b) Measurements at 868 MHz recorded in three diverse open environments ([31], Table 1). 39

2.5 Model predictions versus measured path loss along an L-shaped urban route at 225 MHz ([43], Figures 5-7). Plots for d_L=265 m and d_L=132 m are offset by 10 dB and 20 dB, respectively, for illustration purposes. 40

2.6 Measured and predicted path loss in forested areas. (a) h_a=0.75 m, f=300 MHz ([42], Figure 10(a)); (b) h_a=2.15 m, f=240 MHz ([34], Figure 4(a)); (c) h_a=2.15 m, f=700 MHz ([34], Figure 4(b)). 42

2.7 Mote transmission range: (a) versus antennas height using different models; (b) versus antennas height at different frequencies; (c) versus VWC over flat and rough ground. 44

2.8 Average number of neighbors for a 100-node network with uniform topology: (a) versus antennas height using different models; (b) versus antennas height at different frequencies; (c) versus VWC over flat and rough ground. 46

3.1 Basic geometry of scattering at a 2-D dielectric rough surface. . . . 54

3.2 Calculation of geometric parameters of each scattering tile such as the center point location, distance from Tx/Rx, and incidence/emergence angles. 63

3.3 (a) Scattered power versus sand (clay) fraction; (b) Scattered power versus volumetric moisture content. 67

3.4 (a) Normalized relative received power versus the excess delay for different correlation distances and undulation heights; (b) Power azimuth spectrum for various correlation distances and surface roughness heights. 69

3.5 Impact of TRx position on azimuth angular spread. (a) Simulation setup; (b) $m_v = 5\%$; (c) $m_v = 30\%$. 71

3.6 Impact of Rx height on azimuth angular spread. (a) Simulation setup; (b) $m_v = 5\%$; (c) $m_v = 30\%$. 73

3.7 Path loss versus terminal separation for directional and isotropic antennas. (a) Effect of carrier frequency; (b) effect of polarization; (c) effect of base station height. 78

3.8 The sequence of NLOS PDPs (in dBm) versus the range. First columns represent the specularly reflected power. (a) Reference plot: TE polarization, $f_c = 2.6GHz$, $h_t = 20m$; (b) frequency reduced to $f_c = 300MHz$; (c) Base station height is lowered to $h_t = 10m$; (d) TM polarization. Note the Brewster effect along the specular reflection. 79

3.9 NLOS RMS DS versus range for various antenna directionalities and polarizations. (a) At different carrier frequencies; (b) for different Tx heights. 80

4.1 Outdoor small cell scenario. 85

4.2 Scattering from a rough ground. (a) Comparison of reflected and scattered power; (b) scattered power versus surface roughness height. . 85

4.3 Schematic implementation of Kirchhoff formulation in a ray-tracing model. 88

4.4 Basic geometric notations for incidence and emergence angles from a scattering tile. 92

4.5 Path loss versus range: (a) directional antennas compared to isotropic radiators; (b) effect of increasing the carrier frequency 10 fold. Black lines present the local average of the received power. 103

4.6 Coverage range versus combined antenna gains. (a) Coverage range at different mmW frequencies; (b) coverage range for various values of Rician K parameter. 104

4.7 Azimuth correlation versus inter-element spacing. (a,b) correlation at different frequencies; (c,d) correlation at different ranges; (e,f) correlation for different antenna polarizations in the presence and absence of a LOS component. 107

4.8 Elevation correlation versus inter-element spacing. (a,b) correlation at different frequencies; (c,d) correlation at different ranges; (e,f) correlation for different antenna polarizations in the presence and absence of a LOS component. 108

4.9 2D array correlation versus inter-element spacing. Reference plot: Directional, LOS, TM, f_c=60 GHz, d=50 m; (b) Isotropic antennas; (c) NLOS scenario; (d) TE polarization; (e) frequency increased to 300 GHz; (f) Range decreased to 10 m. 109

List of Tables

2.1 Summary of foliage loss models 36

3.1 Summary of effects of radio link and terrain parameters on channel properties 74

4.1 Coherence length (mm) versus antennas directivity and range . . . 111

Acknowledgments

First and foremost, I would like to thank my parents for their boundless love and support. They have always been the source of my happiness and motivation. They empowered me to handle many tense situations I faced during my doctoral studies.

I would like to thank my adviser, Dr. Seyed Zekavat, for guiding me with his seemingly infinite wisdom and for his thoughtful understanding in support of my research work. I had the good fortune of holding many insightful discussions with our research collaborator, Dr. Kamal Sarabandi, which helped me improve the quality of my work. I am grateful to other members of my dissertation committee, Dr. Michael Roggemann, Dr. Timothy Schulz, and Dr. Ossama Abdelkhalik for devoting their time and energy into this project.

During the course of my doctoral studies, I have learned from many faculty members at Michigan Tech. I would like to express my gratitude to Dr. Jeffrey Burl, Dr. Ashok Ambardar, Dr. Sean Kirkpatrick, Dr. Debra Charlesworth, Dr. Kirsti Arko, and Dr. Renfang Jiang.

I appreciate the support of staff members at Michigan Tech during my stay in Houghton. Especially, I would like to thank Ms. Lisa Rouleau, Ms. Michele Kamppinen, Ms. Joan Becker, Ms. Gina Dunstan, Ms. Mary Stevens, Ms. Julie Way, Dr.

Thy Yang, Ms. Nancy Byers-Sprague, and Ms. Carol Wingerson.

Finally, I would like to thank the National Science Foundation for their financial support that made this research work possible.

Abstract

Promising applications of wireless sensor networks (WSNs) and mobile ad hoc networks (MANETs) have stimulated growing interest to model and optimize their performance in various environments. In most of these applications, nodes operate at the ground level; however, near-ground channel models are scarce. In this research, a new computationally tractable path loss model is proposed for WSNs working above a dielectric rough terrain. Principles of the Fresnel zones are exploited to split the proposed path loss model into three segments. The distances that define the edges of each segment are derived theoretically. The effective reflection coefficients used in the proposed model include the effect of higher order surface waves and are applicable to grazing propagation when the surface roughness is less than a wavelength. Path loss predictions offered by the proposed model are consistent with the measurement results in rural and urban areas reported by independent researchers. Moreover, it is verified that by adding an empirically modeled foliage loss to the proposed model, it is possible to accurately evaluate the near-ground propagation in a foliage environment. Next, the proposed model is used to examine the influence of communication and link parameters on coverage range and network connectivity.

In view of exponential growth in data traffic demand, the wireless communications industry has aimed to increase the capacity of existing networks by 1000 times over

the next 20 years. A combination of extreme cell densification, more bandwidth, and higher spectral efficiency is needed to support the data traffic requirements for 5G cellular communications. In this research, the improvements achieved by using three major 5G enabling technologies (i.e., small cells, millimeter-wave spectrum, and massive MIMO) in rural and urban environments are investigated. This work develops SPM and KA-based ray models to investigate the impact of geometrical parameters such as the TRx range and height, soil physical and electrical properties such as roughness, textural composition, and moisture content. In addition, the impact of antenna parameters such as polarization and radiation pattern on terrain-based MU-MIMO channel characteristic parameters such as received power, power delay and angular profiles, RMS delay and angular spread, coherence bandwidth, and coherence distance are examined.

Moreover, Integrating Kirchhoff approximation (KA) and a ray-tracing (RT) algorithm, a new directional 3D channel model is developed for urban millimeter-wave (mmW) small cells. Path-loss, spatial correlation, coverage distance, and coherence length for line-of-sight (LOS), obstructed LOS (OLOS), and non-LOS (NLOS) scenarios are studied in urban areas. Exploiting physical optics (PO) and geometric optics (GO) solutions, closed form expressions for spatial correlation are derived. Coherence length is calculated for horizontal and vertical linear arrays as well as planar 2D arrays. It is deduced that LOS availability, frequency, and surface roughness scale highly impact spatial diversity.

Chapter 1

Introduction

1.1 Motivation

Multiple-Input Multiple-Output (MIMO) communication systems exploit antenna arrays at both the transmitter and receiver to offer parallel sub-channels to enhance the system capacity and quality of service (QoS) without requiring additional bandwidth or carrier power (see Figure 1.1) [1]-[3]. Nevertheless, realistic MIMO channels suffer from significant degradation of diversity gain and MIMO capacity due to the spatial correlation between the signals at different receiving antennas [4], [5]. The performance of adaptation techniques such as power allocation and antenna selection algorithms are also influenced by the spatial properties of the multipath channel.

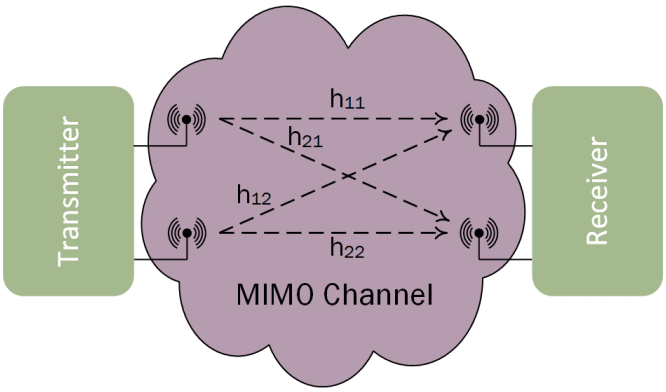

Figure 1.1: Schematic representation of a MIMO channel.

Spatial correlation is a measure of the similarity of signals at different antennas and it is a function of the spacing between antenna elements, radiation patterns, mutual coupling, array geometry, angular energy distribution of incoming waves, and the frequency of operation [6]-[9]. Lower correlation coefficients are highly desired to improve the performance of multiple antenna systems. In order to achieve a large diversity order, both base station (BS) and mobile station (MS) antenna elements should be separated sufficiently. There are practical limitations for accommodating more antenna elements in small portable devices, while multiple antennas can be readily implemented at the BS. For mobile terminals, ignoring the mutual coupling, antenna spacing of about $\lambda/2$ is suggested, as they are usually surrounded by scatterers providing a rich multipath environment. For elevated base stations, however, an inter-element separation of more than 10λ may be required to maintain a similar correlation coefficient [10]-[12].

In a scattering environment, several waves arrive at the elements of an antenna array

through different angles with different phases which reduces the correlation of signals received at antenna elements. In general, in order to have highly decorrelated signals at two antenna elements, we need to maintain a large inter-element spacing compared to the channel coherence distance. In addition, higher spacing reduces the mutual coupling [1], [13]. The correlation across antenna elements can be analytically calculated assuming a certain angle of arrival (AoA) distribution for the incoming waves at the elements of the multiple antenna system. Derivation of these statistical models is fairly simple, but to gain a physical insight into the propagation characteristics of a realistic environment, it is imperative to develop a geometry-based spatial MIMO channel model [14]-[17].

Surface roughness generates incoherent scattering, a.k.a. diffuse scattering, which results in correlation across spatially distributed antenna elements in a MIMO system. In-depth investigation into diffuse scattering effects on communication systems operating over a rough terrain is crucial to characterize a wireless channel [18]. Electromagnetic scattering models are divided into three categories that are empirical, numerical and analytical. Empirical solutions are based on measurement results and, hence, are site-specific and inflexible and do not provide an understanding of the various scattering mechanisms. In addition, development of a measurement campaign can be very costly. Numerical solvers can be categorized as frequency domain, such as method of moments (MoM), and time domain, e.g., finite difference time domain (FDTD) method. These techniques do not rely on simplifying assumptions and can

provide reliable results for any random roughness distribution and scale. However, the insurmountable computational burden of realistic scattering problems limits their usage to relatively small computational domains. Analytical solutions offer fast approximate results using certain simplifying assumptions. These powerful methods can provide physical insight into the scattering mechanisms with much lower computational cost and can be readily integrated with ray tracing algorithms to solve large three dimensional scattering problems [19]-[22].

Ray-tracing routines are used extensively in wave propagation modeling in outdoor and indoor environments. Surface roughness results in the scattering of the energy into the coherent and incoherent components. The coherent component is the mean value of the scattered energy while the incoherent component is the fluctuation around this mean value [23], [24]. To include the effects of the diffuse scattering component, a suitable scattering model should be implemented into the ray tracing routine. Kirchhoff approximation (KA) and SPM are the oldest and most common analytical treatments in scattering from random rough surfaces that address different scattering regimes. KA does not consider the curvature effects; hence, it is only applicable to smoothly undulating surfaces and it is only valid for surfaces with a large correlation length [25]. SPM is a low frequency approximation to the electromagnetic scattering from rough surfaces. SPM performs well for small roughness and slopes [25]-[29].

Because of the presence of scatterers in the environment, multipath propagation is

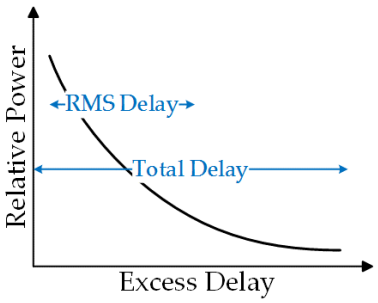

Figure 1.2: Delay spread in a multipath channel.

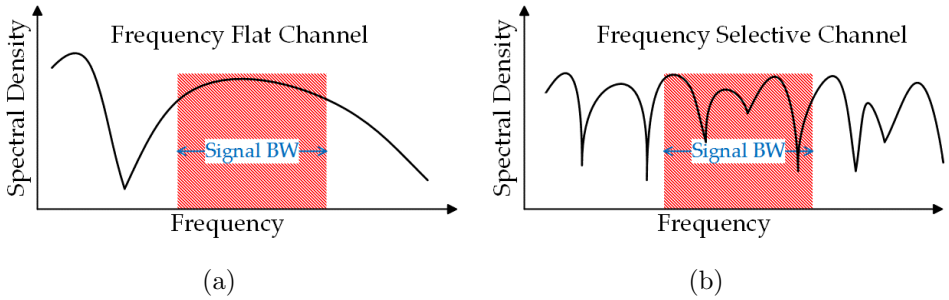

Figure 1.3: Frequency flat versus frequency selective channels.

inherent in realistic radio channels. Multipath not only decorrelates the signals at various receivers, but also induces delay spread which results in frequency-selective fading (see Figure 1.2 and Figure 1.3). Delay spread determines the maximum distortion-free data rates that can be transmitted via a wireless channel. Another critical parameter that is inversely proportional to delay spread is called the coherence bandwidth which quantifies the frequency variations of the channel [1]. Therefore, additional parameters such as delay spread and coherence bandwidth are required to describe the wireless channel.

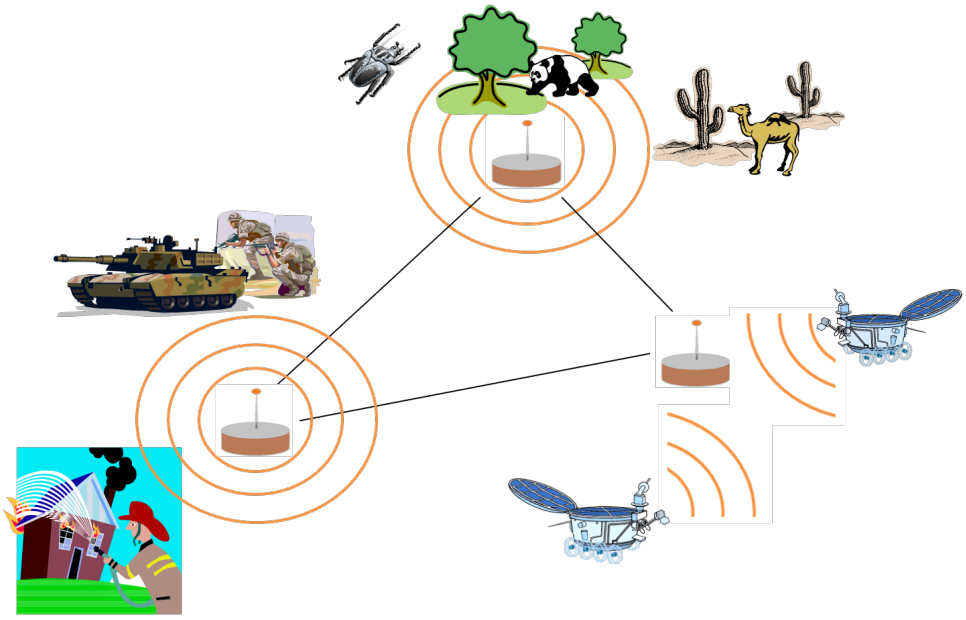

Figure 1.4: Near-ground sensor networks have many applications such as environmental monitoring, planetary explorations, disaster relief operations, and battlefield surveillance.

1.2 Channel modeling for near-ground wireless sensor networks

Wireless sensor networks (WSNs) have found a wide variety of applications in environmental, security, and infrastructure monitoring as well as location-based services (see Figure 1.4) [30]. In most of these emerging applications, sensor nodes work at or slightly above the ground level. However, there is a lack of accurate and computationally efficient radio models tailored for near-ground communications. In most available channel models antennas are assumed to be far above the ground [31]. Near-ground models proposed in the literature are few and they are mainly based on measurement

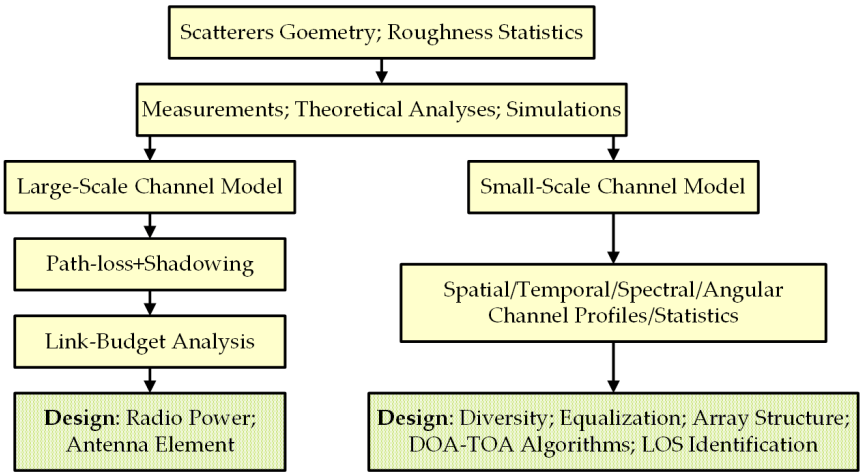

Figure 1.5: Impact of wireless channel modeling on wireless radio design.

campaigns that offer limited simulation scalability and are only accurate for certain environments [32-34].

As shown in Figure 1.5, channel parameters are vital for the design of wireless systems in different near ground WSN and localization applications. In sensor network applications, the height of the antennas above ground is usually low and it may approach zero. We call these situations, positive height or H^+. In some scenarios, ground laying antennas might be used where the antenna height is zero and it is represented by H^0. In some conditions, a wireless device and accordingly its antenna might be (slightly) buried under the ground, water, ice or snow. Thus, the antenna height might be slightly negative which we refer to as H^-.

In this research, a new computationally tractable path loss model is proposed for WSNs working above a dielectric rough terrain. Principles of the Fresnel zones are exploited to split the proposed path loss model into three segments. The distances

that define the edges of each segment are derived theoretically. The effective reflection coefficients used in the proposed model include the effect of higher order surface waves and are applicable to grazing propagation when the surface roughness is less than a wavelength. Path loss predictions offered by the proposed model are consistent with the measurement results in rural and urban areas reported by independent researchers. Moreover, it is verified that by adding an empirically modeled foliage loss to the proposed model, it is possible to accurately evaluate the near-ground propagation in a foliage environment. Next, the proposed model is used to examine the influence of communication and link parameters on coverage range and network connectivity.

1.3 Channel modeling for fifth generation (5G) cellular networks

Exponentially growing demand for higher wireless data throughput motivates exploring new technologies and investigating higher frequency spectrum [35]. Modulation techniques and channel coding are exploited to enhance spectral efficiency up to the Shannon limit. However, by exploiting higher carrier frequencies, higher data rates and service quality can be achieved [36]. Moreover, reducing access point coverage areas shortens the average distance between the base station and the device and improves the spatial frequency reuse. Hence, deployment of wide scale small cell access

points is another prevailing trend to improve the area spectral efficiency as well as energy efficiency [37]. Millimeter wave (mmW) frequencies between 30 GHz and 300 GHz have been proposed for outdoor small cells [38]. These frequencies provide much greater spectrum allocations and enable the placement of a large number of antenna elements in small form factors [37].

Massive MIMO, aka Multiuser MIMO (MU-MIMO), is a promising technology that uses a large excess of base station (BS) antennas to serve several user terminals in parallel in the same time-frequency resource. When MIMO channel matrix entries are sufficiently independent, multiple spatial dimensions become accessible for signaling, which offers capacity and multiplexing gain. However, to achieve such a decorrelation, large inter-element spacing and a rich scattering environment are required. MU-MIMO pulls together the distributed antennas at the user terminals to enjoy the advantages of MIMO in a much larger scale, even under difficult propagation conditions. Hence, MU-MIMO is an ideal candidate 5G technology for highway and rural macrocell deployments where there is limited infrastructure and unfavorable propagation conditions. MU-MIMO can drastically increase the capacity by aggressive spatial multiplexing. It can also increase the energy efficiency by several orders of magnitude by concentrating power into small regions in space via beamforming. Such high energy efficiency makes it possible to power the base stations using solar or wind energy in areas where electricity grids are unavailable. The maximum number of orthogonal pilot sequences is proportional to coherence time and bandwidth.

Fortunately, microwave MU-MIMO channels in open and rural environments exhibit high temporal stability and large coherence bandwidth, which increases the number of available orthogonal pilots and reduces the sounding process overhead.

This work develops SPM and KA-based ray models to investigate the impact of geometrical parameters such as the TRx range and height, soil physical and electrical properties such as roughness, textural composition, and moisture content. Moreover, the impact of antenna parameters such as polarization and radiation pattern on terrain-based MU-MIMO channel characteristic parameters such as received power, power delay and angular profiles, RMS delay and angular spread, coherence bandwidth, and coherence distance are examined. In this study, random terrain roughness is assumed Gaussian with an exponential correlation function. The proposed ray models enable us to study the impact of soil textural composition in terms of sand, silt, and clay fractions and soil water content by adjusting the terrain dielectric constant. Different types of soil are considered and it is realized that the soil particle fractions and, more importantly, its volumetric moisture content can make a notable difference on the electrical properties of the terrain and, hence, the scattered power.

Moreover, Integrating Kirchhoff approximation (KA) and a ray-tracing (RT) algorithm, a new directional 3D channel model is developed for urban millimeter-wave (mmW) small cells. Path-loss, spatial correlation, coverage distance, and coherence

length for line-of-sight (LOS), obstructed LOS (OLOS), and non-LOS (NLOS) scenarios are studied in urban areas. Exploiting physical optics (PO) and geometric optics (GO) solutions, closed form expressions for spatial correlation are derived. Coherence length is calculated for horizontal and vertical linear arrays as well as planar 2D arrays. It is deduced that LOS availability, frequency, and surface roughness scale highly impact spatial diversity. In addition, using antenna arrays of moderate gain at both sides of the link, even under NLOS conditions, a typical urban cell size of 200m is achievable.

1.4 Overview of dissertation

A versatile near-ground field prediction model is proposed in chapter 2 to facilitate accurate WSN simulations. Path loss is split into three segments using the principles of the Fresnel zones. The distances that define the edges of each segment are derived theoretically. The model is validated against several experimental data sets obtained in different environments. It is observed that the proposed model has higher accuracy compared to existing near-ground analytical propagation models. This improvement is due to careful assessment of the impact of first Fresnel zone obstruction, terrain irregularities and dielectric properties on the direct, specularly reflected and higher order waves. Effects of antenna height, frequency of operation, polarization and

terrain electrical and geometrical properties on the range and connectivity of low-altitude WSNs are studied through Monte Carlo simulations.

In chapter 3, small perturbation method (SPM) and Kirchhoff approximation (KA) are incorporated into ray-tracing (RT) routines to model multiuser multi-input multi-output (MU-MIMO) channels formed on a rough dielectric terrain. The effect of surface roughness and correlation length, solid soil fractions, moisture content, link range, antenna height, polarization, radiation pattern, and carrier frequency are examined on received power, power delay and angular profiles, root mean square (RMS) delay and angular spread, coherence bandwidth, and coherence distance. Quantitative and qualitative analyses reveal that antenna directionality and terrain undulation and textural composition have significant impacts on the received signal power and channel multipath parameters and, hence, the performance of MU-MIMO terrain-based communication systems.

In chapter 4, integrating Kirchhoff approximation (KA) and a ray-tracing (RT) algorithm, a new directional 3D channel model for urban millimeter-wave (mmW) small cells is developed. Path-loss, spatial correlation, coverage distance, and coherence length for line-of-sight (LOS), obstructed LOS (OLOS), and non-LOS (NLOS) scenarios are studied in urban areas. Exploiting physical optics (PO) and geometric optics (GO) solutions, closed form expressions for spatial correlation are derived. It is deduced that LOS availability, frequency, and surface roughness scale highly impact

spatial diversity. In addition, using antenna arrays of moderate gain at both sides of the link, even under NLOS conditions, a typical urban cell size of 200m is achievable.

Chapter 5 concludes the dissertation and offers possible future work.

Chapter 2

Near-Ground Channel Modeling for Wireless Sensor Networks

2.1 Introduction

Wireless sensor networks (WSNs) have found a wide variety of applications in environmental, security, and infrastructure monitoring as well as location-based services. In most of these emerging applications, sensor nodes work at or slightly above the ground level [39]. However, there is a lack of accurate and computationally efficient radio models tailored for near-ground communications. In most available channel models antennas are assumed to be far above the ground [40], [41]. There are few

near-ground models proposed in the literature that are mainly based on measurement campaigns. These models offer limited simulation scalability and are only accurate for certain environments [31], [34], [41]-[48]. In this study, a versatile theoretical model is developed to predict the feasible transceiver (TRx) range and node connectivity for WSNs deployed for diverse applications. The applicability of the proposed model is verified by comparing the results with the near-ground measurements carried out by independent researchers in rural, forested and urban settings.

Promising applications of WSNs and mobile ad hoc networks (MANETs) have stimulated growing interest to model and optimize their performance in various environments [31], [49]. Based on the measurement results reported by several researchers, it is known that lowering the antennas altitude significantly decreases the signal strength, hence, reducing the system range. This effect is addressed in [31] by proposing a two-slope log-normal path loss model for a WSN at 868 MHz in an open area. In [42], the impact of foliage on near-ground radiowave propagation is studied for battlefield sensor networks operating at 300 MHz and 1900 MHz. Measurement results for ground-based UHF band communicators in urban terrain are reported in [43] for both line-of-sight (LOS) and non-line-of-sight (NLOS) links. Numerical solvers are prescribed in [44] and [45] to characterize near-ground long range propagation but their computational complexity limits the number of nodes in the simulated network. In [46], a simple mathematical path loss model for near-ground links is introduced. Nonetheless, a flat perfectly conducting ground is assumed in the derivation of the

model which overlooks the significant impact of terrain roughness and electrical properties on the channel transfer characteristics. In addition, the break point distance after which, according to the two-ray propagation model, the path loss increases at the rate of 40dB per decade is set too far which results in underestimation of the path loss at larger distances.

According to the plane-earth model, at small range, strong oscillations take place around the direct ray level. However, the median power falloff rate obtained through regression fits is roughly the same as in free space and the total loss can be approximated by the free space loss [50]. The distance where the last maximum in the received wave pattern occurs is called the break distance, d_B, that is a function of antenna heights and operating frequency. At this distance, the first Fresnel zone touches the ground and the direct and ground-reflected waves, collectively called the space waves, only combine destructively beyond this range. Owing to destructive interference between the space waves, the power falloff rate increases from 20 dB/decade before d_B to 40 dB/decade after it. At almost three times the break distance, we will reach the critical distance, d_C. This is the distance where almost 57% of the first Fresnel zone is still clear of obstruction. If we move farther than the critical distance, ground turns into a significant obstruction for the transmitted energy and diffraction loss should also be included in the total loss. As explained in [51], using the two-ray analysis, we can make out another distinct region. At distances smaller than the transmitter height ($d < h_t$), space waves only combine constructively and

the received signal strength increases slowly. However, this region does not have any practical importance for near-ground WSNs and will be neglected in this work.

Plane-earth propagation model offers a simple but useful path loss model which properly predicts the rise of the falloff rate at the break distance. However, in order to arrive at a more accurate model suitable for sensor network design, we shall also consider the geometrical and electrical properties of terrain. For propagation above an irregular terrain, the physical statistical properties of the ground surface have a considerable impact on the statistics of the received signal by decreasing the ground reflectivity and generating local surface waves. For rough surfaces, an equivalent reflection coefficient can be derived by multiplying the plane surface reflection coefficient by a scattering loss factor to account for the reduction in the reflected signal amplitude. Two commonly used approximations for the scattering loss factor are derived by Ament and Boithias [52], [53].

In WSNs, due to low heights of the sensor nodes, propagation often approaches the grazing condition. In this scenario, according to the Rayleigh criterion, the surface appears electrically smooth and the space waves cancel each other, leaving only the higher order surface waves. It is shown in [54] that as long as the TRx altitude is low in terms of the wavelength, these surface waves are dominant regardless of frequency of operation. Nevertheless, the traditional loss factors found by Ament and Boithias disregard the effects of terrain self-shadowing and surface waves which render them

inadequate for near-ground propagation.

In this chapter, a new computationally tractable path loss model is proposed for WSNs working above a dielectric rough terrain. Principles of the Fresnel zones are exploited to split the proposed path loss model into three segments. The distances that define the edges of each segment are derived theoretically. In the first region, the line-of-sight ray dominates the signal transmission while in the second region both the direct and ground-reflected signals impact the received energy. In the third region, diffraction loss caused by insufficient path clearance is also added to the reference loss. The effective reflection coefficients used in the proposed model include the effect of higher order surface waves and are founded on the perturbation approach applied to a volumetric integral equation and are applicable to grazing propagation when the surface roughness is less than a wavelength [55], [56]. Path loss predictions offered by the proposed model are consistent with the measurement results in rural and urban areas reported by independent researchers. Moreover, it is verified that by adding an empirically modeled foliage loss to the proposed model, it is possible to accurately evaluate the near-ground propagation in a foliage environment. Finally, the proposed model is used to examine the influence of communication and link parameters on coverage range and network connectivity.

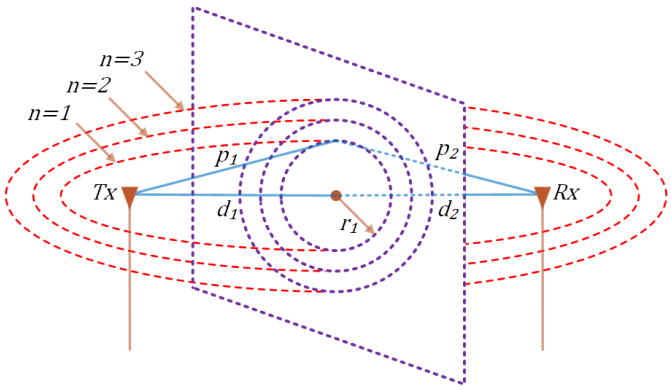

Figure 2.1: Family of Fresnel zones. An imaginary plane perpendicular to the LOS cuts the successive Fresnel ellipsoids in concentric circles.

2.2 Derivation of the break points

The locus of all points having a constant value of excess path length, Δd, as compared to the direct path, forms an ellipsoid of revolution with the two terminals at the foci and the LOS path as the axis of revolution. A family of such ellipsoids in which Δd varies in integer multiples of half-wavelengths, $n\lambda 2$ with n an integer and λ the wavelength, is called the Fresnel zones [50]. As shown in Figure 2.1, the intersection of these Fresnel ellipsoids with an imaginary plane perpendicular to the LOS path constructs a family of concentric circles with radii

$$r_n = \sqrt{\frac{n\lambda d_1 d_2}{d_1 + d_2}} \tag{2.1}$$

where d_1 and d_2 are the distances of the plane from the transmitter and the receiver, respectively [50]. Equation (2.1) is valid if $d_1, d_2 \gg r_n$. The radii of the circles depend

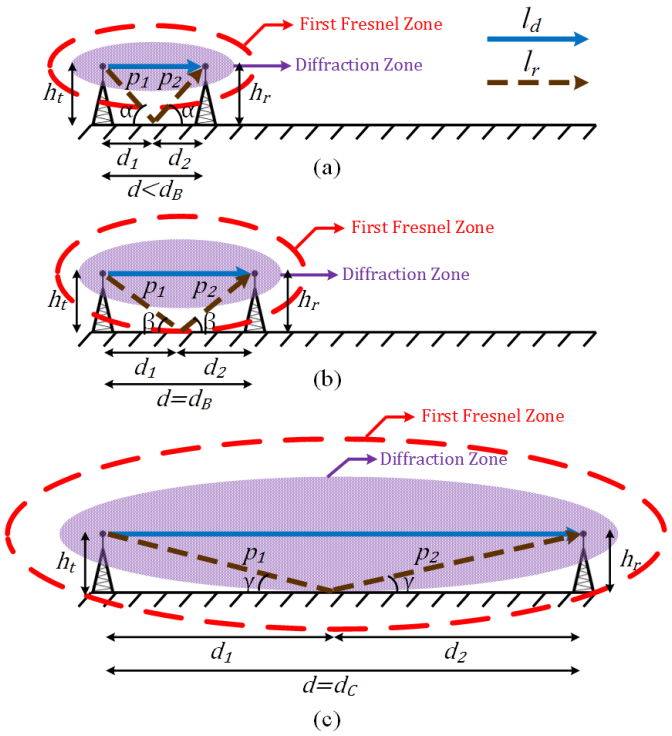

Figure 2.2: Schematic representation of the first Fresnel zone and the diffraction zone in a radio link as the distance between two terminals increases. (a) First Fresnel zone is clear of obstructions; (b) First Fresnel zone touches the ground surface; (c) Diffraction zone is tangent to the ground surface.

on the location of the plane and reach their maximum of $r_{n,max} = \sqrt{n\lambda d}/2$ when the plane is midway between the terminals where $d = d_1 + d_2$.

Most of the radio energy is concentrated in the first Fresnel zone; hence, to prevent the blockage of energy, we site the antennas such that the first Fresnel zone is clear of obstacles. As sketched in Figure 2.2, when one terminal moves away from the other, the radius of the first Fresnel zone increases until it touches the earth surface at the break distance, d_B. d_B divides the LOS propagation path into two distinct near and far regions. In the near region, mean signal attenuation is equivalent to free space

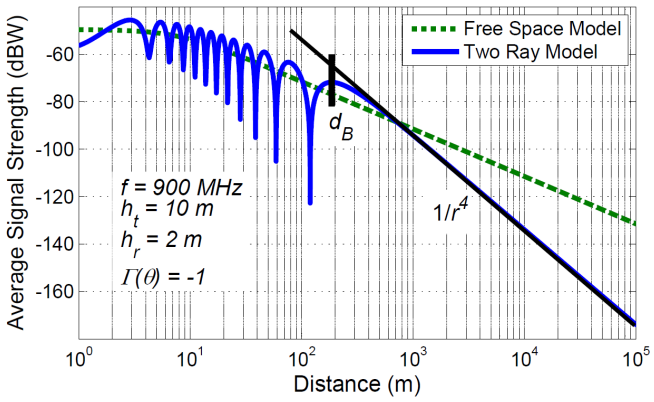

Figure 2.3: Path loss versus terminal separation for free space model and two-ray model. Depiction of the break distance and dual-slope piece-wise linear regression fit in a microcellular propagation scenario assuming a flat perfectly conducting ground plane.

wavefront spreading loss, whereas beyond d_B, obstruction of the first Fresnel zone also contributes to attenuation loss which results in a steeper falloff rate of the signal strength.

Figure 2.3 illustrates the concept of the near/far regions using the two ray model. In the near region, regression fits about the oscillatory pattern of the received signal result in a path loss exponent of two which corresponds to free space loss. However, in the far region, destructive interference of the direct and reflected signals leads to a path loss exponent of four. Break distance indicates the position where the gradual transition from square law to fourth law begins. This phenomenon serves as the basis for the well-known dual-slope piecewise linear path loss model for microcellular LOS topographies.

Specularly reflected ray travels the shortest path among all the rays scattered by

the ground for any given transmitter and receiver heights and separation. Therefore, when the range increases, any ellipsoid with the transmitter and receiver as the foci first touches the ground on the specular point. Referring to Figure 2.2(b), at the break distance, the first Fresnel zone is tangent to the ground and the excess path length equals

$$\Delta d = l_r - l_d = \frac{\lambda}{2} \tag{2.2a}$$

$$l_d = \sqrt{d_B^2 + (h_t - h_r)^2} \tag{2.2b}$$

$$l_r = \sqrt{d_B^2 + (h_t + h_r)^2} \tag{2.2c}$$

in which l_d and l_r are the direct and reflected path lengths, respectively, and h_t and h_r are the transmitter and receiver heights, respectively. If we multiply both sides of (2.2a) by $(l_d + l_r)$ and substitute (2.2b) and (2.2c) into the resulting equation, after simple algebraic manipulations we will find

$$l_d + l_r = \frac{8 h_t h_r}{\lambda}. \tag{2.3}$$

Adding (2.2a) and (2.3), we can find the break distance as

$$d_B = \sqrt{\left(\frac{4 h_t h_r}{\lambda} + \frac{\lambda}{4}\right)^2 - (h_t + h_r)^2}. \tag{2.4}$$

Alternatively, subtracting (2.2a) from (2.3), we can write

$$d_B = \sqrt{\left(\frac{4h_t h_r}{\lambda} - \frac{\lambda}{4}\right)^2 - (h_t - h_r)^2}. \tag{2.5}$$

We can rewrite (2.5) as

$$d_B = \frac{4h_t h_r}{\lambda}\sqrt{1 - \frac{\lambda^2\left(h_t^2 + h_r^2\right)}{(4)^2 h_t^2 h_r^2} + \left(\frac{\lambda^2}{(4)^2 h_t h_r}\right)^2} \approx \frac{4h_t h_r}{\lambda}. \tag{2.6}$$

The approximate value in (2.6) is valid if $h_t, h_r \gg \lambda$ and is famously known as the break distance in the microcellular propagation scenario. However, in near-ground sensor network channel modeling, this approximation is no longer accurate as the condition does not hold. Hence, in this work, the exact formula in (2.5) will be used for the break distance. Using the notations in Figure 2.1 and Figure 2.2, we can write

$$p_1 = \sqrt{d_1^2 + h^2} \approx d_1 + \frac{h^2}{2d_1}, \quad h \ll d_1 \tag{2.7a}$$

$$p_2 = \sqrt{d_2^2 + h^2} \approx d2 + \frac{h^2}{2d_2}, \quad h \ll d_2 \tag{2.7b}$$

in which d_1 and d_2 are the horizontal distances between the transmitter-obstacle and obstacle-receiver, respectively. h is the obstruction height which is always a negative

value in LOS topographies and can be expressed as

$$h = -\left[h_r + (h_t - h_r)\frac{d_2}{d}\right], \quad 0 \leq d_2 \leq d \tag{2.8}$$

where $d = d_1 + d_2$ is the horizontal distance between the transmitter and receiver. As mentioned earlier, the point where the ellipsoid touches the surface of the earth is the specular reflection point which can be used to find d_2 and d in a more convenient form given by

$$d_2 = \left(\frac{h_r}{h_t + h_r}\right) d \tag{2.9a}$$

$$h = \frac{-2h_t h_r}{h_t + h_r}. \tag{2.9b}$$

Now, we can write

$$\Delta d = l_r - l_d = (p_1 + p_2) - (d_1 + d_2) \approx \frac{h^2}{2}\left(\frac{d}{d_1 d_2}\right). \tag{2.10}$$

We can express the phase difference between the LOS and the reflected paths as

$$\Delta\varphi = \frac{2\pi\Delta d}{\lambda} = \frac{\pi}{2}\upsilon^2. \tag{2.11}$$

ν is the dimensionless Fresnel-Kirchhoff diffraction parameter that corresponds to [51]

$$\upsilon = h\sqrt{\frac{2d}{\lambda d_1 d_2}} = \frac{h}{r_n}\sqrt{2n}. \tag{2.12}$$

h/r_n is called the Fresnel zone clearance. According to the Fresnel knife-edge diffraction model, when ν is approximately -0.8 or less, there is sufficient LOS path clearance and the diffraction loss is minimal. Substituting ν=-0.8 in (2.12), it is found that h=-0.566 which implies that as long as almost 57% of the first Fresnel zone is kept clear of obstacles, diffraction loss can be neglected. To find the critical distance, d_C, we first substitute ν=-0.8 in (2.11) and find Δd=0.16 λ is the path lengths difference at the critical distance. Therefore, using the same approach as was employed to derive the break distance,

$$l_r - l_d = \Delta d = 0.16\lambda \tag{2.13a}$$

$$l_r + l_d = \frac{25 h_t h_r}{\lambda}. \tag{2.13b}$$

Adding (2.13a) and (2.13b), we can find the critical distance as

$$d_C = \sqrt{\left(\frac{12.5 h_t h_r}{\lambda} + \frac{\lambda}{12.5}\right)^2 - (h_t + h_r)^2}. \tag{2.14}$$

Alternatively, subtracting (2.13a) from (2.13b), we can write

$$d_C = \sqrt{\left(\frac{12.5 h_t h_r}{\lambda} - \frac{\lambda}{12.5}\right)^2 - (h_t - h_r)^2}. \tag{2.15}$$

We can rewrite (2.15) as

$$d_C = \frac{12.5 h_t h_r}{\lambda} \sqrt{1 - \frac{\lambda^2 \left(h_t^2 + h_r^2\right)}{(12.5)^2 h_t^2 h_r^2} + \left(\frac{\lambda^2}{(12.5)^2 h_t h_r}\right)^2} \approx \frac{12.5 h_t h_r}{\lambda}. \tag{2.16}$$

However, the approximate value in (2.16) is valid as long as $h_t, h_r \gg \lambda$ that does not apply to near-ground WSN scenario. Therefore, in this study, the exact formula in (2.15) will be used for the critical distance. As witnessed in [57], dual-slope piecewise linear path loss model based on Fresnel zone clearance can predict the LOS microcellular propagation loss as accurately as a minimum mean square error (MMSE) regression fit on the measured data in open, urban and suburban areas. This work will inspect the accuracy and adequacy of such models for near-ground sensor networks.

2.3 Near-ground path loss model

2.3.1 Short-range communication

As shown in Figure 2.2(a), when $d < d_B$, the first Fresnel zone is clear of obstacles. In this region, reflected field from the ground interferes with the direct signal causing the signal level to oscillate widely. However, the attenuation of the median received signal with distance is almost the same as that of free space. Hence, attenuation is entirely due to the spreading of wavefront which corresponds to the free-space path

loss,

$$L_{fs} = (2kd)^2 \tag{2.17}$$

in which $k = \omega\sqrt{\mu\varepsilon_0} = 2\pi/\lambda$ is the free space wavenumber, ω is the angular frequency, ε_0 is the free space permittivity, μ is the permeability, and λ is the wavelength in free space.

2.3.2 Medium-range communication

As shown in Figure 2.2(b), when $d > d_B$, part of the energy in the first Fresnel zone is intercepted by the ground. Therefore, attenuation results from both spherical wavefront spreading and obstruction of the first Fresnel zone which leads to a more pronounced decay rate. Plane-earth propagation model offers a good prediction of signal attenuation in this region; however, assuming a flat perfectly conducting ground leads to an overestimation of the destructive interference between the direct and the geometrical-optics (GO) reflection fields which gives an imprecisely high power falloff rate. As found in [58], disregarding the electrical properties of the terrain can lead to grave errors as large as 10 dB which is unacceptable in designing energy-constrained wireless sensor networks. Moreover, according to [56], including the physical statistics of the terrain roughness in the model may attenuate the ground wave by up to 6 dB for realistic ground surfaces.

To investigate the impact of roughness statistics on the signal transmission, the Fresnel reflection coefficient of a flat surface is modified using a correction factor to create an effective reflection coefficient. Traditional correction factors such as those proposed by Ament and Boithias [56] are simple to implement and are sufficiently accurate for remote sensing and microcellular applications. However, for sensor network design, they have fundamental shortcomings which stem from the near-grazing propagation condition. At low grazing angles, in conformity with the Rayleigh criterion, since the incident waves are almost parallel to the surface of the plane, the direct and ground reflected components cancel each other even for larger roughness heights. Therefore, the surface waves which are smaller in magnitude and are highly localized to the ground boundary become the dominant propagation mechanism. However, surface waves are not considered in the conventional correction factors. They also overlook the impacts of polarization of the incident wave and roughness correlation length.

The effective reflection coefficients used in our model address the impacts of surface waves, incident polarization, and surface correlation distance and are founded on the perturbation theory applied to a volumetric integral equation originally prescribed in [55], [56]. They are valid for low grazing propagation as far as the surface roughness height is less than a wavelength. The two-ray model over rough dielectric terrain is given by

$$L_{tr} = L_{fs}.L_{ex} \tag{2.18}$$

in which L_{fs} is the free-space attenuation and L_{ex} is the excess loss factor due to obstruction of the Fresnel zone which corresponds to

$$L_{ex} = \left| 1 + \frac{l_d}{l_r} R_\alpha^{eff} e^{(-j\Delta\varphi)} \right|^2 \tag{2.19}$$

where l_d, l_r, and $\Delta\phi$ can be calculated using (2.2b), (2.2c), and (2.11), respectively. R_α^{eff} is the effective reflection coefficient where $\alpha = v, h$ denotes the vertical or horizontal incident polarization, respectively. Then,

$$\begin{aligned} R_v^{eff} = R_v + \frac{\sigma^2}{2}\left(k_1^2 - k^2\right)\left(R_v^2 - 1\right) \\ -\sigma^2 \frac{k_{ix}^2\left(k_1^2 - k^2\right)}{k^2\left(\varepsilon_1 k_{iz} + k_{1zi}\right)}\left[\left(R_v - 1\right)k_{iz} - \left(R_v + 1\right)k_{1zi}\right] \\ -\sigma^2 \frac{\left(k_1^2 - k^2\right)^2}{2\pi k^4\left(\varepsilon_1 k_{iz} + k_{1zi}\right)}\left[\left(R_v - 1\right)k_{iz}A_x\left(k_x\right) + \left(R_v + 1\right)k_{ix}A_z\left(k_x\right)\right] \end{aligned} \tag{2.20a}$$

$$R_h^{eff} = R_h - \frac{\sigma^2}{2}\left(k_1^2 - k^2\right)\left(R_h^2 - 1\right) - \sigma^2 \frac{\left(k_1^2 - k^2\right)^2}{2\pi\left(k_{iz} + k_{1zi}\right)}\left(R_h + 1\right)A_y\left(k_x\right) \tag{2.20b}$$

where

$$A_x\left(k_x\right) = \int_{-\infty}^{\infty} \frac{k'_{1z}\left(k_{1zi}k'_z + k_{ix}k'_x\right)}{\left(\varepsilon_1 k'_z + k'_{1z}\right)} W\left(k'_x - k_{ix}\right) dk'_x \tag{2.21a}$$

$$A_y\left(k_x\right) = \int_{-\infty}^{\infty} \frac{1}{k'_z + k'_{1z}} W\left(k'_x - k_{ix}\right) dk'_x \tag{2.21b}$$

$$A_z\left(k_x\right) = \int_{-\infty}^{\infty} \frac{k'_x\left(k_{1zi}k'_z + k_{ix}k'_x\right)}{\left(\varepsilon_1 k'_z k'_{1z}\right)} W\left(k'_x - k_{ix}\right) dk'_x. \tag{2.21c}$$

k is the wavenumber in the air and k_1 is the wavenumber in the dielectric. k_{iu}/k_u

stands for the wavenumber components in the incident (scattered) direction where $u = x, z$. We have $k_x = k \sin\theta$ and $k_z = k \cos\theta$ in which θ is the elevation angle. The rough surface is characterized by a random height function $z = f(x)$, in which $f(x)$ is a random function with zero mean, i.e., $\langle f(x) \rangle = 0$. Statistics of the roughness are included in the model using surface RMS height, σ, and roughness correlation length, L, which is incorporated in the Gaussian spectral density function $W(k_x) = \sqrt{\pi} L e^{\left(-k_x^2 L^2/4\right)}$. Electrical properties of the terrain are taken into account using the effective permittivity, ε_1, of the underlying dielectric layer. Integrals in (2.21) are fast converging and are evaluated numerically. Most of their contribution comes from a narrow angular range centered on the specular direction ($k = k_{ix}$), which expands by increasing the roughness height. R_v and R_h are the Fresnel reflection coefficients of a flat surface for vertical and horizontal polarizations, respectively,

$$R_v = \frac{k_1^2 k_{iz} - k^2 k_{1zi}}{k_1^2 k_{iz} + k^2 k_{1zi}} \tag{2.22a}$$

$$R_h = \frac{k_{iz} - k_{1zi}}{k_{iz} + k_{1zi}} \tag{2.22b}$$

At this point, it is worth noting that a 1D surface model is adopted to derive the effective reflection coefficients. A 1D rough surface refers to a surface with protuberance along one horizontal coordinate and constant profile along the other, whereas a 2D rough surface has variations along both horizontal coordinates. As verified throughout our simulations, assuming a 1D rough surface in the construction of a path loss model

leads to tremendous computational savings while being perfectly adequate for the following reasons: (1) Surfaces under study are assumed to be geometrically isotropic. Examples of anisotropic surfaces are some wind-driven and cultivated lands; (2) in a path loss model, we are only interested in scattering effects in the plane of incidence. Scattering outside the plane of incidence cannot be accurately predicted using a 1D model unless the roughness under consideration is truly 1D [59]. On the other hand, off the plane scattering becomes critical when dealing with 3D spatial channel characterization; and (3) it is well-known that cross-polarized fields are only created by 2D surfaces. However, the amplitude of the cross-polarized fields generated by realistic rough surfaces is generally several orders of magnitude smaller than that of the co-polarized fields. Hence, cross-polarized components do not serve an important role in the transmission of energy and can be ignored in the path loss model.

2.3.3 Long-range communication

In cellular communications, cell radii are much smaller than d_B to reduce the transmit power and increase the capacity. However, in WSNs, antenna heights are very low and a significant part of the first Fresnel zone is always occupied by the ground; therefore, in most applications, the link range by far exceeds d_C. For example, at the frequency of 915 MHZ if we consider the antenna heights are 7 cm then, according to (2.5) and (2.15), the break distance, d_B, is only 2.2 cm and the critical distance,

d_C, is roughly 16 cm. Hence, computing the diffraction loss, that can attenuate the transmitted signal by up to 6 dB, is integral to WSN channel characterization. Here, total path attenuation is the sum of the loss due to an ideal knife-edge diffraction and an additional reference loss that takes account of the diffractor (rough terrain) parameters such as permittivity and roughness statistics which are discussed in the previous subsection. The path loss associated with knife-edge diffraction is calculated by assuming an asymptotically thin diffracting object half-way between the transmitter and receiver, which corresponds to [50]

$$L_{ke} = \left(0.5 + \frac{0.877\left(h_t + h_r\right)}{\sqrt{\lambda d}}\right)^2 \tag{2.23}$$

Finally, the proposed near-ground WSN path loss model in decibel is summarized as

$$L_{NG}\left(dB\right) = \begin{cases} L_{fs} & \text{if } d \leq d_B \\ L_{fs} + L_{ex} & \text{if } d_B \leq d \leq d_C \\ L_{fs} + L_{ex} + L_{ke} & \text{if } d \geq d_C \end{cases} \tag{2.24}$$

where

$$L_{fs}\,(dB) = -27.56 + 20\log_{10}(f) + 20\log_{10}(d) \tag{2.25a}$$

$$L_{ex}(dB) = 20\log_{10}\left|1 + \frac{l_d}{l_r} R_{\alpha}^{eff} e^{(-j\Delta\varphi)}\right| \tag{2.25b}$$

$$L_{ke}(dB) = 20\log_{10}\left(0.5 + \frac{0.877\,(h_t + h_r)}{\sqrt{\lambda d}}\right) \tag{2.25c}$$

and d_B and d_C have been introduced in (2.4) and (2.14), respectively. Here, f is in MHz and d, h_t, h_r, and λ are all in meters.

2.3.4 Added features in urban settings

LOS urban propagation, for instance an in urban canyon, can be well predicted using the proposed model because the canyon only rises the spatial fading but the average trend do not change noticeably [43]. However, in NLOS scenario, an additional term in the model is required to account for the steeper falloff rate. Here, to include the excess NLOS loss, we exploit an empirical formula originally derived for ground-based communicators in an L-shaped urban path at UHF [43],

$$L_{NLOS}(dB) = 8 + 10 n_{NLOS} \log_{10} \frac{d}{d_L} \tag{2.26}$$

in which n_{NLOS} is the NLOS path loss factor given by

$$n_{NLOS} = \left[4.27 \times 10^{-5}\,(f - 225) - 8.22 \times 10^{-4}\,(W - 17) + 0.033\right] d_L + 2.7. \quad (2.27)$$

Here, f is the frequency in MHz, W is the width of the NLOS route in meters, and d_L is the length of the LOS route in meters prior to turning into the NLOS route. As we turn from the LOS street to the NLOS street, a discontinuity in the received power level occurs which is referred to as the corner loss in [43] and is set to 8 dB based on averaging the measurement results which is included in (2.26).

2.3.5 Foliage loss

WSNs deployed in wild environments often undergo an excess attenuation due to signal transmission through a depth of foliage. We shall add an empirically modeled foliage loss to our model in order to assess its prediction accuracy in forested environments. Foliage induced excess loss is generally represented in mathematical form $L_{fo}(dB) = uf^v d_{fo}^w$, where f is the frequency of operation typically in MHz or GHz and d_{fo} is the propagation distance through foliage in meters. u, v, and w are numerical values evaluated using least squared error fitting on the measured data. Table 2.1 summarizes some of the well-known foliage loss models in the literature [34], [60]-[63].

Table 2.1
Summary of foliage loss models

Model	Expression	Notes
Weissberger's Model [60]	$L_{fo}(dB) = \begin{cases} 0.45f^{0.284}{d_{fo}}^{1}, & 0 < d_{fo} \leq 14\ m \\ 1.33f^{0.284}{d_{fo}}^{0.588}, & 14\ m < d_{fo} \leq 1400\ m \end{cases}$	f in GHZ; d_{fo} in meters $0.230\ GHz \leq f \leq 95\ GHz$ for dense, dry, in leaf trees
COST 235 Model [61]	$L_{fo}(dB) = \begin{cases} 26.6f^{-0.2}{d_{fo}}^{0.5}, & out\ of\ leaf \\ 15.6f^{-0.009}{d_{fo}}^{0.26}, & in\ leaf \end{cases}$	f in MHZ; d_{fo} in meters $9.6\ GHz \leq f \leq 57.6\ GHz$ $d_{fo} \leq 200\ m$
ITU-R Model [62]	$L_{fo}(dB) = 0.2f^{0.3}{d_{fo}}^{0.6}$	f in MHZ; d_{fo} in meters $for\ UHF\ d_{fo} \leq 400\ m$
Fitted ITU-R Model [63]	$L_{fo}(dB) = \begin{cases} 0.37f^{0.18}{d_{fo}}^{0.59}, & out\ of\ leaf \\ 0.39f^{0.39}{d_{fo}}^{0.25}, & in\ leaf \end{cases}$	f in MHZ; d_{fo} in meters $for\ SHF$
Lateral ITU-R Model [34]	$L_{fo}(dB) = 0.48f^{0.43}{d_{fo}}^{0.13}$	f in MHZ; d_{fo} in meters $for\ VHF\ d_{fo} \leq 5\ km$ $for\ UHF\ d_{fo} \leq 1.2\ km$

2.4 Model validation and WSN connectivity analysis

In this section, prediction ability of the proposed model is verified by comparing it to the near-ground measurements in open, urban, and forested areas reported by independent researchers. Next, the influence of terrain electrical and geometrical properties on the range and connectivity of low-altitude WSNs are discussed.

2.4.1 Model validation and discussion

Here, the prediction results of our model are validated against available near-earth measurement campaigns. Many empirical models in the literature are provided without stating the dielectric and roughness properties of the terrain over which the measurements are performed. In these cases, we consider $\varepsilon = \varepsilon_r - j60\kappa\lambda$ where for average ground the dielectric constant is ε_r=15, conductivity is κ=0.005 mhos/m, σ=1.13 cm is the roughness RMS height, and surface correlation length is L=7.39 cm [50], [64]. Moreover, transceiver antenna gains are removed from the received power to find the path loss, whenever necessary.

Figure 2.4(a) compares the proposed model predictions with the LOS stationary measurements at distance of 75 m using monopole antennas working at 300 MHz [42]. Model predictions match the measurements closely. It is noted that path loss is largely dependent on the terminal heights. Therefore, any model that does not explicitly include the impact of antennas altitude is ineffective in WSN design. Figure 2.4(a) also inspects the path loss prediction accuracy of the proposed model in comparison with the near-ground analytic models reported in the literature. Since our model takes account of the impact of terrain irregularities and dielectric properties on the GO reflection and higher order fields, it achieves remarkably higher accuracy in predicting the path loss compared to previous analytic models which neglect one or several of

the aforementioned propagation features.

In Figure 2.4(b), measurements at 868 MHz are carried out in three different quasi-flat open environments, namely, a ground plain, a yard, and a grass park. $\lambda/4$ Monopole antennas are employed at height of 13 cm [31]. There is a vast disparity between the measurements especially at long range which are attributed to uneven terrain and presence of large scatterers in proximity of the measurement setup. Nevertheless, it is observed that the proposed model together with the model in [48] lie between and follow the slope of the measured curves along their entire range while the model in [46] deviates at longer distances.

WSN nodes deployed in urban and suburban settings are generally much closer to the ground (usually asphalt) than to the building facades which implies that the break distances formulated in this study apply to LOS urban topographies as well. Moreover, this model also works for NLOS scenario provided it is supplemented by the excess loss term in (2.26). Figure 2.5 shows the path loss along an L-shaped urban route measured using omnidirectional wideband discone antennas at 225 MHz along with the model predictions [43]. Antennas height is 2 m and the width of the NLOS route is 17 m. Each result is piecewise linear with three distinct segments that correspond to a LOS segment, a corner loss segment, and a NLOS segment. Since the measured LOS data are fitted into a single slope line, it appears that the measured and predicted results are diverging up to the break distance which does not have a

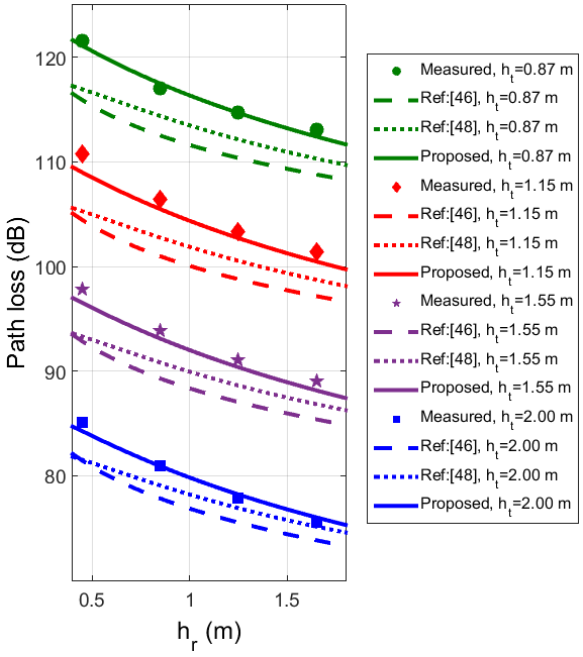

(a)

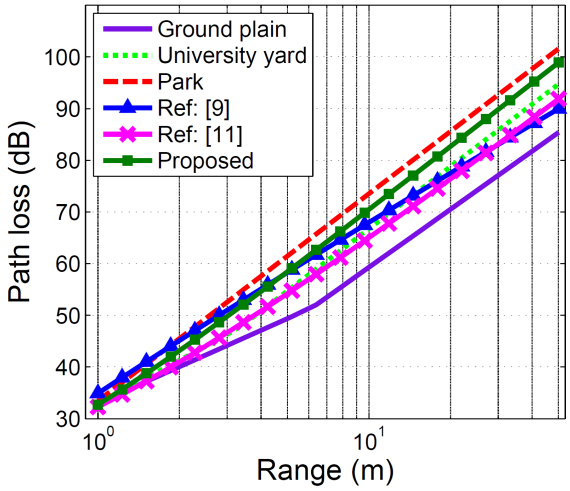

(b)

Figure 2.4: Comparison of the near-ground models predictions with measured data in open area. (a) Stationary measurements at distance of 75 m at 300 MHz ([42], Figure 12). Plots for h_t=0.87 m, h_t=1.15 m, and h_t=1.55 m are offset by 30 dB, 20 dB, and 10 dB, respectively, for illustration purposes; (b) Measurements at 868 MHz recorded in three diverse open environments ([31], Table 1).

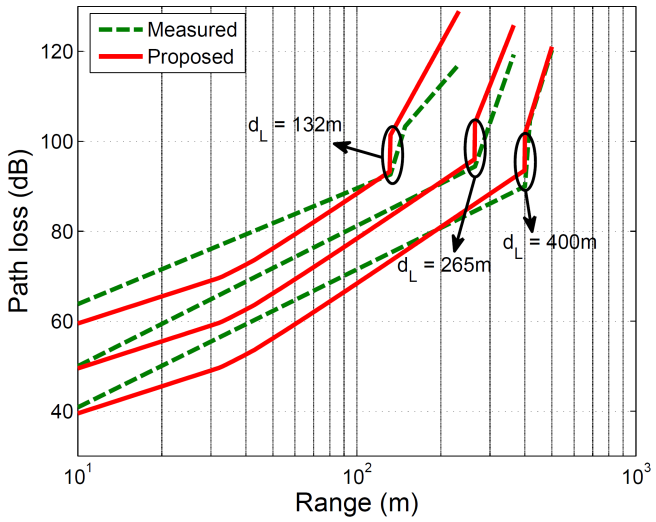

Figure 2.5: Model predictions versus measured path loss along an L-shaped urban route at 225 MHz ([43], Figures 5-7). Plots for d_L=265 m and d_L=132 m are offset by 10 dB and 20 dB, respectively, for illustration purposes.

factual basis. It is observed that the LOS path loss, the discontinuity in the signal level due to corner loss, and the NLOS steeper falloff rate are all predicted with a reasonable accuracy.

It is very common for wireless sensors to communicate through a depth of foliage. Several empirical models are proposed to account for the excess loss caused by the foliage. These models are generally based on experimental data acquired over a shallow depth of a specific type of vegetation. This suggests that they do not address the impact of density and texture of foliage as well as the propagation of lateral waves on the canopy-air interface. However, the latter phenomenon is only dominant at very large foliage depth which does not apply to WSN usage.

In Figure 2.6, some well-known empirical foliage loss models are added to near-ground

path loss model to evaluate their performance in low-altitude deployments. In Figure 2.6(a), measurements are recorded using discone antennas in a deciduous forest at the frequency of 300 MHz. Antennas height is 0.75 m [42]. Another measurement campaign is conducted in a tropical palm plantation using omnidirectional antennas at height of 2.15 m [34]. Measurements are taken at the frequencies of 240 MHz and 700 MHz and are depicted in Figure 2.6(b) and Figure 2.6(c), respectively. It is found that at a short range, predicted values of all the models are in good agreement with measured data. Nevertheless, Weissburger and ITU-R models predictions diverge sharply from the measured data as the range in the foliage increases. Predicted path loss using the FITU-R and LITU-R models match the measured data closely, especially at the lower antenna height of 0.75 m, which demonstrates their applicability to WSN design in forested areas.

2.4.2 Connectivity in near-ground WSNs

In this subsection, the near-ground path loss model is used in WSN design by evaluating the maximum transmission range of nodes and studying network connectivity via Monte Carlo simulations. Sensor motes in our simulations have a maximum transmission power of 10 dBm and receiver sensitivity of -101 dBm for a maximum dynamic range of 111 dB that are typical values for popular Mica2 motes [67]. Center frequency is 915 MHz unless otherwise specified.

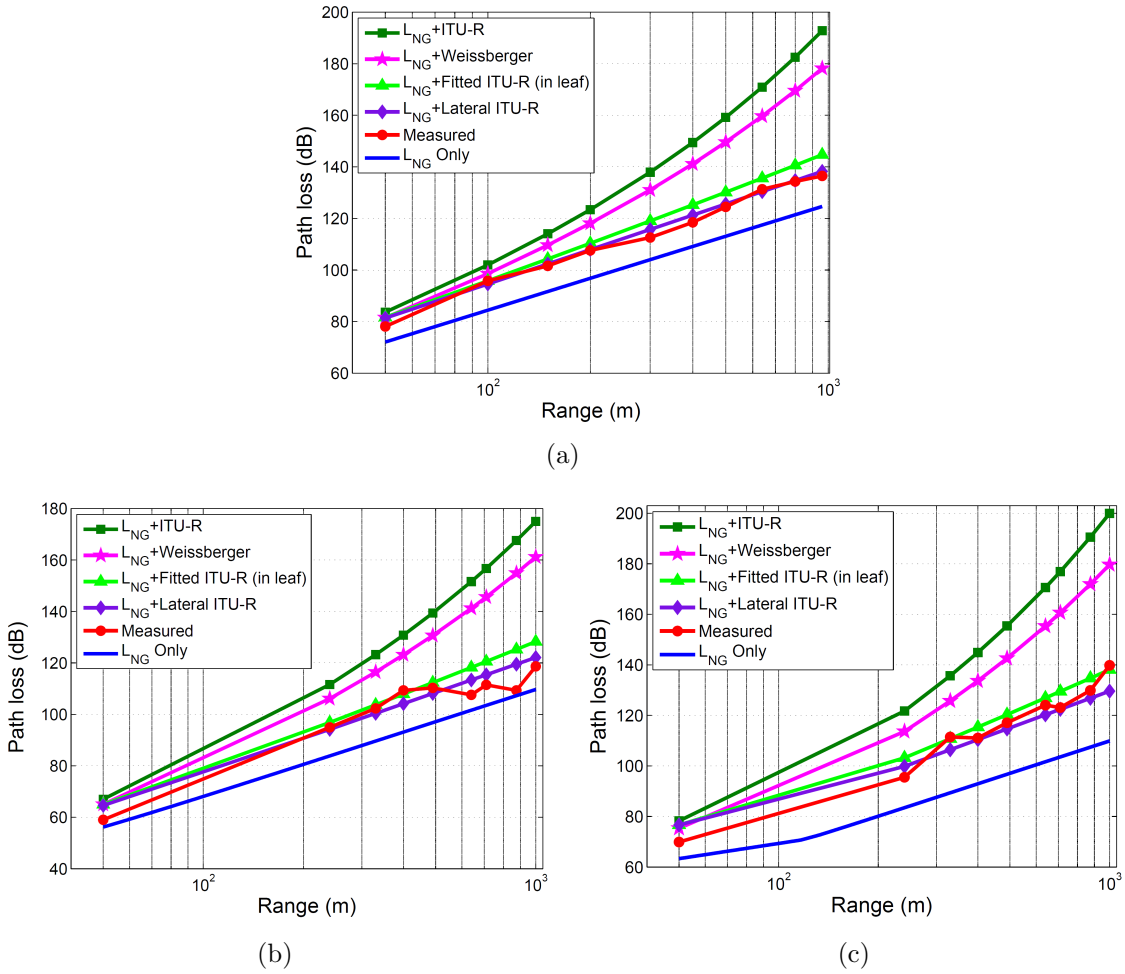

Figure 2.6: Measured and predicted path loss in forested areas. (a) h_a=0.75 m, f=300 MHz ([42], Figure 10(a)); (b) h_a=2.15 m, f=240 MHz ([34], Figure 4(a)); (c) h_a=2.15 m, f=700 MHz ([34], Figure 4(b)).

Maximum link range is found by equating the path loss and the dynamic range of motes. When path loss exceeds the dynamic range, the communication between nodes is lost. Evaluation of the coverage range is critical in sensor deployment to find the optimum node density for which the quality of service (QoS), scalability, and reliability requirements are met while the cost is minimized.

In Figure 2.7(a), coverage range is evaluated using different models introduced in section III, namely, the free-space model, the two-ray model and the near-ground model. Free-space model gives the unrealistically long coverage range of 4640 m independent of the terminals height and is not shown on the plot. The antenna height, h_a, is observed to have a prominent role in confining the coverage area and the maximum link range increases drastically when the antenna is elevated from the ground level. Comparing the results from the two-ray and the near-ground models, it is realized that incorporating the diffraction loss can significantly impact the link range, especially at lower altitudes. Closer to the ground level, antenna polarization also becomes important and it is seen that vertically-polarized antennas can communicate over longer distances. According to the plane-earth model, loss has no frequency dependence when $d \gg h_t, h_r$ [49]. However, it is shown in Figure 2.7(b) that lowering the antenna height undermines the frequency independence. To explain this observation, we note that in (2.20), with all the geometrical parameters fixed, the amplitude of higher order waves rise as the wavelength increases; hence, in order to improve network connectivity, we should lower the operating frequency which increases the communication range.

Figure 2.7(c) depicts the influence of soil volumetric water content (VWC) on the communication range. Water content has a major impact on the electrical properties of soil [68]. Silt loam with 17.16% sand, 63.84% silt, and 19% clay represents the

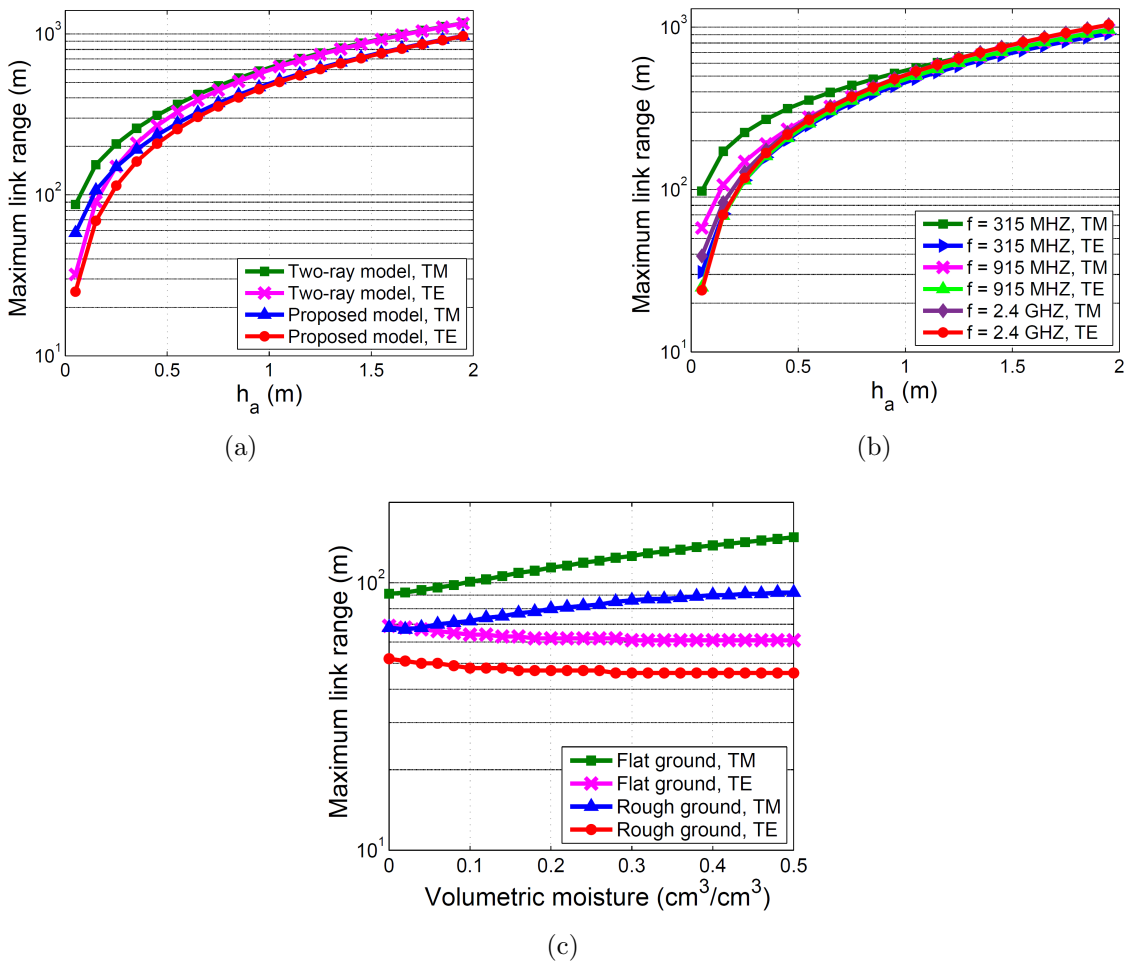

Figure 2.7: Mote transmission range: (a) versus antennas height using different models; (b) versus antennas height at different frequencies; (c) versus VWC over flat and rough ground.

terrain dielectric in this simulation and the antenna height is 10 cm. Using the well-known semi-empirical dielectric mixing model in [69, 70], we find that as the moisture content changes from 0 to 0.5 cm^3/cm^3, the dielectric constant of soil changes from ε=2.39 to ε=33.83-3.24i. This steep increase in the dielectric constant, however, only slightly alters the Fresnel reflection coefficient at grazing incidence. The amplitude

of the reflection coefficient will decrease (increase) slowly for vertical (horizontal) polarization as VWC increases it will remain very close to -1 which warrants the near cancellation of the direct and specularly reflected waves. It is perceived that even slight variation in the reflection coefficient causes a noticeable change in the coverage radius. Moreover, the plane-earth model tends to overestimate the coverage range compared to the near-ground model that takes surface irregularities into consideration.

In high-node-count applications such as environmental or security monitoring, a large number of low-cost autonomous sensors are spatially distributed to cooperatively monitor certain physical or environmental conditions. Here, mesh connectivity and the number of neighbors in range per node have a crucial influence on network performance, reliability and power conservation. In order to assess the average number of single-hop neighbors in range (average degree of a node) in the network, Monte Carlo simulations are used. In each iteration, 100 nodes are randomly distributed in the two-dimensional plane of 1000 ft$\times$1000 ft (304.8 m$\times$304.8 m) and average number of neighbors is calculated as the ratio of the total number of links within range to the number of nodes in the network. In Figure 2.8(a), different loss models are used to predict the average number of neighbors. Free-space model predicts full mesh connectivity, i.e., each node has 99 single-hop neighbors independent of terminals height. Vertical polarization yields far better connectivity at lower altitudes in comparison to horizontal polarization. It is also found that connectivity has high sensitivity to

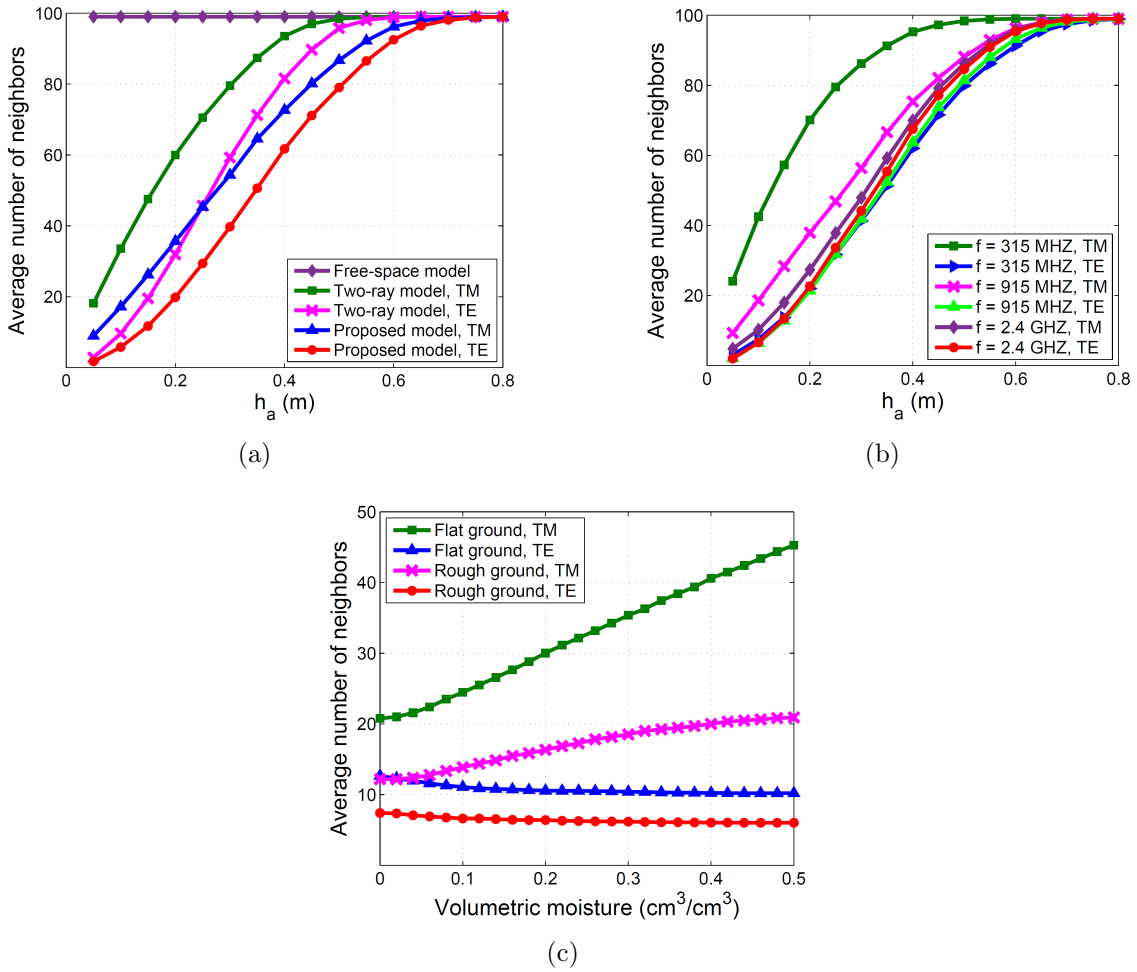

Figure 2.8: Average number of neighbors for a 100-node network with uniform topology: (a) versus antennas height using different models; (b) versus antennas height at different frequencies; (c) versus VWC over flat and rough ground.

terminal height and almost spans full range as height increases from the ground level to 0.8 m. Particularly, closer to the ground level, the height effect exacerbates. Figure 2.8(b) shows the impact of frequency on average number of neighbors. At lower frequencies, network connectivity is improved. In Figure 2.8(c), we study the effect of soil VWC on network connectivity. It is noticed that a fluctuating terrain degrades

network connectivity in contrast with a flat one. An interesting observation is that as soil moisture content increases, e.g. as a result of precipitation, connectivity enhances if the antennas are vertically polarized but deteriorates if the antennas are horizontally polarized. However, horizontally polarized antennas are minimally affected by change in roughness and dielectric properties of the ground.

2.5 Conclusion

An improved computationally feasible near-ground field prediction model is presented to facilitate highly accurate WSN simulations. The model is validated against published measured data in open, urban, and forested areas. It is observed that the proposed model has higher accuracy compared to existing near-ground analytical models. The increased precision is due to careful assessment of the impact of first Fresnel zone obstruction, terrain irregularities, and dielectric properties of the ground on the LOS, specular reflection and higher order waves. It is realized that the near-ground model applies to LOS urban topographies as well. Moreover, this model also works for NLOS urban scenario provided it is supplemented by a proper NLOS excess loss term. Various empirical foliage loss models are added to near-ground path loss model and compared to measured data in near-ground foliage environments to determine which one is more suitable for low-altitude applications.

The proposed model is also used to evaluate the effects of radio link and terrain parameters on the transmission range and network connectivity of WSNs. Some practical implications of this study include: (a) the critical distance is very small in WSN applications and, therefore, the diffraction loss is integral to WSN channel characterization; (b) at grazing angles, Fresnel reflection coefficient displays a very low sensitivity to terrain dielectric constant; (c) provided the geometrical parameters are fixed, higher order waves intensify as the wavelength increases; (d) antenna height is by far the most influential geometrical parameter to link range and network connectivity; (e) coverage radius and connectivity are fairly sensitive to the reflection coefficient when antennas are placed near the ground; (f) terrain roughness degrades the accessible range and connectivity; (g) lowering the frequency of operation, enhances the reachable communication distance and network connectivity; (h) close to the ground level, vertically polarized antennas outperform their horizontally polarized counterparts in terms of coverage range and connectivity; (i) precipitation boosts/reduces the maximum link range and network connectivity when motes are equipped with vertically/horizontally polarized antennas.

Chapter 3

Multiuser MIMO Channel Characterization over Random Rough Dielectric Terrain

3.1 Introduction

Effective deployment of wideband wireless technologies such as multi-input multi-output orthogonal frequency division multiplexing (MIMO-OFDM) systems requires proper understanding of spatial and temporal characteristics of wireless channels [1], [71]. The transceivers (TRx) in these systems do not have any information about the

power, delay, and direction of arrival of each individual path and instead require the aggregate descriptions of the propagation environment including the received power, power delay spread (DS) and power angular spread (AS). Angular dispersion has a major impact on capacity and diversity gain in multi-antenna systems, while it adversely affects the performance of beamforming techniques [72], [73]. In [74], the performance of space-frequency coded MIMO-OFDM is quantified as a function of propagation parameters. The length of cyclic prefix (CP) and fast Fourier transform (FFT) blocks are directly related to the channel delay spread [75]. In underspread channels, the size of CP and FFT can be decreased, which reduces latency and peak-to-average power ratio (PAPR) and increases power and bandwidth efficiency [76]. In [77], it is illustrated that for a given quality of service (QoS) in an OFDM system, as the channel delay spread increases, the required transmit power decreases. In addition, the authors in [78] prove that for most power allocation and scheduling schemes, OFDM network throughput increases at higher channel delay spread. In [79], a ray tracing (RT) simulator is utilized in an indoor setting, and it is verified that MIMO channel spatial dispersion can be well predicted using the angular spread. Moreover, channel capacity and spatial diversity order of antenna array systems improve by increasing the angle spread [80]. The study in [71] reveals that larger delay spread introduces a lower block error rate (BLER) and higher angular spread improves the BLER performance in a Long-Term Evolution (LTE) system. In [81], wideband channel measurements in two urban test sites are presented and compared to the results

of a commercial ray tracer and errors in the prediction of DS and AS are mainly attributed to limitations in the modeling of surface irregularities.

Multiuser MIMO (MU-MIMO) is a promising technology that uses a large excess of base station (BS) antennas to serve several user terminals in parallel in the same time-frequency resource [82]-[88]. When MIMO channel matrix entries are sufficiently independent, multiple spatial dimensions become accessible for signaling, which offers capacity and multiplexing gain. However, to achieve such a decorrelation, large inter-element spacing and a rich scattering environment are required [82]. MU-MIMO pulls together the distributed antennas at the user terminals to enjoy the advantages of MIMO in a much larger scale, even under difficult propagation conditions [35]. Hence, MU-MIMO is an ideal candidate 5G technology for highway and rural macrocell deployments where there is limited infrastructure and unfavorable propagation conditions. MU-MIMO can drastically increase the capacity by aggressive spatial multiplexing. It can also increase the energy efficiency by several orders of magnitude by concentrating power into small regions in space via beamforming [85], [89]. Such high energy efficiency makes it possible to power the base stations using solar or wind energy in areas where electricity grids are unavailable [90]. The maximum number of orthogonal pilot sequences is proportional to coherence time and bandwidth [87]. Fortunately, microwave MU-MIMO channels in open and rural environments exhibit high temporal stability and large coherence bandwidth, which increases the number

of available orthogonal pilots and reduces the sounding process overhead. Simulations at the personal communication services (PCS) band (1900 MHz) show that a billboard-sized base station array can provide 20 Mb/s service to 1000 rural homes [90]. In [88], a set of over the air experiments were conducted to evaluate the potential of UHF-band MU-MIMO to equip rural areas with high-speed WiFi over unused TV bands.

RT models are extensively used for indoor and outdoor propagation modeling [7], [18], [91], [92]. Conventional ray tracers render path loss well but neglect the diffuse component, which leads to inaccurate assessment of delay and angular profiles [93]. Rough surfaces diffusely scatter the incident power, which should be accounted for in channel characterization [18], [91]. Surface roughness has a random nature that is described using statistical techniques. Various techniques have been proposed to incorporate the dispersive effect of surface roughness in deterministic propagation prediction models [7], [18], [24], [27], [73], [94]. Analytical scattering formulations such as Kirchhoff approximation (KA) and small perturbation method (SPM) are two attractive options, which are readily implemented in a RT routine and offer fast approximate solutions under certain simplifying assumptions [25]. These powerful methods are capable of solving large three dimensional (3D) scattering problems with minimal computational cost and lend physical insight into the underlying scattering mechanisms [20], [22], [25], [28]. KA performs well for smoothly fluctuating surfaces with a large correlation length while SPM applies to surfaces with small roughness

and slopes [7], [20], [25], [28].

In [95], a one-dimensional (1D) rough surface is adopted to incorporate the effect of terrain irregularities on a near-ground link. [7] considers a 1D roughness to study the impact of diffuse scattering on inter-user and intra-user correlation of pair-wise channel coefficients in a MIMO system. However, using a 1D rough surface is inadequate when scattering outside the plane of incidence is desired [59]. In [18], KA is integrated into a ray model to derive the coverage maps in an office setting. Rough surfaces are modeled as perfect electric conductor (PEC), which disregards the electrical properties of indoor materials.

This chapter develops SPM and KA-based ray models to investigate the impact of geometrical parameters such as the TRx range and height, soil physical and electrical properties such as roughness, textural composition, and moisture content. Moreover, the impact of antenna parameters such as polarization and radiation pattern on terrain-based MU-MIMO channel characteristic parameters such as received power, power delay and angular profiles, RMS delay and angular spread, coherence bandwidth, and coherence distance are examined. In this study, random terrain roughness is assumed Gaussian with an exponential correlation function. The proposed ray models enable us to study the impact of soil textural composition in terms of sand, silt, and clay fractions and soil water content by adjusting the terrain dielectric constant. Different types of soil are considered and it is realized that the soil particle

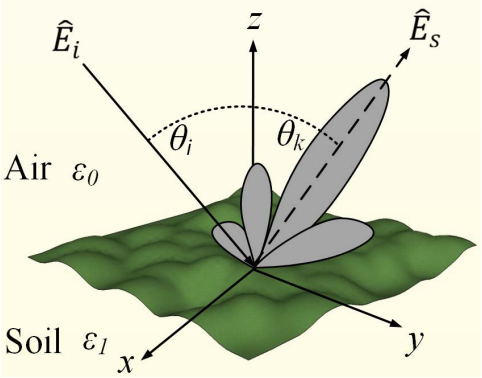

Figure 3.1: Basic geometry of scattering at a 2-D dielectric rough surface.

fractions and, more importantly, its volumetric moisture content can make a notable difference on the electrical properties of the terrain and, hence, the scattered power.

3.2 Mobile channel characterization

3.2.1 Small perturbation scattering model

The general scattering geometry from a dielectric rough surface is shown in Figure 3.1. Scattered power is divided into coherent and incoherent components. The coherent component dominates for small surface roughness. For large roughness, the coherent component vanishes and the incoherent part becomes more significant. Importance of diffuse scattering in multidimensional channel propagation modeling is highlighted in a recent study [91]. SPM is one of the most employed rough surface scattering solutions, which can be integrated in ray tracing models [20], [22], [25],

[28]. Derivation of the small perturbation theory is based on perturbative expansion of unknown scattering amplitude to an arbitrary order with respect to a small height parameter. Complexity of SPM solution increases steeply as the order of expansion increases but the accuracy of the predictions also improves [20], [28].

Here, SPM is applied to a 2D random rough surface in a 3D scattering geometry. The analyses includes bistatic scattering amplitudes up to the first order. SPM formulation used in this work is based on the extinction theory. Derivation details can be found in [20].

Consider a plane electromagnetic wave of the general form

$$\widehat{E}_i = \widehat{e}_i e^{(ik\widehat{k}_i\overline{r})} = \widehat{e}_i e^{(ik_{ix}x + ik_{iy}y - ik_{iz}z)} \tag{3.1}$$

is incident on a 2D dielectric rough surface. In (3.1), $\widehat{k}_i$ is the incident wave direction that is perpendicular to the electric field direction,$\widehat{e}_i$. $k = \omega\sqrt{\mu\varepsilon} = 2\pi/\lambda$ is the wavenumber in which ω is the angular frequency, μ is the permeability, ε is the permittivity, and λ is the wavelength. The position vector is $\overline{r} = x\widehat{x} + y\widehat{y} + z\widehat{z}$. Components of the wavenumber in the incident direction are $k_{ix} = k\sin\theta_i\cos\phi_i$, $k_{iy} = k\sin\theta_i\sin\phi_i$, and $k_{iz} = k\cos\theta_i$. The rough surface is characterized by a random height function $z = f(x, y)$ in which $f(x, y)$ is a random function with zero mean, i.e., $\langle f(x, y)\rangle = 0$.

In SPM, rough surface profile, $f(\overline{r}_\perp)$ where $\overline{r}_\perp = x\widehat{x} + y\widehat{y}$, and its derivatives are considered small parameters. These assumptions can be expressed as $k_z f(\overline{r}_\perp), k_{1z} f(\overline{r}_\perp) \ll 1$ and $df/dx, df/dy \ll 1$. The first expression ensures that surface variations are small compared to wavelength, while the latter guarantees that slopes are slight. Here, k_1 is the wavenumber of region 1 related to ε_1 (see Figure 3.1).

First, we consider the incident wave to be horizontally polarized, i.e., $\widehat{e_i} = \widehat{e}(-k_{iz})$. The zeroth-order scattered field is

$$E_s^{(0)}(\overline{r}) = R_h \widehat{e}(k_{iz}) e^{(i\overline{k}_{i\perp}\cdot\overline{r}_\perp + ik_{iz}z)} \tag{3.2}$$

In (3.2), R_h is the Fresnel reflection coefficient of TE waves:

$$R_h = \frac{(k_{iz} - k_{1iz})}{(k_{iz} + k_{1iz})} \tag{3.3}$$

k is the wavenumber of region 0, where the source is located, and k_1 is the wavenumber of region 1 (see Figure 3.1). We also have $\overline{k}_{i\perp} = k_{ix}\widehat{x} + k_{iy}\widehat{y}$. For the case of vertically polarized incident wave, i.e., $\widehat{e_i} = \widehat{h}(-k_{iz})$, zeroth-order solution is

$$E_s^{(0)}(\overline{r}) = R_v \widehat{h}(k_{iz}) e^{(i\overline{k}_{i\perp}\cdot\overline{r}_\perp + ik_{iz}z)} \tag{3.4}$$

where R_v is the Fresnel reflection coefficient of TM waves:

$$R_v = \frac{(k_1^2 k_{iz} - k^2 k_{1zi})}{(k_1^2 k_{iz} + k^2 k_{1zi})} \tag{3.5}$$

From (3.2) and (3.4) it is noticed that the zeroth-order solutions are the reflected waves from a flat surface.

For the case of horizontally and vertically polarized incident waves, the first order solutions are, respectively, derived as

$$\begin{aligned} E_s^{(1)}(\overline{r}) = & \int d\overline{k}_\perp e^{(i\overline{k}_\perp\cdot\overline{r}_\perp\cdot + ik_z z)} iF(\overline{k}_\perp - \overline{k}_{i\perp}) \\ & + [\widehat{e}(k_z) f_{ee}^{(1)}(\overline{k}_\perp, \overline{k}_{i\perp}) + \widehat{h}(k_z) f_{he}^{(1)}(\overline{k}_\perp, \overline{k}_{i\perp})] \end{aligned} \tag{3.6a}$$

$$\begin{aligned} E_s^{(1)}(\overline{r}) = & \int d\overline{k}_\perp e^{(i\overline{k}_\perp\cdot\overline{r}_\perp\cdot + ik_z z)} iF(\overline{k}_\perp - \overline{k}_{i\perp}) \\ & + [\widehat{e}(k_z) f_{eh}^{(1)}(\overline{k}_\perp, \overline{k}_{i\perp}) + \widehat{h}(k_z) f_{hh}^{(1)}(\overline{k}_\perp, \overline{k}_{i\perp})] \end{aligned} \tag{3.6b}$$

where $F(\overline{k}_\perp)$ is the Fourier transform of the rough surface profile, $f(\overline{r}_\perp)$. Furthermore, $f_{\alpha\beta}^{(1)}$ in which $\alpha, \beta = e, h$ are the first order scattering terms provided in [28]. First order solution also evaluates the depolarization of the received fields due to inclination

of the scattered rays. Thus, whenever non-local effects are negligible, first-order SPM (SPM1) is fairly accurate and higher-order expansions, which sharply increase the complexity of solutions, are unnecessary. We can find the total scattered electric field corresponding to a horizontally polarized incident wave by adding (3.2) and (3.6a). Similarly, adding (3.4) and (3.6b) leads to the total scattered field for a vertically polarized incident wave.

3.2.2 Kirchhoff approximation

KA is also known as tangent plane approximation (TPA) or physical optics (PO) theory. KA together with SPM are the oldest and the most prominent analytical approaches to study wave scattering from rough surfaces. SPM is suitable for small roughness heights at arbitrary low lateral scale of roughness, whereas KA is valid for any roughness height as long as the lateral scale of roughness is much larger than the wavelength, i.e., large curvature radii. In KA, tangent plane approximation is applied to calculate the surface fields, which results in relatively simple expressions for the scattering field intensities. Here, we briefly discuss the main properties of the model and derivation details can be found in [59].

The KA angular factor that incorporates the incidence and scattering angles as well as the reflection coefficient of the underlying surface into the scattered field equations

is defined as

$$F(\theta_i, \theta_k, \phi) = \frac{\upsilon_x \xi_x}{\upsilon_z \xi_z} + \frac{\upsilon_y \xi_y}{\upsilon_z \xi_z} + 1 \tag{3.7}$$

in which

$$\upsilon_x = k(\sin\theta_i - \sin\theta_k \cos\phi) \tag{3.8a}$$

$$\upsilon_y = -k(\sin\theta_k \sin\phi) \tag{3.8b}$$

$$\upsilon_z = -k(\cos\theta_i + \cos\theta_k) \tag{3.8c}$$

$$\xi_x = \sin\theta_i(1 - R_\alpha) + \sin\theta_k \cos\phi(1 + R_\alpha) \tag{3.8d}$$

$$\xi_y = \sin\theta_k \sin\phi(1 + R_\alpha) \tag{3.8e}$$

$$\xi_z = \cos\theta_k(1 + R_\alpha) - \cos\theta_i(1 - R_\alpha)\cdot \tag{3.8f}$$

$\phi = \phi_k - \phi_i$ and R_α is the Fresnel reflection coefficient of the flat surface where $\alpha = v, h$ denotes the vertical or horizontal incident polarization, respectively, given by (3.3) and (3.5). For a Gaussian surface, the expression derived for the scattering field intensity corresponds to [59]

$$\langle \rho\rho^* \rangle = e^{-g} \left[\rho_0^2 + \frac{\pi L^2 F^2}{A} \sum_{m=1}^{\infty} \frac{g^m}{m!m} e^{-\frac{\upsilon_{xy}^2 L^2}{4m}} \right] \tag{3.9}$$

where $\langle\rangle$ denotes statistical expectation. $A{=}l_x l_y$ is the area of the mean scattering surface. Surface dimensions are assumed much larger than the surface correlation

length for statistical stationarity that is necessary for stochastic handling of the scattering problem. ρ_0=sinc$\upsilon_x l_x$sinc$\upsilon_y l_y$ is the scattering coefficient of a plane surface of extent A in which $\mathrm{sinc}(x)=\sin(x)/x$. L is the correlation length of the roughness and $\upsilon_{xy}=\sqrt{\upsilon_x^2+\upsilon_y^2}$. $g=\sigma^2\upsilon_z^2$ is called the Ament coherent scattering loss factor that can be used to divide surfaces into three broad categories, namely, slightly, moderately, and very rough surfaces. Next, for each of these categories, the series solution in (3.9) is examined.

Slightly rough surfaces have $g \ll 1$, for which the series solution in (3.9) converges quickly and only the first term needs to be considered. Surfaces for which $g \approx 1$ are categorized as moderately rough. The series converges relatively slowly and several terms should be taken into consideration to obtain a solution. Surfaces for which $g \gg 1$ are regarded as very rough. This limit is sometimes referred to as deep phase modulation because the surface roughness drastically alters the phase of the scattered waves. In this case, series solution in (3.9) is of minimal use and the results in this limit may be obtained by considering geometrical optics (GO) theory as follows [20]

$$\langle \rho \rho^* \rangle = e^{-g} \left[\rho_0^2 + \frac{\pi L^2 F^2}{Ag} e^{g - \frac{\upsilon_{xy}^2 L^2}{4g}} \right] \tag{3.10}$$

To derive the scattering field expression, it is assumed that surface has no infinite gradient and surface dimensions are much larger than surface correlation length, L,

which is in turn much larger than λ. Shadowing effect is also included in our model using a shadowing function that has been widely used to modify the bistatic scattering coefficients [96]

$$S(\theta_i, \theta_k) = [1 + \Lambda(\theta_i, s) + \Lambda(\theta_k, s)]^{-1} \tag{3.11}$$

in which

$$\Lambda(\theta, \sigma) = \frac{1}{2}\left[\sqrt{\frac{2}{\pi}}\frac{s}{\cot\theta}\exp(-\frac{\cot^2\theta}{2s^2}) - \text{erfc}(\frac{\cot\theta}{\sqrt{2}s})\right] \tag{3.12}$$

s is the mean surface slope defined as $s = \sqrt{2}\sigma/l$ for a Gaussian rough surface [20]. erfc is the complementary error function.

3.2.3 Ray tracing simulations

Two self-programmed ray tracing routines based on SPM and KA are developed in this study. Evaluation of the diffuse energy is subject to the following assumptions: (1) incident electric field is plane and linearly polarized; (2) antennas are located in the far-field of the rough terrain; (3) antenna elements are omni-directional point radiators; (4) side lengths of the scattering tiles are much larger than the roughness correlation length to ensure statistical stationarity, i.e., $l_x, l_y \gg L$ [18], [28]; (5) rough surface profile has a Gaussian height distribution; (6) surface roughness is statistically isotropic; (7) surface slopes are gentle, i.e., $df/dx, df/dy \ll 1$; (8) for SPM, terrain irregularities are assumed small, i.e., $|k_z f(\overline{r}_\perp)|, |k_{1z} f(\overline{r}_\perp)| \ll 1$ [20], [28]; (9) for KA,

correlation length is much larger than the wavelength, i.e., $L \gg \lambda$ [20], [28]; (10) in SPM, impact of multiple scattering and shadowing are neglected, while in KA shadowing is included.

As shown in Figure 3.2, to implement the scattering formulation in the RT model, the computational domain is divided into small tiles whose side lengths are 20 surface correlation lengths. Now, the wave propagated from the point source can locally be assumed plane. Amplitude of the plane incident wave is calculated at the center of each tile and maintained constant over the entire surface of the tile. This representation reduces the spherical wavefront to a locally plane one so that the formulation of SPM and KA can be applied to calculate the diffusely scattered energy from each tile. Next, to find the total scattered field, the contribution from all segments with different phases and directions of arrival are summed at the observation point.

Both RT tools generate 2D random rough surfaces with normal height distribution. They can deal with vertical and horizontal incident polarizations. The proposed models consider a dielectric terrain instead of a PEC that is an important improvement compared to similar tools, e.g., [7], [18]. Furthermore, the depolarization of scattered waves is taken into account. Thus, impact of electrical properties of the terrain on the communication channel that has been underestimated in the previous studies can be closely investigated.

Scattering tiles are characterized by their lengths in x and y directions, l_x and l_y,

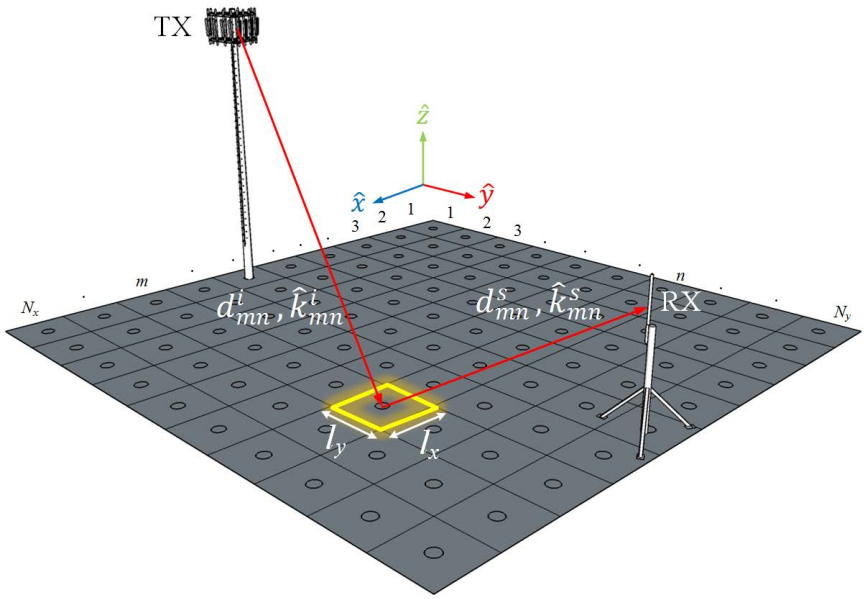

Figure 3.2: Calculation of geometric parameters of each scattering tile such as the center point location, distance from Tx/Rx, and incidence/emergence angles.

respectively, surface RMS height, σ, roughness correlation length, L, and effective permittivity, ε_r, of the underlying dielectric layer. σ represents the standard deviation of the height of the rough surface irregularities in terms of wavelength. L is the distance between two statistically independent points on the surface and is a measure of the density of the surface variations. ε_r is a function of the soil texture, moisture content, frequency, and temperature.

3.2.4 Soil parameters

To study the impact of soil textural composition and moisture content on the wireless channel parameters, a dielectric mixing model is required to describe the macroscopic

dielectric behavior of the soil system. The soil mixture is comprised of solid soil particles, water and air voids. Depending on the particle size, soil solids are classified as sand for particles with diameters in the range of 0.05 and 2.0 mm, silt including the soil particles of diameters in the 0.002 to 0.05 mm range, and clay for particles with diameters smaller than 0.002 mm [97]. Textural composition refers to soil solids fractions. The water contained in the soil is divided into bulk water and bound water. Bound water molecules are held firmly by the soil particles and are located in the first few molecular layers adjacent to the particle surfaces referred to as the Stern layer. Bulk water or free water molecules are located in the so-called Gouy layer and are far enough from the soil particles to freely move within the soil medium. Due to the forces acting on a bound water molecule, it exhibits a distinct dielectric dispersion spectrum from a free water molecule, which leads to dissimilar interaction with electromagnetic waves. The ratio of the bound water to free water is proportional to soil specific surface area A_s. Clayey soil has a higher A_s and, therefore, higher bound water quotient, whereas sandy soil has a lower A_s and, thus, a higher free water quotient.

The model exploited in this work is a widely used semi-empirical dielectric mixing model of the form [98], [99]:

$$\varepsilon = \varepsilon^{'} - i\varepsilon^{''} = 1.15 \left[1 + \frac{\rho_b}{\rho_s}(\varepsilon_s^{\alpha} - 1) + m_v^{\beta'} \varepsilon_{fw}^{'\alpha} - m_v \right]^{1/\alpha} - 0.68 - i \left[m_v^{\beta''} \varepsilon_{fw}^{''\alpha} \right]^{1/\alpha} \tag{3.13}$$

in which

$$\varepsilon_s = (1.01 + 0.44\rho_s)^2 - 0.062 \tag{3.14a}$$

$$\beta^{'} = 1.2748 - 0.519S - 0.152C \tag{3.14b}$$

$$\beta^{''} = 1.33797 - 0.603S - 0.166C \tag{3.14c}$$

$$\varepsilon^{'}_{fw} = \varepsilon_{\omega\infty} + \frac{\varepsilon_{\omega 0} - \varepsilon_{\omega\infty}}{1 + (2\pi f \tau_\omega)^2} \tag{3.14d}$$

$$\varepsilon^{''}_{fw} = \frac{2\pi f \tau_\omega (\varepsilon_{\omega 0} - \varepsilon_{\omega\infty})}{1 + (2\pi f \tau_\omega)^2} + \frac{\sigma_{eff}(\rho_s - \rho_b)}{2\pi f \varepsilon_0 \rho_s m_v} \tag{3.14e}$$

$$\sigma_{eff} = 0.0467 + 0.2204\rho_b - 0.4111S + 0.6614C \tag{3.14f}$$

$$\tau_\omega = 1.768 \times 10^{-11} - 6.086 \times 10^{-13}T + 1.104 \times 10^{-14}T^2 - 8.110 \times 10^{-17}T^3 \tag{3.14g}$$

where ε is the relative dielectric constant of the soil mixture with real part $\varepsilon^{'}$ and imaginary part $\varepsilon^{''}$; m_v=$\rho_b m_g$ is the volumetric moisture content; m_g=W_w/W_d is the gravimetric moisture content; ρ_b=W_d/V is the bulk density of the dry soil in grams per cubic centimeter, which can be found using [39]; ρ_s is the specific density of solid soil particles; W_d, W_w, and V are the weight of the dry soil, weight of water, and volume of soil mixture sample, respectively; ε_s is the dielectric constant of the soil solids; α=0.65 is an empirically determined constant; $\beta^{'}$ and $\beta^{''}$ are texture-dependent empirically determined constants; S and C are the mass fractions sand and clay, respectively; ε_{fw} is the relative permittivity of water with real part $\varepsilon^{'}_{fw}$ and imaginary part $\varepsilon^{''}_{fw}$; $\varepsilon_{\omega 0}$=80.1 is the static dielectric constant of water; $\varepsilon_{\omega\infty}$=4.9 is the optical limit of

dielectric constant of water; f is the frequency in Hertz; $\varepsilon_0 = 8.854 \times 10^{-12}\, F/m$ is the permittivity of free space; σ_{eff} is the effective conductivity of the soil mixture; τ_ω is the relaxation time of water that is equal to 9.231×10^{-12} at room temperature, $20°C$; T is the temperature in Celsius.

3.3 Results and discussion

In this section, the proposed SPM ray model is used to analyze the effects of surface statistical and electrical properties on the received power, power azimuth spectrum, RMS delay and angle spread, coherence bandwidth, and coherence distance. Next, KA ray model is used to study the impact of antenna directivity and polarization, and carrier frequency in a terrain-based MU-MIMO communication system.

A typical scattering environment is presented in Figure 3.2. Here, the rough surface is Gaussian with exponential correlation function. The computational domain is typically $500 \times 500L^2$, in which L is the correlation distance that is segmented into a total of 25×25 tiles in x and y directions. Side lengths of each tile is $20L$, which is large enough to provide a locally planar phase-front for the incident wave and ensures the stationarity of the rough surface [28].

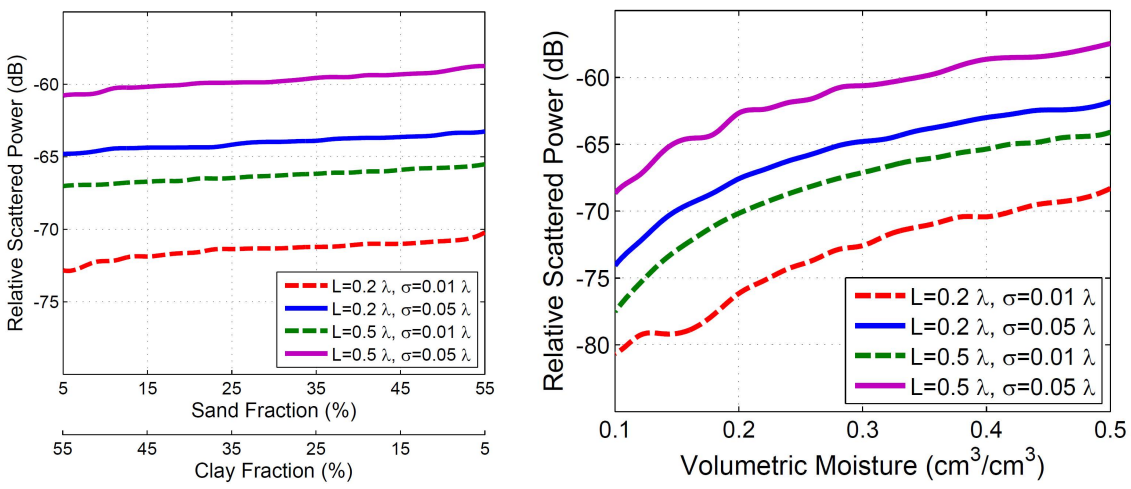

Figure 3.3: (a) Scattered power versus sand (clay) fraction; (b) Scattered power versus volumetric moisture content.

The simulation parameters for SPM ray model are as follows, unless otherwise specified: 100 random rough surfaces are generated for Monte Carlo simulations; TE polarization is assumed; Tx antenna height is 50λ while Rx element height is 10λ and both are isotropic radiators; silt loam with 17.16% sand, 63.84% silt, and 19.00% clay represents the terrain dielectric. Typically, a dry silt loam with $0.05\,cm^3/cm^3$ volumetric moisture content corresponding to a relative permittivity of ε=3.7+0.3i at 900 MHz and a wet one with $0.3\,cm^3/cm^3$ volumetric moisture content corresponding to a relative permittivity of ε=16.8 + 1.8i at 900 MHz are used in the simulations.

In Figure 3.3(a), we study the effect of soil solids composition on the power scattered from the terrain. Here, TM polarization is assumed. Dry soil solids exhibit the same dielectric features while wet soil systems show very distinct dielectric properties [97];

hence, relatively high water content of $0.3\,cm^3/cm^3$ is assumed so that the impact of altering soil solid fractions on scattered power manifests itself better. Soil textural composition impacts scattered energy at Rx via changing the macroscopic dielectric behavior of the soil medium. In the simulation setup, silt fraction is fixed at 40%, while sand and clay fractions sweep an identical range of 5% to 55%. As the sand content increases from 5% to 55%, dielectric constant of the soil system changes from ε=$16.12 + 2.93i$ to ε=$22.55 + 1.48i$. It is observed that increasing the sand content, increases the scattered power. Moreover, we notice that the scattered power increases by increasing the undulations height or increasing the surface correlation length.

Figure 3.3(b) depicts the influence of moisture content on the received power. The scenario is similar to the latter case but here we choose a specific soil particle distribution and alter the volumetric moisture content. A textural class with a higher A_s and, therefore, a higher clay fraction is picked so that the effect of adding water to the soil system is clearly observed. Silty clay with 5.02% sand, 47.60% silt, and 47.38% clay represents the terrain dielectric in this case. As the moisture content changes from 0.1 to $0.5\,cm^3/cm^3$, the dielectric constant of soil changes from ε=$5.02 + 0.87i$ to ε=$32.60 + 4.50i$. Increasing the moisture content noticeably boosts the scattered power [100]. It is illustrated that increasing the water content from 0.1 to $0.5\,cm^3/cm^3$ leads to an almost 10 dB increase in the scattered power. At this point it becomes clear that considering the impact of dielectric soil system is crucial and any result derived from a PEC ground is subject to major errors. It is also observed that the

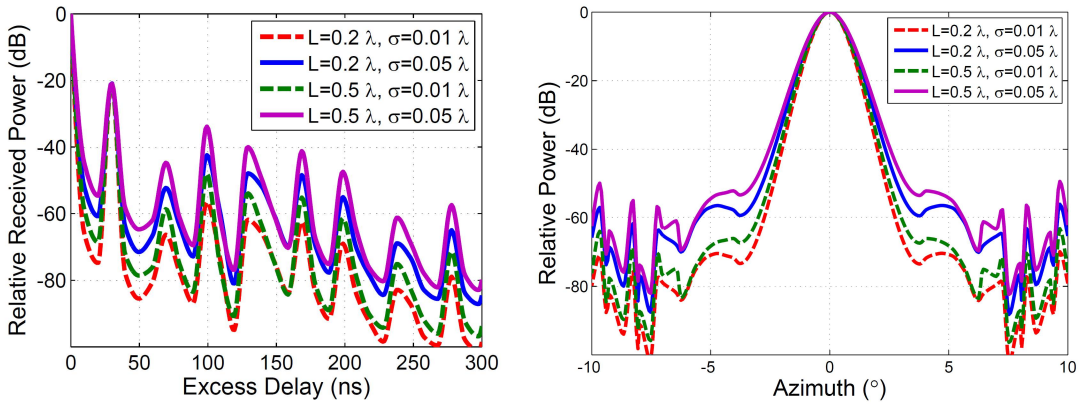

(a) (b)

Figure 3.4: (a) Normalized relative received power versus the excess delay for different correlation distances and undulation heights; (b) Power azimuth spectrum for various correlation distances and surface roughness heights.

scattered power increases by increasing the undulations height and increasing the surface correlation length, which is in agreement with the previous result.

To study the effects of surface undulation height and correlation length on power delay profile, polynomial regression fits of the normalized received power are plotted versus excess delay in Figure 3.4(a). Here, TRx distance is 100λ, Tx height is 50λ and Rx height is 10λ. The received power from the LOS path is normalized to 0 dB and all other multipath components including the reflected power are normalized accordingly. The Plot suggests that as surface roughness and surface correlation length increase, the power of multipath components augments, which is attributed to the wider spread of the scattered power on the rough terrain [7].

In Figure 3.4(b), power azimuth spectrum of a rough terrain is evaluated. Here, the

set up is similar to Figure 3.4(a); the power received from the direct path is suppressed because we are merely interested in the effect of surface roughness on power azimuth spread. The received power from the specular reflection path is normalized to 0 dB and all other multipath components are normalized accordingly. It is observed that as roughness increases, more energy is received from incoherent paths, which is in agreement with our observation in Figure 3.4(a). Moreover, it is noted that the contribution of non-specular components in the total received power increases as undulation height increases. It is found that increasing surface roughness increases the RMS delay and angular spread, while it decreases the coherence bandwidth. The direct path component has a significant impact on decreasing the RMS delay and angular spread, and increasing the coherence bandwidth. Further, varying the surface correlation length exercises a weaker influence on the RMS delay spread and coherence bandwidth compared with varying the undulation height [101]. Figure 3.5 demonstrates the effect of TRx distance on LOS azimuth angular spread at the mobile station (MS) side. Advantages of MIMO technology lies in the addition of spatial diversity. Inspecting the AS is vital as it determines the coherence distance that in turn specifies the antenna spacing required to achieve higher rank gain matrices in multi-antenna systems. In Figure 3.5(b), as the TRx distance increases, angular spread decreases. It is also observed that higher roughness height always leads to higher angular spread. When TRx distance increases, the scattered power decreases much faster than the direct power. Hence, the mean value of K increases with

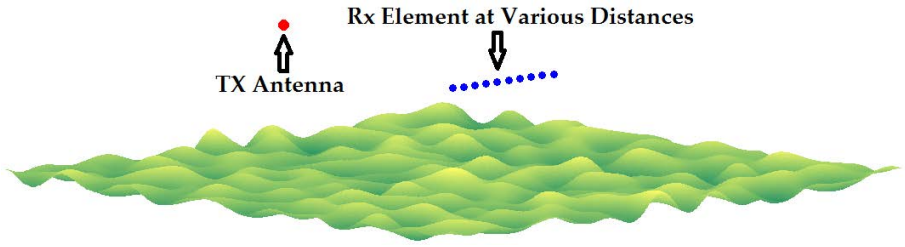

(a)

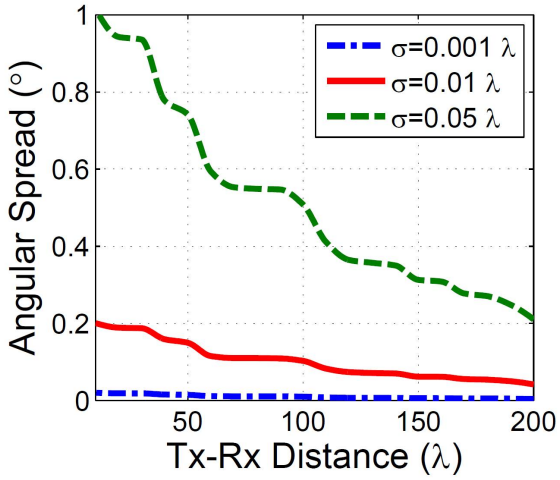

(b)

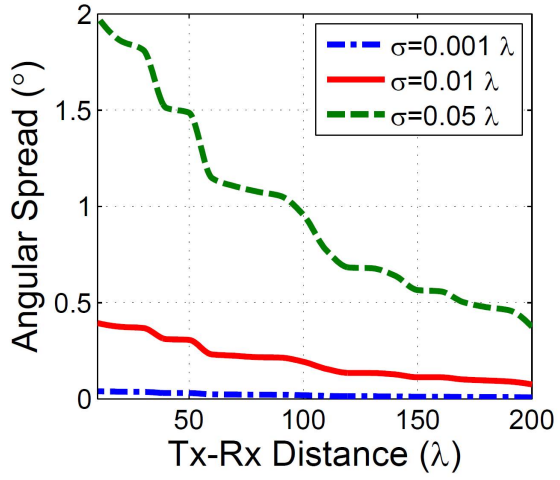

(c)

Figure 3.5: Impact of TRx position on azimuth angular spread. (a) Simulation setup; (b) $m_v = 5\%$; (c) $m_v = 30\%$.

distance, in which K is the ratio of the direct power to diffuse power, leading to reduction of the angular spread. Figure 3.5(c) reveals the impact of soil moisture on the AS. It is realized that increasing m_v from 5% to 30% widens the AS by almost two-fold, which is mainly attributed to the amplification of the scattered field strength from rough terrain. Figure 3.6 illustrates the impact of Rx height on LOS azimuth angular spread at the MS side for two different water volume contents. The distance is 50λ. As Rx height increases, AS decreases. This effect is brought about by an increase in K similar to the previous case. Table 3.1 offers a qualitative summary of the impacts of geometrical and electrical parameters on channel properties that are examined in this study. It is noted that electrical properties of the soil system modifies the phase angle of the scattered field as well as the ratio of the energy received from direct and indirect paths that in turn alters the temporal and angular distribution of power in the LOS scenario.

In the next step, KA ray model is used to simulate a terrain-based MU-MIMO communication system. Antenna arrays are simulated using directional horn antennas. The transmit array is either isotropic or directional with a directionality of 25 dBi and horizontal beamwidth of 10 degrees. The receive antenna is assumed isotropic. Transmit and receive beams are assumed perfectly aligned. Terrain dielectric is $\varepsilon{=}\varepsilon_r - i60\kappa\lambda$ where for average ground the dielectric constant is $\varepsilon_r{=}15$, conductivity

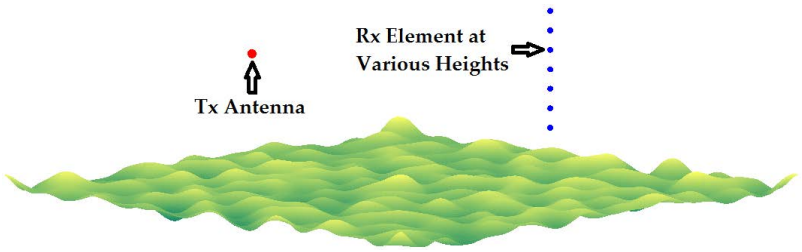

(a)

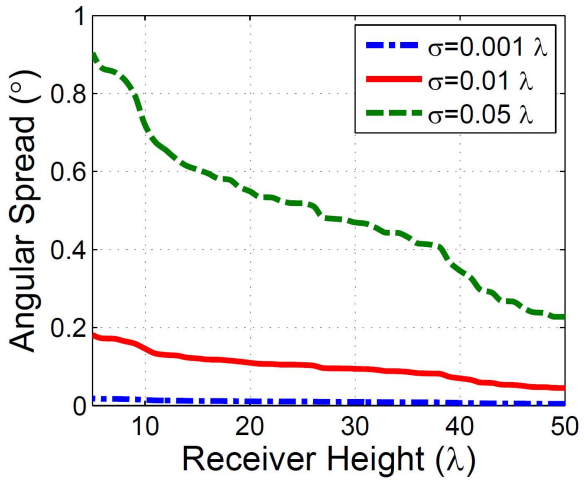

(b)

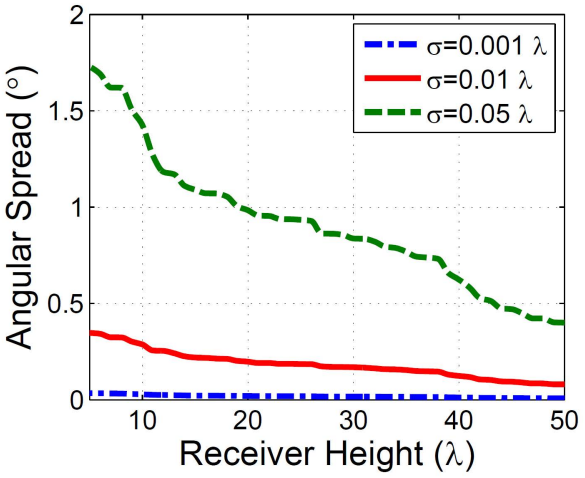

(c)

Figure 3.6: Impact of Rx height on azimuth angular spread. (a) Simulation setup; (b) $m_v = 5\%$; (c) $m_v = 30\%$.

Table 3.1
Summary of effects of radio link and terrain parameters on channel properties

Parameter	1	2	3	4	5	6	7	8	9	10	11
Diffuse Power	∅	⇩	⇩	⇧	⇧	⇩	⇧	⇧	⇧	⇧	⇩
RMS Delay Spread	⇩	⇩	⇩	⇧	⇧	⇩	⇧	⇧	⇧	⇧	⇩
RMS Angular Spread	⇩	⇩	⇩	⇧	⇧	⇩	⇧	⇧	⇧	⇧	⇩
Coherence Bandwidth	⇧	⇧	⇧	⇩	⇩	⇧	⇩	⇩	⇩	⇩	⇧
Coherence Distance	⇧	⇧	⇧	⇩	⇩	⇧	⇩	⇩	⇩	⇩	⇧

1. Line of Sight (LOS) Signal
2. Tx-Rx Distance
3. Tx/Rx Height
4. Roughness RMS Height (σ)
5. Roughness Correlation Length (L)
6. Frequency of Operation
7. Temperature
8. Soil Moisture Content (m_v)
9. Soil Bulk Density
10. Wet Soil Sand Fraction
11. Wet Soil Clay Fraction

Symbols represent the following:
⇧ = positive correlation
⇩ = negative correlation
∅ = independent

is κ=0.005 $mhos/m$, σ=1.13 cm is the roughness RMS height, and surface correlation length is L=7.39 cm [50], [64]. Simulation frequencies are 300 MHz, 900 MHz, and 2.6 GHz; access point height is 10 m unless otherwise stated; user equipment height is 1.5 m. Figure 3.7(a) studies the effect of antenna directionality and carrier frequency on the received power. TM polarization is assumed. Directional beamforming antennas at the base station have a directionality of 25 dBi, while the receive antenna is isotropic. Beamforming not only decreases the path loss, but also reduces the power fluctuations around the median received signal especially for shorter links.

This is because when directional antennas are used, most of scatterers fall outside the antennas beamwidth and, therefore, transceivers do not see them. Moreover, at lower frequencies, path loss median and oscillations are diminished. Figure 3.7(b) shows that the dips and valleys are larger for TE polarization, which indicates higher scattered power (see [102], page 221). Increasing antenna heights also flattens the received power curve, as depicted in Figure 3.7(c). At lower angles, in conformity with Rayleigh criterion, the terrain surface appears electrically smoother that leads to higher reflection and larger interference with the direct component.

Figure 3.8 demonstrates the impact of antenna polarization, carrier frequency, and base station height on the chip power in NLOS links versus separation of the terminals. First column in each plot represents the power received from the specular direction, whereas the remainder of power is received from scatterers around the specular direction. Figure 3.8(a) serves as our reference and in each of the subsequent plots one of the simulation parameters is altered while the others are kept unchanged to study the impact of each parameter individually. When terminals are moved away from each other, both the reflection and scattered powers decrease. However, the scattered power falls off much faster because it is inversely proportional to the squared product of distances between scatterers and terminals while the reflected power is inversely proportional to the squared addition of those distances [103]. As the carrier frequency decreases, the surface appears electrically smoother, so the specular power increases,

while the diffuse power decreases. Lowering the access point height increases the incidence angles on the rough terrain, which reduces the scattered power. Nonetheless, at small ranges, this reduction is compensated by bringing the scatterers closer to the Tx. Figure 3.8(d) shows that the scattered power is less for TM polarized antennas compared to TE polarized antennas (see [68], page 437). The Brewster effect along the specular direction is also noticeable. Power delay profile (PDP) is used to compute the RMS delay spread, which is an important measure that impacts inter symbol interference (ISI) and determines achievable frequency diversity of wireless channels. Figure 3.9 illustrates the non-line-of-sight RMS DS versus range for various antenna directionalities and polarizations. The directional link is equipped with a transmit array with a directionality of 25 dBi. Most of scatterers, especially those located at shorter distances, fall outside the beamwidth of the directional transmit antenna. This drastically reduces the RMS DS and hence increases the channel coherence bandwidth. Moreover, at higher frequencies and higher access points, the RMS DS increases.

3.4 Conclusion

In this work, SPM and KA are implemented in a ray tracing algorithm to study the effect of terrain physical properties and antenna radiation pattern and polarization on the propagation loss, delay and angular spread, and bandwidth of a MU-MIMO

channel. Dielectric properties of the underlying surface are also included in the proposed model to further improve the accuracy of ray tracing simulations. The main conclusions of this study are as follows: (a) Higher surface RMS height increases the incoherent component of the scattered field and decreases the coherent component; (b) increasing TRx distance decreases the received power; (c) as the height of Tx and/or Rx increases, effect of surface roughness on the received power diminishes; (d) increasing the fraction of larger particles in the soil mixture boosts the scattered power; (e) increasing the soil moisture content augments the scattered power; (f) increasing undulations height has a noticeable impact on increasing the RMS delay and angular spread that increases the channel frequency selectivity and decreasing the coherence distance; (g) channel bandwidth has a higher sensitivity to the variation of surface roughness height rather than surface correlation distance; (h) directional antennas boost the received power and coherence bandwidth; (i) increasing the carrier frequency reduces the received power and coherence bandwidth; (j) the scattered power and the delay spread are larger for TE polarized antennas.

This study highlights the significance of diffuse scattering in multiuser multi-antenna communication channels with applications in highway and rural macrocells, wireless sensor networks for environmental monitoring, near ground communication between TRx working above a dielectric rough terrain, and body surface to external device channel modeling. Future work will investigate the impacts of multilayer dielectric roughness and ground proximity on the performance of multi-antenna systems.

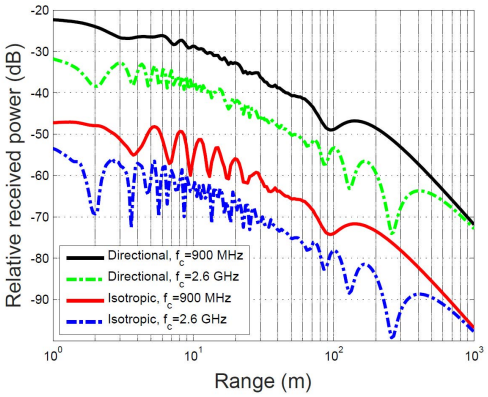

(a)

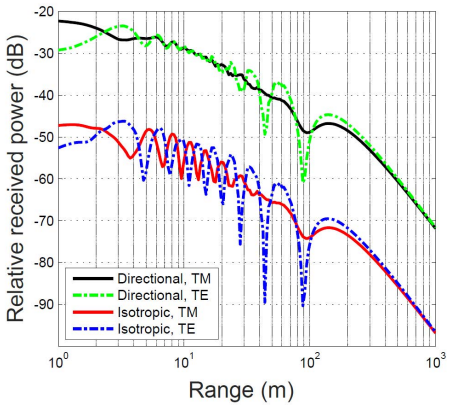

(b)

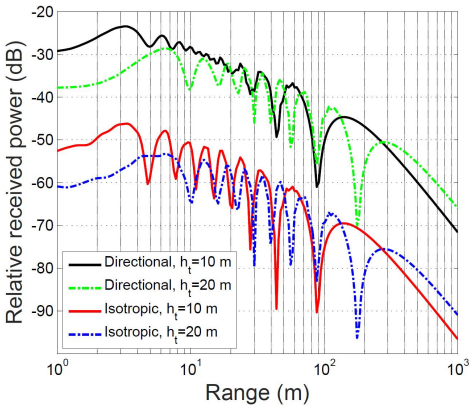

(c)

Figure 3.7: Path loss versus terminal separation for directional and isotropic antennas. (a) Effect of carrier frequency; (b) effect of polarization; (c) effect of base station height.

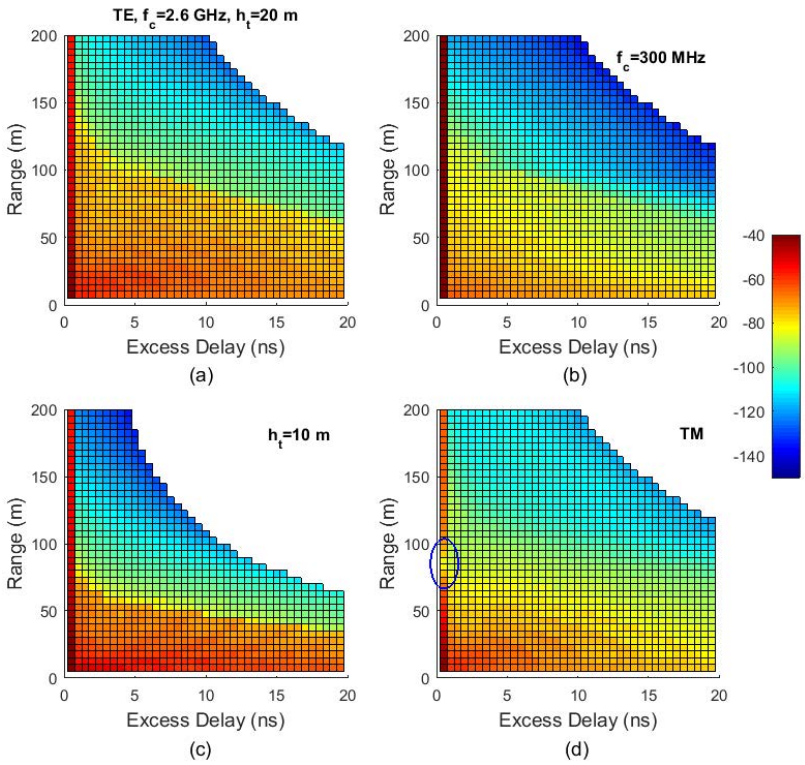

Figure 3.8: The sequence of NLOS PDPs (in dBm) versus the range. First columns represent the specularly reflected power. (a) Reference plot: TE polarization, $f_c = 2.6GHz$, $h_t = 20m$; (b) frequency reduced to $f_c = 300MHz$; (c) Base station height is lowered to $h_t = 10m$; (d) TM polarization. Note the Brewster effect along the specular reflection.

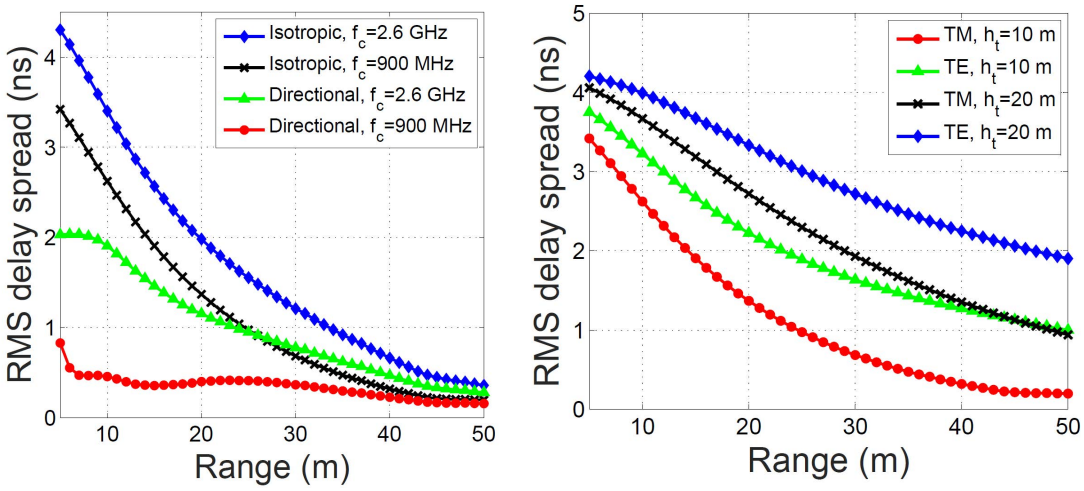

(a) (b)

Figure 3.9: NLOS RMS DS versus range for various antenna directionalities and polarizations. (a) At different carrier frequencies; (b) for different Tx heights.

Chapter 4

Millimeter Wave Directional Channel Modeling for Small Cells

4.1 Introduction

Fifth generation (5G) wireless communication networks are envisaged to support exponentially higher traffic volumes by exploiting ultra-dense small cell deployments, large spectrum allocations, and highly directional antennas [35], [90]. Modulation and channel coding techniques can be used to increase spectral efficiency up to the Shannon limit. However, by exploiting higher carrier frequencies, higher data rates and service quality can be achieved [36]. Moreover, reducing the access point coverage

area decreases the average distance between base station (BS) and user equipment (UE) and improves spatial frequency reuse. Hence, deployment of wide scale small cell access points is a prevailing trend toward improving the area spectral efficiency and enhancing energy efficiency [104].

Millimeter wave (mmW) frequencies between 30GHz and 300GHz have been proposed for outdoor small cells [37], [38], [105]. These frequencies offer much greater spectrum allocations and enable the placement of a large number of antenna elements in small form factors [89]. Extensive research has been conducted to model indoor propagation for mmW frequency ranges [18], [106]-[108], but minimal data exists concerning wide area outdoor propagation [38], [105], [109], [110]. In [109]-[111], simple ray-tracing (RT) models are developed to analyze mmW multi-input multi-output (MIMO) capacity for outdoor mesh backhaul in picocellular networks. However, wireless propagation is supposed to be dominated by a line-of-sight (LOS) component and a few strong specular reflections and LOS blockage and scattering effects are neglected. Measurements at 28 GHz in New York City confirm that even in non-LOS (NLOS) scenarios, mmW picocellular networks offer more than 30 times higher capacity compared to current cellular LTE systems [37]. In a theoretical study, average data rate for mmW systems is predicted to be 50 times more compared to microwave systems [112]. Measurements conducted in suburban Austin, Texas at 38GHz confirms that cell sizes in the order of 200 m is achievable for mmW communications, particularly at lower BS heights [36]. Signal penetration and reflection properties of

common building materials are studied via measurements at 28 GHz in [113]. It is observed that common indoor materials such as clear glass and drywall cause lower attenuation while penetration loss of mmWs through outdoor building materials such as brick and tinted glass is high. Hence, the interference between indoor and outdoor mmW networks is minimal.

Surface roughness generates diffuse scattering that reduces specular reflectivity and results in angular dispersion of radio waves. Diffuse scattering effects are particularly important in characterization of wireless channels at mmW frequency spectrum. Note that in mmW range, an undulation height in the order of millimeters is electrically very rough. Several approaches have been proposed to incorporate dispersive effects of surface roughness in deterministic propagation prediction models [7], [18], [38], [92], [114]. To include the diffusely scattered fields, an efficient surface scattering formulation should be employed in a ray tracing model. Kirchhoff approximation (KA) is a widely used analytical method in the study of wave scattering from random rough surfaces [20], [25], [28]. Impact of surface roughness on the performance of open-area terrain-based communication systems are investigated in [92], [115]. The authors in [7] propose a simple MIMO channel model in which scatterers are modeled as one-dimensional (1D) random rough surfaces. However, scattering and reflection from the ground plane as well as multiple wall reflections are ignored and antennas are assumed omnidirectional. In addition, in three-dimensional (3D) channel characterization it is important to evaluate the scattering outside the plane of incidence; a 1D model

is not accurate in off-plane directions unless the roughness under study is truly 1D [115]. In [18], surface roughness is integrated into a ray model to study the impact of diffuse scattering in indoor environments at THz frequencies.

Full-dimension MIMO (FD-MIMO) uses two-dimensional (2D) arrays to house large number of antennas in a small form factor [90]. To exploit these antennas efficiently, accurate 3D channel models are needed to address the impact of elevation angles. Prospect of deploying multi-antenna techniques such as beamforming and spatial multiplexing in the elevation dimension requires further study. All realistic wireless channels experience multipath propagation. In a scattering environment, several waves arrive at the elements of an antenna array through different angles with different phases, which reduces the correlation of signals received across antenna elements [1]. Uncorrelated channel responses are essential for spatial diversity to combat fading and for spatial multiplexing to improve bit rate in multi-antenna systems [14].

4.2 Problem definition

4.2.1 Geometry

Figure 4.1 depicts the scattering environment in a typical multiuser scenario where an access point (AP) is simultaneously transmitting symbols to UE1 and UE2. Here,

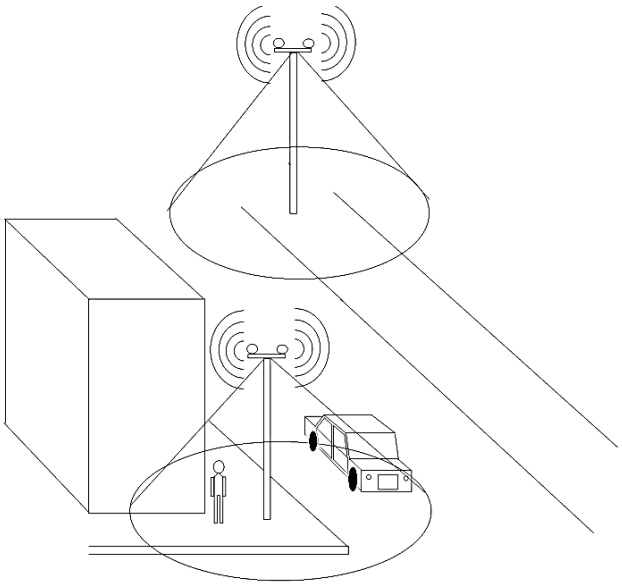

Figure 4.1: Outdoor small cell scenario.

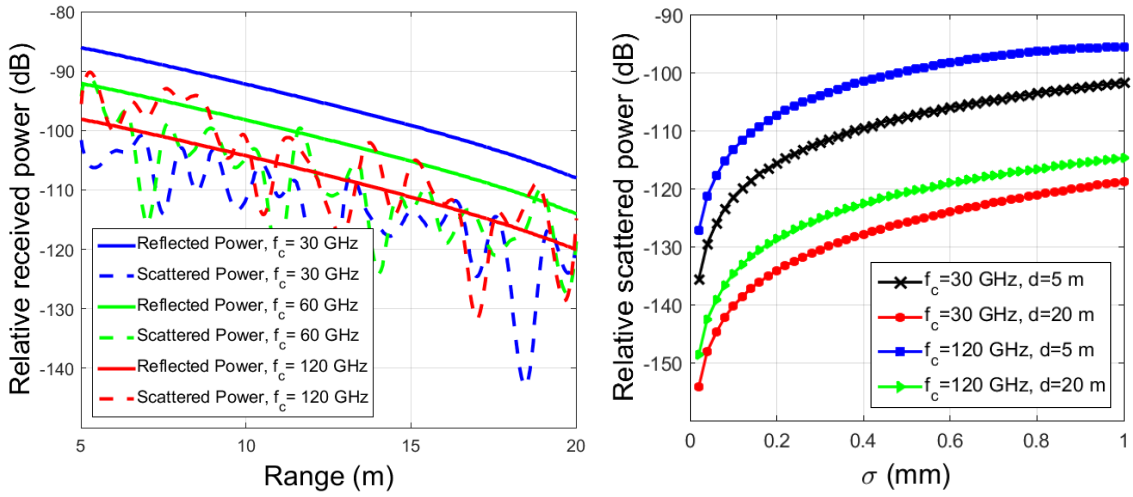

(a) (b)

Figure 4.2: Scattering from a rough ground. (a) Comparison of reflected and scattered power; (b) scattered power versus surface roughness height.

access points are deployed on lampposts and transmit data to users within their coverage area.

At mmW frequencies, diffuse scattering has a significant impact on the channel behavior and should be taken into account. Figure 4.2 depicts the scattered power from a rough ground that is calculated using an advanced surface scattering model known as the integral equation method (IEM) [116]. Figure 4.2(a) compares the amplitude of specularly reflected and diffusely scattered powers from the rough ground at three frequencies within the mmW range. For the dielectric, we consider $\varepsilon = \varepsilon_r - j60\kappa\lambda$ where the dielectric constant is ε_r=15, conductivity is κ=0.005 mhos/m, and λ is wavelength at the simulation frequency. The normally distributed roughness is characterized by its rms height σ=1.00 mm and correlation length T=25 λ. It is noted that as the frequency increases, the scattered power becomes comparable to and even exceeds the reflected power. Figure 4.2(b) suggests that the diffuse power increases with the roughness height. Diffuse power is especially prominent at higher frequencies and lower ranges, which are attributes of mmW small cells.

4.2.2 Ray tracing algorithm

In this work, Kirchhoff approximation is included in the ray tracing routine to calculate the diffusely scattered power from rough urban surfaces. To implement the Kirchhoff scattering theory in ray tracing algorithm, the surface is partitioned into scattering tiles or scatterers with equal side length of 10 times the surface correlation

length, as schematically represented in Figure 4.3. Therefore, the incident wave radiated from a point source is considered locally plane with invariable amplitude over the whole surface of a scatterer. Segmentation of the rough surface reduces the spherical wave emitted from the source to a locally plane one that can be handled by Kirchhoff equations to calculate the diffuse field scattered from each segment. Choosing the number of tiles is a compromise between accuracy and computational burden. To our advantage, energy scattered by the rough surface is mainly confined to a narrow angle around the specular direction, which in turn bounds the computational domain on the rough surface [20]. The scattering tiles are symmetrically placed about the specular reflection point. For isotropic roughness, it is reasonable to lay an equal number of tiles in both directions. Next, to find the diffusely scattered component, the contribution from all segments are summed at the observation point.

In addition, in the KA-based ray model multiple wall reflections up to 20^{th} order are incorporated. Reflected components will be modified by antenna gain patterns, the Fresnel reflection coefficient, and the Ament loss factor, which will be discussed later.

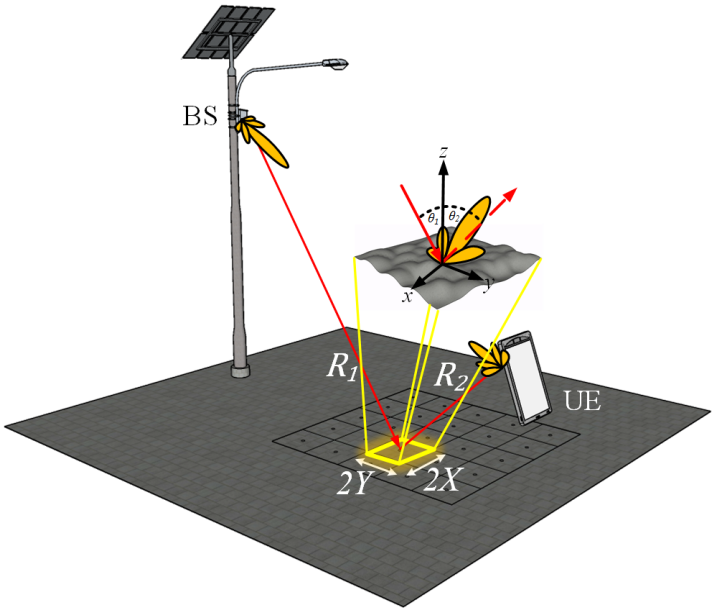

Figure 4.3: Schematic implementation of Kirchhoff formulation in a ray-tracing model.

4.2.3 LOS and NLOS channel matrices

NLOS channel matrix is represented as [117]

$$H_1^{NLOS} = \left[e_r\left(\phi_{r1}\right)\cdots e_r\left(\phi_{rP}\right)\right] \times \begin{bmatrix} a_1 & \cdots & 0 \\ \vdots & \ddots & \vdots \\ 0 & \cdots & a_P \end{bmatrix} \times \begin{bmatrix} e_t^T\left(\phi_{t1}\right) \\ \vdots \\ e_t^T\left(\phi_{tP}\right) \end{bmatrix}$$

$$= \sum_{p=1}^{P} a_p G_r\left(\phi_{rp}, \theta_{rp}\right) G_t\left(\phi_{tp}, \theta_{tp}\right) e_r\left(\phi_{rp}\right) e_t^T\left(\phi_{tp}\right) \tag{4.1}$$

in which p denotes a multipath component (MPC) with coefficient a_p that forms the angles of departure (AoD) ϕ_{tp} and θ_{tp} with the transmit antenna array and angles of

arrival (AoA) ϕ_{rp} and θ_{rp} with the receive antenna array. In addition, $e_t(\phi_{tp})$ and $e_r(\phi_{rp})$ are, respectively, the transmit array and receive array phase shift vectors for the p^{th} MPC, which depend on the array configurations. Effects of antenna directivities are included in $G_t(\phi_{tp}, \theta_{tp})$ and $G_r(\phi_{rp}, \theta_{rp})$. As an example, for the special case of horizontal uniform linear arrays with inter-element spacing d_t and d_r (normalized to λ) at the Tx and Rx, respectively, channel coefficients from BS antenna element l to UE1 antenna element k under NLOS and LOS conditions correspond to

$$h_{1,(kl)}^{NLOS} = \sum_{p=1}^{P} a_p g_{rp}(\phi_{rp}, \theta_{rp}) g_{tp}(\phi_{tp}, \theta_{tp}) \times e^{-i2\pi(d_r(k-1)\sin\phi_{rp} + d_t(l-1)\sin\phi_{tp})} \tag{4.2}$$

$$h_{1,(kl)}^{LOS} = a_0 + h_{1,(kl)}^{NLOS} \tag{4.3}$$

respectively. Here, $a_0 = \lambda e^{-2\pi/\lambda d_1}/(4\pi d_1)$ is the LOS coefficient and d_1 is the distance between BS and UE1. In terms of the Rice factor, K, which is the ratio of the LOS power to the NLOS power, the LOS coefficient is expressed as $a_0 = \sqrt{K_1 E\left[\left|h_{1,(kl)}^{NLOS}\right|^2\right]} e^{-2\pi/\lambda d_1}$. The latter expression for a_0 is particularly useful in evaluating the impact of partial blockage of LOS energy on channel parameters. $E[\cdot]$ denotes statistical expectation and $|\cdot|$ is absolute value. Similar quantities can be derived for UE2. Channel matrix for UE2 can be written as

$$H_2^{NLOS} = \sum_{p=1}^{P} b_p G_r(\psi_{rp}, \alpha_{rp}) G_t(\phi_{tp}, \theta_{tp}) e_r(\psi_{rp}) e_t^T(\phi_{tp}) \tag{4.4}$$

To analyze inter-user spatial correlation, it is conventional to assume that the two users are co-located and share the same scattering landscape. Thus, the scatterers contributing to the transmission between BS and UE1 are also contributing to the transmission between BS and UE2. Note that H_1^{NLOS} and H_2^{NLOS} share the same AoD, ϕ_{tp} and θ_{tp}, because signal is directed from BS to the same scatterers. However, scattered energy reaches UE1 and UE2 at different angles with distinct amplitudes, therefore, their path coefficients and their AoA differ. Here, the normalized pair-wise intra-user and inter-user spatial correlation coefficients are respectively defined as follows: Intra-user

$$R_{1,(kl,mn)}^{NLOS} = \frac{E\left(h_{1,(kl)}^{NLOS} h_{1,(mn)}^{NLOS*}\right)}{E\left(\left|h_{1,(kl)}^{NLOS}\right|\right) \cdot E\left(\left|h_{1,(mn)}^{NLOS}\right|\right)} \tag{4.5}$$

$$R_{1,(kl,mn)}^{LOS} = \frac{E\left(h_{1,(kl)}^{LOS} h_{1,(mn)}^{LOS\ *}\right)}{E\left(\left|h_{1,(kl)}^{LOS}\right|\right) \cdot E\left(\left|h_{1,(mn)}^{LOS}\right|\right)} \tag{4.6}$$

Inter-user

$$R_{1,2,(kl,mn)}^{NLOS} = \frac{E\left(h_{1,(kl)}^{NLOS} h_{2,(mn)}^{NLOS*}\right)}{E\left(\left|h_{1,(kl)}^{NLOS}\right|\right) \cdot E\left(\left|h_{2,(mn)}^{NLOS}\right|\right)} \tag{4.7}$$

$$R_{1,2,(kl,mn)}^{LOS} = \frac{E\left(h_{1,(kl)}^{LOS} h_{2,(mn)}^{LOS\ *}\right)}{E\left(\left|h_{1,(kl)}^{LOS}\right|\right) \cdot E\left(\left|h_{2,(mn)}^{LOS}\right|\right)} \tag{4.8}$$

When the extent of scatterers is much greater than the surface correlation length, $X, Y \gg T$, their surface height distributions become independent, which leads to

uncorrelated scattering [28], i.e.,

$$E\left[a_i a_j^*\right] = 0,\ E\left[b_i b_j^*\right] = 0,\ E\left[a_i b_j^*\right] = 0,$$
$$\text{For } i \neq j \quad i, j = 1, 2, \cdots, P \tag{4.9}$$

As an example, for the special case of horizontal uniform linear arrays, using (4.2) and assuming uncorrelated scattering, we can write

$$E\left(h_{1,(lk)}^{NLOS} h_{1,(mn)}^{NLOS*}\right)$$
$$= \sum_{p=1}^{P} E\left[a_p a_p^*\right] g_{rp}^2\left(\phi_{rp}, \theta_{rp}\right) g_{tp}^2\left(\phi_{tp}, \theta_{tp}\right) \times e^{-i2\pi(d_r(k-m)\sin\phi_{rp} + d_t(l-n)\sin\phi_{tp})} \tag{4.10}$$

$$E\left(h_{1,(lk)}^{NLOS} h_{2,(mn)}^{NLOS*}\right)$$
$$= \sum_{p=1}^{P} E\left[a_p b_p^*\right] g_{rp}\left(\phi_{rp}, \theta_{rp}\right) g_{rp}\left(\psi_{rp}, \alpha_{rp}\right) g_{tp}^2\left(\phi_{tp}, \theta_{tp}\right)$$
$$\times e^{-i2\pi(d_r((k-1)\sin\phi_{rp} - (m-1)\sin\psi_{rp}) + d_t(l-n)\sin\phi_{tp})} \tag{4.11}$$

Similar expressions can be found for other terms in (4.5)-(4.8). Next, intra-user and inter-user spatial correlation coefficients, $E\left[a_p a_p^*\right]$ and $E\left[a_p b_p^*\right]$, will be evaluated.

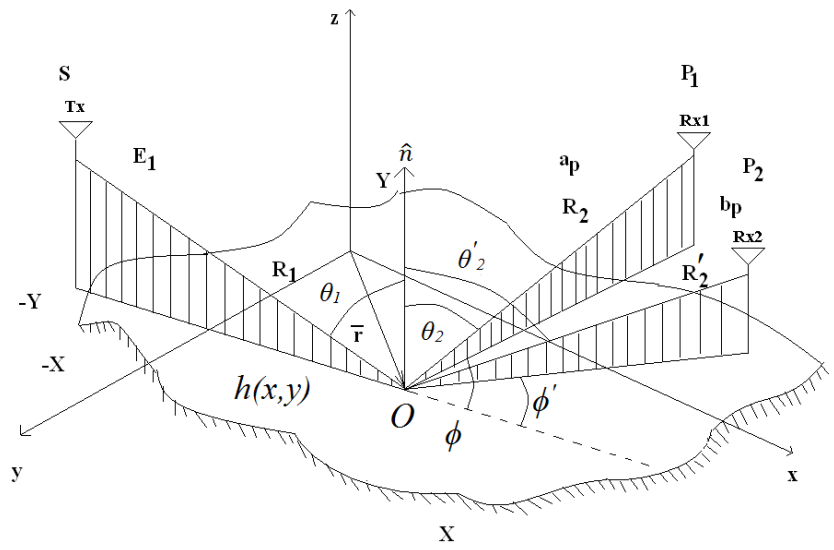

Figure 4.4: Basic geometric notations for incidence and emergence angles from a scattering tile.

4.3 Theoretical evaluation

This section examines the diffuse field statistics from a random rough surface to analytically evaluate the correlation of the field scattered by scatterer p at two distinct directions, $E\left[a_p b_p^*\right]$. Next, $E\left[a_p a_p^*\right]$ is evaluated as a special case when the two directions coincide. In this work, KA is applied to a 3D problem with 2D random rough surfaces. To evaluate the statistics of the scattered field amplitude, a statistical description of the scattering surface is required. Rough surfaces are characterized by a random height function $z = h(x, y)$, in which $h(x, y)$ is a Gaussian random function with zero mean and $\bar{r} = x\hat{x} + y\hat{y} + z\hat{z}$ is the position vector on the surface.

As shown in Figure 4.4, a rectangular scattering tile extends over $-X \leq x \leq X$

and $-Y \leq y \leq Y$ centering at O. $A = 4XY$ is the mean scattering surface area. Surface dimensions are assumed much larger than the surface correlation length to maintain statistical stationarity (surface rms height may be taken as stationary) that is necessary for stochastic handling of the scattering problem. Source is located at S in the far field from all points on the scattering surface, i.e., $R_1 \gg A/\lambda$ [118]. Hence, the incident wave is assumed a plane electromagnetic wave with electric field of the form $E_1 = E_0 e^{-ikR_1}$ where $k = \omega\sqrt{\mu\varepsilon} = 2\pi/\lambda$ is the incident wavevector. The angle of incidence is represented by θ_1. We also assume observation points, P_1 and P_2, are located in the far field of the scattering tile, i.e., $R_2, R'_2 \gg A/\lambda$. The path coefficient at P_1 is represented by a_p and the angles θ_2 and ϕ denote its scattering angle relative to the z axis and its azimuth angle relative to the incidence plane, respectively. Similarly, the path coefficient at P_2 is represented by b_p and the angles θ'_2 and ϕ' specify the corresponding scattering direction. Hereafter, primed quantities are associated with P_2 and can be determined by replacing appropriate angles.

KA angular factor, which incorporates the incidence and scattering angles as well as reflection coefficient of the underlying surface into the scattered field equations is defined as [28]

$$F(\theta_1, \theta_2, \phi) = \frac{v_x \xi_x}{v_z \xi_z} + \frac{v_y \xi_y}{v_z \xi_z} + 1 \tag{4.12}$$

in which

$$v_x = k\left(\sin\theta_1 - \sin\theta_2\cos\phi\right) \tag{4.13a}$$

$$v_y = -k\left(\sin\theta_2\sin\phi\right) \tag{4.13b}$$

$$v_z = -k\left(\cos\theta_1 + \cos\theta_2\right) \tag{4.13c}$$

$$\xi_x = \sin\theta_1\left(1 - R_\alpha\right) + \sin\theta_2\cos\phi\left(1 + R_\alpha\right) \tag{4.14a}$$

$$\xi_y = \sin\theta_2\sin\phi\left(1 + R_\alpha\right) \tag{4.14b}$$

$$\xi_z = \cos\theta_2\left(1 + R_\alpha\right) - \cos\theta_1\left(1 - R_\alpha\right) \tag{4.14c}$$

R_α is the Fresnel reflection coefficients of a flat surface where $\alpha = v, h$ denotes vertical and horizontal incident polarizations, respectively, given by

$$R_v = \frac{k_1^2 k_{iz} - k^2 k_{1zi}}{k_1^2 k_{iz} + k^2 k_{1zi}} \tag{4.15a}$$

$$R_h = \frac{k_{iz} - k_{1zi}}{k_{iz} + k_{1zi}} \tag{4.15b}$$

k is the wavenumber in the air and k_1 is the wavenumber in the dielectric. k_{iz}/k_z is the normal component of the wavenumber in the incident/scattered direction with $k_z = k\cos\theta$. The normalized scattering coefficient corresponding to a_p is defined as $\rho = a_p/a_{p0}$, where a_{p0} is the field reflected specularly by a flat surface of the same

extent with the same angle of incidence at the same distance, which corresponds to

$$a_{p0} = \frac{ike^{-ik(R_1+R_2)}A\xi_z}{4\pi R_2} = \frac{ie^{-ik(R_1+R_2)}A\xi_z}{2\lambda R_2} \tag{4.16}$$

Hence, we can write the scattered field in terms of the scattering coefficient

$$a_p = \frac{ike^{-ik(R_1+R_2)}A\xi_z}{4\pi R_2}\rho = \frac{ie^{-ik(R_1+R_2)}A\xi_z}{2\lambda R_2}\rho \tag{4.17}$$

Similarly, the relationship between the scattered field b_p and its coefficient ρ' is expressed as

$$b_p = \frac{ike^{-ik(R_1+R'_2)}A\xi'_z}{4\pi R'_2}\rho' = \frac{ie^{-ik(R_1+R'_2)}A\xi'_z}{2\lambda R'_2}\rho' \tag{4.18}$$

To simplify the subsequent derivations, we study the statistics of the scattering coefficients instead of a_p and b_p. Using (4.17) and (4.18), we write

$$E\left[a_p b_p^*\right] = \frac{e^{-ik(R_2-R'_2)}A^2\xi_z\xi'_z}{4\lambda^2 R_2 R'_2}E\left[\rho(\rho')^*\right] \tag{4.19}$$

$$E\left[a_p a_p^*\right] = \frac{4A^2\xi_z^2}{\lambda^2 R_2^2}E\left[|\rho|^2\right] \tag{4.20}$$

ρ is calculated using the general Kirchhoff solution for the field and its derivative on the surface in the Helmholtz formulation of rough surface scattering

$$\rho = \frac{F}{A}\iint_A e^{i\bar{v}.\bar{r}}dxdy \tag{4.21}$$

where F is the angular factor, A is the area of the mean scattering surface, and $\bar{v} = (v_x\hat{x}, v_y\hat{y}, v_z\hat{z})^T$. The assumptions made in deriving (4.21) are: 1) Source and observation points are in the far field of the surface; 2) the incident wave is plane and linearly polarized; 3) coupling between different wave polarizations are neglected; 4) no point on the surface has infinite gradient; 5) mutual interaction of the roughness irregularities are disregarded. Now, we intend to evaluate

$$E\left[\rho(\rho')^*\right] = \mathrm{cov}\left(\rho, \rho'\right) + E\left[\rho\right] E^*\left[\rho'\right] \tag{4.22}$$

$\mathrm{cov}\left(\rho, \rho'\right)$ is the covariance of ρ and ρ'. Substituting (4.21) in (4.22) and assuming a Gaussian roughness, we have

$$\begin{aligned}\mathrm{cov}\left(\rho, \rho'\right) = \frac{FF'}{A}\int_0^\infty \int_0^{2\pi} e^{iv_x\tau\cos\phi + iv_y\tau\sin\phi} \\ \times\left[\chi_2\left(v_z, -v'_z\right) - \chi\left(v_z\right)\chi^*\left(v'_z\right)\right]\tau d\tau d\phi \end{aligned} \tag{4.23a}$$

$$E\left[\rho\right]E^*\left[\rho'\right] = \chi\left(v_z\right)\chi^*\left(v'_z\right)\rho_0{\rho'}_0 = e^{-g_1}\rho_0{\rho'}_0 \tag{4.23b}$$

where $F = F\left(\theta_1, \theta_2, \phi\right)$ and $F' = F\left(\theta_1, \theta'_2, \phi'\right)$ are are the angular factors corresponding to observation points P_1 and P_2, respectively. $\chi\left(v_z\right)$ is the characteristic function of a rough surface that is defined as the Fourier transform of its probability density function. For a Gaussian surface,

$$\chi\left(v_z\right) = \exp\left(-g/2\right) \tag{4.24}$$

where $g = \sigma^2 v_z^2$ is called the Ament coherent scattering loss factor [28]. $\chi_2\left(v_z, -v'_z\right)$ is the 2D characteristic function. For a stationary Gaussian surface,

$$\chi_2\left(v_z, -v'_z\right) = \exp\left(-g_1 + g_2 C\left(\tau\right)\right) \tag{4.25}$$

in which $C(\tau) = \exp\left(-\tau^2/T^2\right)$ is the surface correlation length, $g_1 = (g + g')/2 = \sigma^2\left(v_z^2 + v_z^{2\prime}\right)/2$ and $g_2 = \sqrt{gg'} = \sigma^2 v_z v'_z$. $\rho_0 = \operatorname{sinc} v_x X \operatorname{sinc} v_y Y$ is the scattering coefficient of a plane surface of extent A and $\operatorname{sinc}(x) = \sin(x)/x$. To obtain (4.23a), isotropic surface statistics is assumed to allow evaluation of the surface integration in spherical coordinates. Making the substitution

$$e^{g_2 C(\tau)} = \sum_{m=0}^{\infty} \frac{g_2^m}{m!} [C(\tau)]^m \tag{4.26}$$

χ_2 may be expanded as

$$\chi_2\left(v_z, -v'_z\right) = e^{-g_1} \sum_{m=0}^{\infty} \frac{g_2^m}{m!} e^{-\frac{m\tau^2}{T^2}} \tag{4.27}$$

The series in (4.26) only converges when the argument of the exponential is less than unity that sets restrictions upon utility of the expansion in (4.27), which will be discussed shortly. Note that the term of order zero in (4.27) equals $\chi\left(v_z\right)\chi^*\left(v'_z\right)$.

Substituting (4.27) into (4.23a) yields

$$\begin{aligned}\operatorname{cov}(\rho,\rho') &= \frac{FF'}{A}e^{-g_1} \\ &\times \sum_{m=1}^{\infty}\frac{g_2^m}{m!}\int_0^{\infty}\int_0^{2\pi} e^{i(v_x\cos\phi+iv_y\sin\phi)\tau}e^{-\frac{m\tau^2}{T^2}}\tau d\tau d\phi \end{aligned} \tag{4.28}$$

Applying

$$\int_{\theta}^{\theta+2\pi} e^{\pm ix\cos\phi\pm iy\sin\phi}d\phi = 2\pi J_0\left(\sqrt{x^2+y^2}\right) \tag{4.29}$$

to (4.28) leads to

$$\operatorname{cov}(\rho,\rho') = \frac{2\pi FF'}{A}e^{-g_1}\times\sum_{m=1}^{\infty}\frac{g_2^m}{m!}\int_0^{\infty} J_0(v_{xy}\tau)\,e^{-\frac{m\tau^2}{T^2}}\tau d\tau \tag{4.30}$$

where $J_0(.)$ is the zeroth-order Bessel function of the first kind and $v_{xy}=\sqrt{v_x^2+v_y^2}$. Integral in (4.30) may be evaluated using

$$\int_0^{\infty} J_0(ax)\,e^{-p^2x^2}xdx = \frac{1}{2p^2}e^{-\frac{a^2}{4p^2}} \tag{4.31}$$

Hence, (4.30) may be written as

$$\operatorname{cov}(\rho,\rho') = \frac{\pi T^2FF'}{A}e^{-g_1}\sum_{m=1}^{\infty}\frac{g_2^m}{m!m}e^{-\frac{v_{xy}^2T^2}{4m}} \tag{4.32}$$

Substituting (4.23b) and (4.32) into (4.22), we find

$$E\left(\rho(\rho')^*\right) = e^{-g_1}\left[\rho_0\rho'_0 + \frac{\pi T^2 F F'}{A}\sum_{m=1}^{\infty}\frac{g_2^m}{m!m}e^{-\frac{v_{xy}^2 T^2}{4m}}\right] \tag{4.33}$$

In the special case when the two observation points coincide, (4.33) reduces to the autocorrelation equation,

$$E\left(\rho\rho^*\right) = e^{-g}\left[\rho_0^2 + \frac{\pi T^2 F^2}{A}\sum_{m=1}^{\infty}\frac{g^m}{m!m}e^{-\frac{v_{xy}^2 T^2}{4m}}\right] \tag{4.34}$$

Parameter g_2 is proportional to σ^2/λ^2 . Therefore, it can be used to divide surfaces into three broad categories, namely, slightly, moderately, and very rough surfaces. Slightly and moderately rough surfaces are handled using the physical optics (PO) model while geometric optics (GO) solution is used for very rough surfaces [68]. Next, for each of these categories, the series solution in (4.31) is examined.

Slightly rough surfaces have $g_2 \ll 1$, for which the series solution in (4.33) converges quickly and only the first term needs to be considered. Therefore,

$$E\left(\rho(\rho')^*\right) = e^{-g_1}\left[\rho_0\rho'_0 + \frac{\pi g_2 T^2 F F'}{A}e^{-\frac{v_{xy}^2 T^2}{4}}\right] \tag{4.35}$$

Surfaces for which $g_2 \approx 1$ are categorized as moderately rough. The series converges relatively slowly and several terms should be taken into consideration to obtain a solution. Surfaces for which $g_2 \gg 1$ are regarded as very rough. In this case, series

solution in (4.33) is of little use and we need to revisit the integral in (4.23a). Noting that for $g_2 \gg 1$, $\chi(v_z)\chi^*(v'_z) \approx 0$ and using (4.29), we find

$$\mathrm{cov}(\rho, \rho') = \frac{2\pi FF'}{A} e^{-g_1} \int_0^\infty J_0(v_{xy}\tau)\, e^{g_2 e^{-\tau^2/T^2}}\, \tau d\tau \tag{4.36}$$

Significant contributions to this integral only come from small τ where the argument of the exponential is small; Hence, the surface correlation function may be approximated by the first two terms of its series expansion, i.e., $\exp(-\tau^2/T^2) = 1-\tau^2/T^2$. Substituting in (4.36) and applying (4.31) leads to

$$\mathrm{cov}(\rho, \rho') = \frac{\pi T^2 FF'}{Ag_2} e^{g_2 - g_1 - \frac{v_{xy}^2 T^2}{4g_2}} \tag{4.37}$$

We find from (4.22), (4.23b), and (4.37)

$$E\left(\rho(\rho')^*\right) = e^{-g_1}\left[\rho_0 {\rho'}_0 + \frac{\pi T^2 FF'}{Ag_2} e^{g_2 - \frac{v_{xy}^2 T^2}{4g_2}}\right] \tag{4.38}$$

Under the GO limit, we modify (4.38) to incorporate the shadowing effects,

$$E\left(\rho(\rho')^*\right) = e^{-g_1}\left[\rho_0 {\rho'}_0 + \frac{\pi T^2 FF'S}{Ag_2} e^{g_2 - \frac{v_{xy}^2 T^2}{4g_2}}\right] \tag{4.39}$$

where $S = S(\theta_i, \theta_s)$ is the shadowing function in which $\theta_i = \theta_1$ is the incidence angle and $\theta_s \approx (\theta_2 + \theta'_2)/2$ is the scattering angle. A widely used shadowing function is

reported by Sancer [96] to modify the bistatic scattering coefficients,

$$S\left(\theta_i, \theta_s\right) = \left[1 + \Lambda\left(\gamma_i\right) + \Lambda\left(\gamma_s\right)\right]^{-1} \tag{4.40}$$

in which $\gamma_\alpha = (T \cot \theta_\alpha)/(2\sigma)$ and $\alpha = i, s$. For the Gaussian random rough surface,

$$\Lambda\left(\theta\right) = \frac{1}{2}\left[\frac{e^{-\gamma^2}}{\sqrt{\pi}\gamma} - \mathrm{erfc}(\gamma)\right] \tag{4.41}$$

erfc is the complementary error function.

4.4 Numerical results and discussion

A mmW outdoor urban link is considered in which the access points are mounted on the lampposts below the rooftops of the surrounding buildings. Buildings are assumed to form a continuum on both sides of the street. Here, we study the path loss, spatial correlation, coverage distance, and coherence length for LOS, OLOS, and NLOS situations, which are typical of an urban street with foliage and vehicular and pedestrian traffic.

Antenna arrays are simulated using directional horn antennas. Both vertically and horizontally polarized antennas are considered. The transmit array is either isotropic or directional with a directionality of 25 dBi and horizontal beamwidth of 10 degrees.

The receive array is either isotropic or directional with a directionality of 15 dBi and horizontal beamwidth of 40 degrees. Transmit and receive beams are assumed perfectly aligned. Concrete is assumed for the building exteriors with dielectric constant ε=4.17+0.36i, roughness height σ=0.2 mm, and surface correlation length T=38.6 mm [119]. Road dielectric is asphalt for which the dielectric constant is ε=3.18+0.1i, σ=0.34 mm is the roughness rms height, and surface correlation length is T=4.2 mm [66], [119]. Simulation frequencies are 30 GHz, 60 GHz, 94 GHz, 120 GHz, and 300 GHz. Unless otherwise stated, access point height is 5 m, UE height is 1.5 m, and the street width is 18 m. Access point is installed 4 m away from one side of the street while the UE is considered in the middle of the street.

To calculate the total received field at the observation point, the direct and reflected fields from ground and multiple bounces from walls up to the 20th order, and single scattering from ground and walls are included in the KA-based ray model. To implement the Kirchhoff scattering theory in a ray tracing algorithm, on each surface, 20×20 scattering tiles with equal side length of 10 times the surface correlation length are placed around the specular reflection point. Figure 4.5 represents the relative received power at different distances from the BS in an urban canyon. In the case of directional transceivers, the transmit array has a directionality of 25 dBi and horizontal beamwidth of 10 degrees. The receive array has a directionality of 15 dBi and horizontal beamwidth of 40 degrees. Antennas at both sides are vertically polarized. It is realized that higher directionality increases the received power and

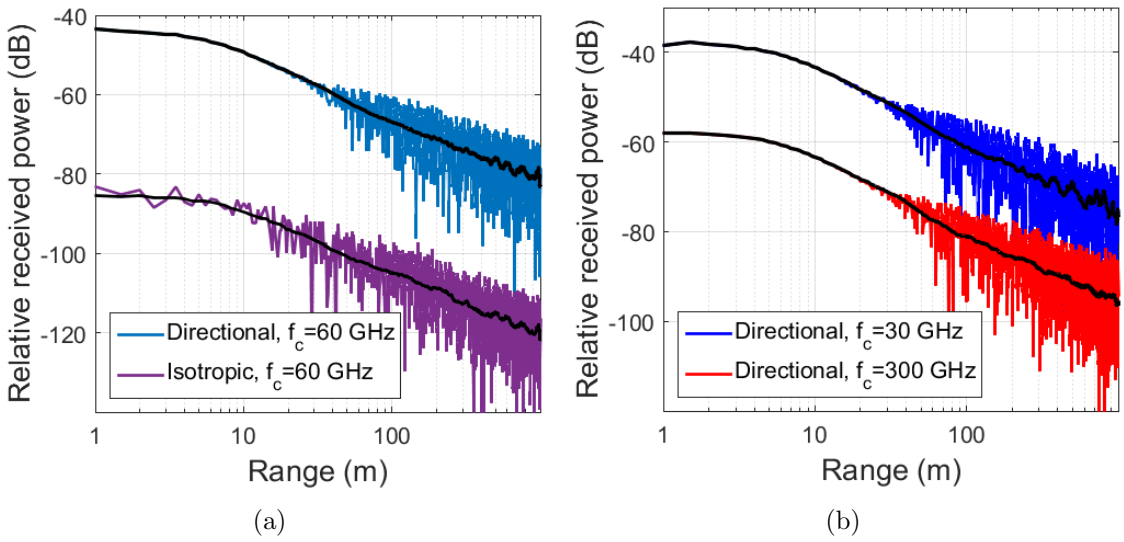

Figure 4.5: Path loss versus range: (a) directional antennas compared to isotropic radiators; (b) effect of increasing the carrier frequency 10 fold. Black lines present the local average of the received power.

reduces the shadow fading. This is because when directional antennas are used, most of the reflectors and scatterers will fall outside the antennas beamwidth. Moreover, it is noticed that increasing the carrier frequency by one order of magnitude decreases the received power by almost 2 orders of magnitude. It is also observed that the LOS median power falloff rate is roughly equivalent to free space wavefront spreading loss and, therefore, the total loss can be approximated by the free space loss. That is because at mmW frequencies, the first Fresnel zone radius is very small. In our simulations, the break distance, $d_B = 4h_t h_r/\lambda$ at which the first Fresnel zone touches the ground and the gradual transition from square law to fourth law begins, is several kilometers.

In order to find the dominant propagation mechanism in mmW links, we compared

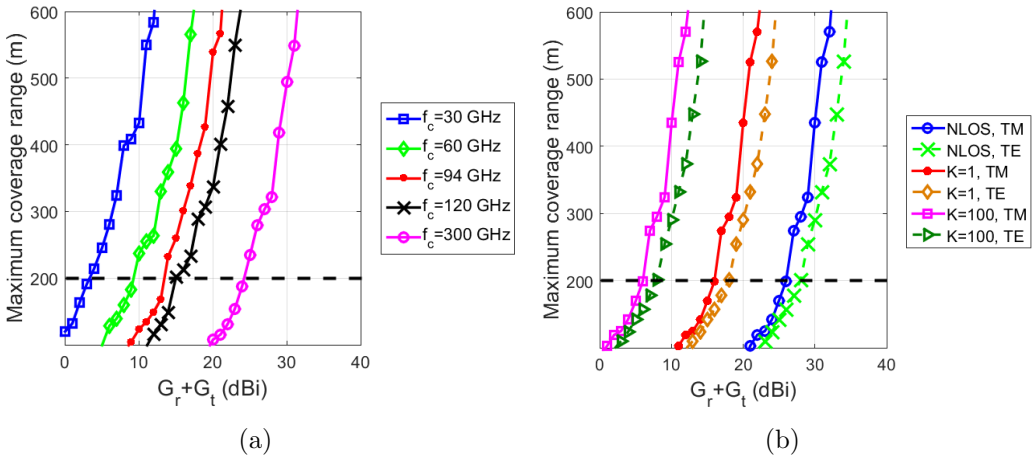

Figure 4.6: Coverage range versus combined antenna gains. (a) Coverage range at different mmW frequencies; (b) coverage range for various values of Rician K parameter.

the contribution of separate components throughout our simulations. It was deduced that for relatively short LOS links (in the order of 20 meters or less), only the direct wave needs to be considered. However, at larger distances, waveguiding effects due to multiple reflections also become important and cannot be overlooked. In fact, in NLOS links these multiple reflections dominate the propagation. Scattering effect is only notable in short NLOS links, especially when less directive antennas are used. As a function of distance, the scattered power decay rate is -40 dB/decade while the direct and reflected powers fall off at the rate of -20 dB/decade [103]. Moreover, at a longer range, the normal component of the wave vector falls, $k_z\sigma$ decreases, and the surface appears electrically smoother. Shadowing effect, however, is always negligible in our simulations. Shadowing is prominent when the mean square surface slope is high and/or the beam approaches the grazing angle. It is intuitive to compare the

propagation features in mmW small cells to those of microwave macrocells based on the Walfisch-Ikegami model [120]. In this model, the buildings in the vertical plane between the Tx and Rx are taken into account and the waveguiding effects are ignored. This is because in urban macrocells, base stations are usually mounted above the rooftop levels and multiple diffractions over the rooftops dominate the propagation. On the other hand, in mmW small cells due to below-rooftop deployment, waveguiding effects are pronounced but diffraction around obstacles is low.

Figure 4.6(a) represents the effect of antenna directivity on coverage distance. A moderate value of 100 dB is selected as the maximum path loss dynamic range [36]. By assuming a low measurable path loss range, we are effectively accounting for the signal attenuation due to random blocking objects such as foliage, cars and people which, on average, will not exceed 20 dB in such short links [121]. Typical coverage distance recommended for mmW small cells is in the order of 200 m, which is also indicated on the plots. It is noted that even at 300 GHz this range is achievable by a combined antenna gain of 25 dBi, which can easily be realized at one side of the link, typically the BS.

The scenario of OLOS or NLOS is considered in Figure 4.6 (b) using the Ricean factor, K. At 60 GHz, it is noticed that the desired range is readily achievable via moderately directive antenna arrays. It is also concluded that vertically polarized antennas attain a larger coverage distance. Here, depolarization effects are not examined; but mmW

measurements in [122] show a cross-polar discrimination (XPD) of at least 10 dB. Thus, based upon the realizable coverage range and XPD in mmW small cells, two stream multiplexing over orthogonal polarizations is readily practicable.

To analyze intra-user and co-located inter-user spatial correlation versus inter-element spacing, a simple scenario is considered in which a BS is simultaneously transmitting to receive antenna 1 and receive antenna 2. In these simulations, baseline parameters are as follows, unless indicated otherwise: f_c=60 GHz, nodes distance is d=50 m, and antennas are vertically polarized. For directional links, the Tx directionality is 25 dBi while that of the Rx is 15 dBi. Correlations at the AP and UE sides were found to follow similar trends; thus, only the results at the UE side are represented. Here, the BS height and distance from the reference side of the street are fixed at 5m and 4 m, respectively. Height of the Rx antenna pair is uniformly distributed over the interval [1m, 3m] and the distance of the pair from the walls at each side of the street is uniformly selected over [4m, 14 m]. 10000 realizations of the canonical randomized geometry are used to compile the correlation statistics for two cases of isotropic and directional antennas. Spatial correlation in azimuth (the horizontal plane) is studied in Figure 4.7. Isotropic transceivers experience richer scattering, thus, the correlation is generally lower when isotropic antennas are used. It is also observed that higher carrier frequencies lead to lower correlations at the same element spacing, as expected. At larger distances, angular spread of the incoming energy decreases, which

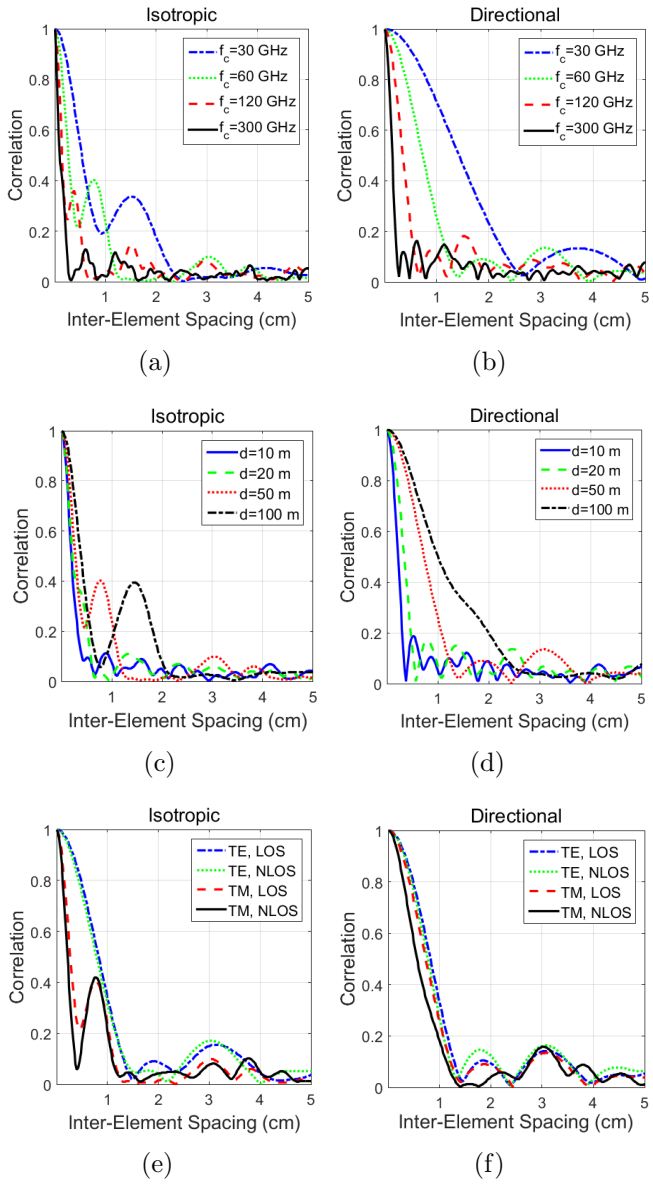

Figure 4.7: Azimuth correlation versus inter-element spacing. (a,b) correlation at different frequencies; (c,d) correlation at different ranges; (e,f) correlation for different antenna polarizations in the presence and absence of a LOS component.

is inversely proportional to the correlation. Therefore, in an urban canyon, correlation coefficients increase with Tx-Rx distance. Moreover, it is observed that vertical polarization leads to better signal decorrelation. Another interesting point is that

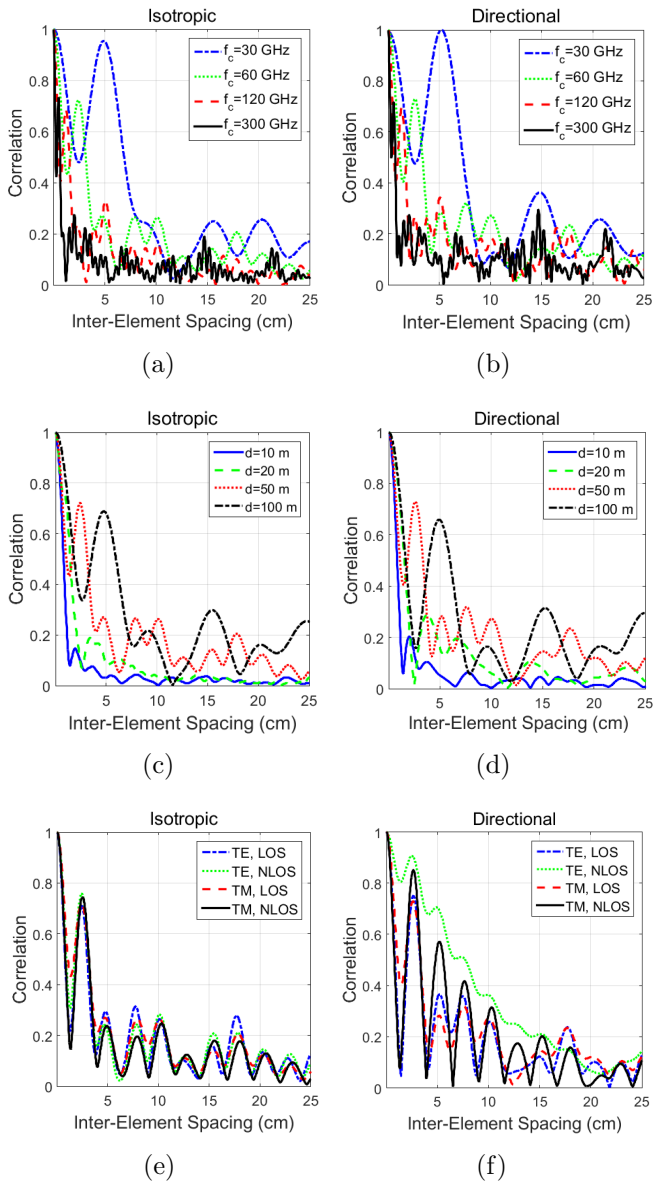

Figure 4.8: Elevation correlation versus inter-element spacing. (a,b) correlation at different frequencies; (c,d) correlation at different ranges; (e,f) correlation for different antenna polarizations in the presence and absence of a LOS component.

LOS component correlates the received signals that in turn increases the correlation coefficients. Figure 4.8 depicts the spatial correlation in elevation (the vertical plane). Compared to the latter simulation, the only difference is that the Rx antenna pair is

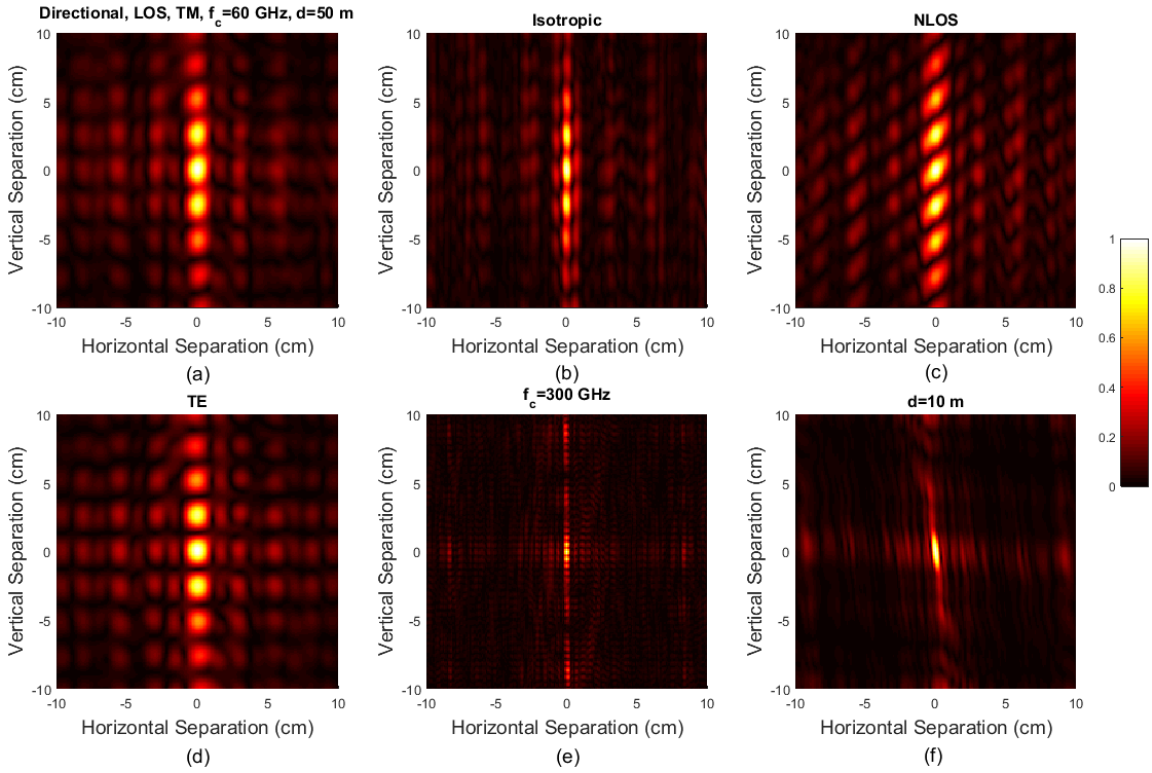

Figure 4.9: 2D array correlation versus inter-element spacing. Reference plot: Directional, LOS, TM, f_c=60 GHz, d=50 m; (b) Isotropic antennas; (c) NLOS scenario; (d) TE polarization; (e) frequency increased to 300 GHz; (f) Range decreased to 10 m.

vertical. The elevation spatial correlation follows exactly the same trends; however, the coherence length is much longer in the vertical plane. Hence, in planar 2D arrays, the horizontal dimension is well-suited for spatial multiplexing to generate degrees of freedom to transmit parallel data streams and improve the spectral efficiency. The vertical dimension, on the other hand, is better exploited for beamforming gain to amplify the signal power and alleviate the interference. To examine the 2D intra-user spatial correlation, a 20 cm×20 cm planar 2D array is considered. Receive antenna 1 is placed at the center of the array while receive antenna 2 is moved in 1 mm steps on a square grid laid on the array. The baseline parameters are similar to linear array

simulations. Figure 4.9(a) serves as our reference result and in each of the subsequent plots, only one of the reference parameters are altered to study the impact of that particular parameter. Due to location of the lampposts and users, simulation geometry is unsymmetrical; thus, the correlation values are also unsymmetrical. This is more pronounced in shorter links. Some interesting observations are: a) beamforming increases the correlation and the coherence length, which manifests itself better in the azimuth dimension (comparing Figure 4.9(a) and Figure 4.9(b)); b) in relatively short links, the direct wave dominates the correlation value, while in longer links the waveguiding effects do; since multiple reflections amplitude are comparable with the direct component amplitude at longer distances. That is why at relatively long simulation distance of d=50 m, eliminating the direct component only modestly alters the correlation; c) horizontally polarized antennas (compared to vertically polarized ones) increase the correlation in horizontal dimension and slightly decrease the correlation in vertical dimension; d) when the carrier frequency increases, correlation declines steeply; e) correlation increases with distance; this is because the angular spread of the incoming energy decreases at longer ranges. Azimuth spread is wider than elevation spread that leads to shorter coherence length in horizontal dimension. It also reduces faster with distance compared to the elevation spread. To achieve

higher rank gain matrices in multi-antenna systems, antenna spacing should exceed the coherence length. Typical coherence length values for range and frequencies of interest in mmW small cells are presented in Table 4.1. Directivity is 25 dBi at the BS

Table 4.1
Coherence length (mm) versus antennas directivity and range

f (GHz)	Transceiver Antenna Directivity											
	Isotropic-Isotropic				Directional-Isotropic				Directional-Directional			
	TE		TM		TE		TM		TE		TM	
	Az	El	Az	El	Az	El	Az	El	Az	El	Az	El
30	15.50	65.25	5.50	68.75	16.00	70.25	14.00	73.00	16.00	70.50	14.50	73.00
94	5.25	19.50	2.00	20.75	5.25	21.75	4.50	22.25	5.25	21.75	4.75	22.25
300	1.75	6.25	1.00	6.50	1.75	6.75	1.50	6.75	1.75	6.75	1.50	6.75

f (GHz)	Receiver-Transmitter Distance											
	20 m				50 m				100 m			
	TE		TM		TE		TM		TE		TM	
	Az	El	Az	El	Az	El	Az	El	Az	El	Az	El
30	7.00	30.00	7.00	30.50	16.00	70.50	14.50	73.00	28.00	126.00	20.25	128.25
94	2.25	9.75	2.25	9.75	5.25	21.75	4.75	22.25	9.50	39.00	6.75	39.50
300	0.75	3.25	0.75	3.25	1.75	6.75	1.50	6.75	3.00	12.50	2.25	12.75

Simulation parameters: LOS, h_t=5 m, h_r=1.5 m, (upper) d=50 m, (lower) directional at both ends; step size is 0.25 mm.

side and 15 dBi at the UE side. Coherence length is directly related to the antenna directionality and link range, and inversely related to the carrier frequency.

4.5 Conclusion

This chapter proposes an approach to investigate the path loss, spatial correlation, coverage distance, and coherence length in multiuser wireless communication systems for promising mmW frequency ranges. Closed form expressions for multiuser correlation of co-located receive antennas are derived theoretically and numerically evaluated for an urban environment under a range of variations in the propagation geometry.

We concluded that scattering effects must be taken into account in any mmW channel model because, especially in NLOS conditions, the diffuse power is significant at higher frequencies and lower transceiver distances, which are typical attributes of mmW small cells. Overall, it is realized that the assumption of favorable propagation for mmW massive MIMO is perfectly valid and both access points and user terminals can enjoy the advantages of MIMO via beamforming and spatial multiplexing. We observed that the target coverage range of 200 meters is easily achievable using directional antennas at the BS and user terminals. Even if only the BS is equipped with directional antennas, the target range is achievable throughout the mmW frequency range. Possible future work include studying the effect of multiscale roughness and incorporating stochastic models to account for blockage effects.

Chapter 5

Conclusion and Future Work

5.1 Conclusion

A computationally feasible near-ground field prediction model is presented in chapter 2 to facilitate more accurate WSN simulations. The model is validated against published measured data in open areas. Model precision is due to careful assessment of the impact of first Fresnel zone obstruction, terrain irregularities, and dielectric properties of the ground on the LOS, specular reflection and higher order waves. The proposed model is also used to evaluate the effects of radio link and terrain parameters on network connectivity of WSNs. Some practical implications of this study include: (a) the critical distance is very small in WSN applications and, therefore,

the diffraction loss is integral to WSN channel characterization; (b) at grazing angles, Fresnel reflection coefficient displays a very low sensitivity to terrain dielectric constant; (c) provided the geometrical parameters are fixed, higher order waves intensify as the wavelength increases; (d) antenna height is by far the most influential geometrical parameter to network connectivity; (e) connectivity is fairly sensitive to the reflection coefficient when antennas are placed near the ground; (f) terrain roughness decreases the accessible neighbors; (g) lowering the frequency of operation, enhances the network connectivity; (h) close to the ground level, vertically polarized antennas outperform their horizontally polarized counterparts in terms of coverage range and connectivity; (i) precipitation boosts/reduces the network connectivity when motes are equipped with vertically/horizontally polarized antennas.

In chapter 3, small perturbation method (SPM) and Kirchhoff approximation (KA) are incorporated into ray-tracing (RT) routines to model multiuser multi-input multi-output (MU-MIMO) channels formed on a rough dielectric terrain. The effect of surface roughness and correlation length, solid soil fractions, moisture content, link range, antenna height, polarization, radiation pattern, and carrier frequency are examined on received power, power delay and angular profiles, root mean square (RMS) delay and angular spread, coherence bandwidth, and coherence distance. Quantitative and qualitative analyses reveal that antenna directionality and terrain undulation and textural composition have significant impacts on the received signal power and channel multipath parameters and, hence, the performance of MU-MIMO terrain-based

communication systems. The main conclusions of this study follows: (a) Higher surface roughness height leads to lower relative received power and lower spatial correlation between the elements of the antenna array; (b) increasing the receiving elements distance reduces the spatial correlation between them; (c) higher surface RMS height increases the incoherent part of the scattered field and decreases the coherent component; (d) angular spread of the incoming waves increases as the surface roughness height increases; (e) increasing the transmitter and receiver array distance decreases the received power and the spatial correlation; (f) as the height of transmitter and/or receiver increases, effect of the surface roughness on the received power and spatial correlation decreases; (g) increasing the undulation heights has a noticeable impact on increasing the RMS delay spread and correspondingly increasing the channel frequency selectivity; (h) increasing the correlation length, decreases the scattered power; (i) channel bandwidth has a higher sensitivity to variation of surface roughness height rather than variation of surface correlation distance; (j) LOS signal reduces the frequency selectivity of the channel and leads to higher coherence bandwidth.

This study highlights the significance of diffuse scattering in MIMO communication channels with applications in wireless sensor networks for environmental monitoring and near ground communication between transceivers working above a dielectric rough terrain, and body surface to external device channel modeling.

Chapter 4 proposes an approach to investigate the spatial correlation and coverage distance in massive MIMO communication systems for mmW frequency ranges. Closed form expressions for multiuser correlation of co-located receive antennas are derived theoretically and numerically evaluated for an urban environment under a range of variations in the propagation geometry. We found that scattering effects must be taken into account in any mmW channel model because, especially in NLOS conditions, the diffuse power is significant at higher frequencies and lower transceiver distances which are typical attributes of mmW small cells. It is observed that for the lamppost based implementation of the mmW small cell, a moderate antenna separation is sufficient to offer spatial diversity. We observed that the target coverage range of 200 meters is easily achievable using directional antennas at the base station and user terminal. Even if only the base station is equipped with directional antennas, the target range is achievable throughout the mmW frequency range.

5.2 Future work

5.2.1 Channel modeling for wireless sensor networks in layered media with rough boundaries

Layered structures with rough boundaries represent many naturally occurring structures. Electromagnetic (EM) scattering from layered structures with rough boundaries have key applications in environmental monitoring, geology and soil mechanics, hydrology, oil and gas exploration, civil engineering, detection of improvised explosive devices (IED), planetary explorations, and medical imaging [123], [140]. However, very limited modeling and measurements have been carried out on links working inside or above multi-layered dielectric structures with rough boundaries such as layered soil, rivers, lakes, and multi-year ice.

Another key set of problems falling into this group is the deployment and optimization of Underground WSN. WUSN is a promising technology which enables a wide variety of new applications that include monitoring of underground soil conditions such as water and mineral content for intelligent irrigation and fertilization, underground infrastructure monitoring such as electrical wiring, pipes and liquid storage tanks, and border patrol and security monitoring using sensors to detect the presence of a

person or an object [141], [143]. WUSN have many advantages over the conventional wired sensor networks such as reliability, ease of deployment, and concealment[142].

Underground wireless channel are hostile mediums for wireless communications. Here, EM waves suffer much higher loss compared to air, which complicates their characterization. Indeed, a comprehensive channel model for such an environment does not exist. WUSN deployed near the surface of the ground are able to communicate with both under and above ground nodes so that a communication link exists partially in the air and partially in the soil. Therefore, investigation of the impacts of ground inhomogeneity on the communication channel operating in low altitude or subsurface is crucial.

5.2.2 Channel modeling for WSN in inhomogeneous media with volumetric stratification

Even though there are several models for path attenuation in forested environments from HF to millimeter-waves range, the spatial, temporal, and spectral characterization of these channels are an under-explored area. WSN deployed in foliage environment experience multipath fading due to scattering, diffraction, energy absorption and shadowing caused by tree trunks and leaves. Moreover, WUSN deployed in such environments suffer scattering resulting from vegetation roots, which have distinct

dielectric properties from the soil. Sensor motes in these systems do not have any information about the power, delay and direction of arrival of each individual path and instead require the aggregate descriptions of the propagation environment including the received power, power delay spread and power angular spread. Due to the presence of scatterers in the environment, multipath propagation is inherent in realistic radio channels. The multipath not only decorrelates the signal outputs at various antennas, but also induces delay spread, which results in frequency-selective fading. Delay spread determines the maximum distortion-free data rates that can be transmitted via a wireless channel. Another critical parameter that is inversely proportional to delay spread is called the coherence bandwidth which quantifies the frequency variations of the channel [1]. Similarly, different angles of departure (AoD) and angles of arrival (AoA) in a multipath environment lead to power angular spread, which determines the coherence distance. In general, wider angular spread and larger spacing between the array elements entail less spatial correlation and vice versa. Coherence distance establishes the minimum antenna spacing required to achieve uncorrelated channel responses. Therefore, effects of additional parameters such as delay spread and angular spread are necessary to accurately describe the wireless channel.

Another important media that belongs to this category is human body. Body area links can be grouped into several classes based on the location of the communicators with respect to the body, namely, implant, on body, and external. Scenarios in which one or both sides of the link are implants are not easily amenable to experimental

measurements [144]. In these scenarios, full-wave simulation tools should be developed to study the propagation environment. However, it is possible to make measurements using communicating nodes to develop empirical models when the transceivers are all on the surface or external to the body. Both theoretical and empirical models will be developed to study path attenuation, shadowing statistics, power delay and angular profiles, RMS delay and angular spread, coherence bandwidth, and coherence distance which will facilitate the design of optimal body area communication systems and the development of body-aware localization algorithms.

References

[1] R. Janaswamy, Radiowave propagation and smart antennas for wireless communications: Springer Science & Business Media, 2001.

[2] S. A. Zekavat and C. R. Nassar, "Achieving high-capacity wireless by merging multicarrier CDMA systems and oscillating-beam smart antenna arrays," IEEE Transactions on Vehicular Technology, vol. 52, pp. 772-778, 2003.

[3] W. Xu, "Multi-antenna non-line-of-sight identification techniques for target localization in mobile ad-hoc networks," 2011.

[4] Y. Su Khiong and J. S. Thompson, "Three-dimensional spatial fading correlation models for compact MIMO receivers," IEEE Transactions on Wireless Communications, vol. 4, pp. 2856-2869, 2005.

[5] X. Cheng, C. X. Wang, H. Wang, X. Gao, X. H. You, D. Yuan, et al., "Cooperative MIMO Channel Modeling and Multi-Link Spatial Correlation Properties," IEEE Journal on Selected Areas in Communications, vol. 30, pp. 388-396, 2012.

[6] L. Wei and J. Ya-Qiu, "A model of MIMO system over a three-dimensional rough surface," in Antennas Propagation and EM Theory (ISAPE), 2010 9th International Symposium on, 2010, pp. 714-717.

[7] X. Wenjie, S. A. Zekavat, and T. Hui, "A Novel Spatially Correlated Multiuser MIMO Channel Modeling: Impact of Surface Roughness," Antennas and Propagation, IEEE Transactions on, vol. 57, pp. 2429-2438, 2009.

[8] M. K. Ozdemir, H. Arslan, and E. Arvas, "On the correlation analysis of antennas in adaptive MIMO systems with 3-D multipath scattering," in Wireless Communications and Networking Conference, 2004. WCNC. 2004 IEEE, 2004, pp. 295-299 Vol.1.

[9] J. S. K. Raj, A. S. Prabu, N. Vikram, and J. Schoebel, "Spatial Correlation and MIMO Capacity of Uniform Rectangular Dipole Arrays," IEEE Antennas and Wireless Propagation Letters, vol. 7, pp. 97-100, 2008.

[10] J.-H. Lee and C.-C. Cheng, "The spatial correlation characteristics of 3-D antenna array systems," in 2011 IEEE 54th International Midwest Symposium on Circuits and Systems (MWSCAS), 2011.

[11] B. S, x00Fc, x00Fc, x00E, orak, and G. K. Kurt, "Simulation and measurement of spatial correlation in MIMO systems with ray tracing," in Signal Processing and Communication Systems (ICSPCS), 2011 5th International Conference on, 2011, pp. 1-5.

[12] P. Chul-Keun and M. Kyeong-Sik, "A study on spatial correlation characteristic of array antenna for multi antenna system," in Microwave Conference Proceedings, 2005. APMC 2005. Asia-Pacific Conference Proceedings, 2005, p. 4 pp.

[13] C. Sturm, M. Porebska, G. Adamiuk, and W. Wiesbeck, "Simulation and Measurement Based Correlation Estimation for Ultra Wideband Antenna Arrays," in Antennas, 2007. INICA '07. 2nd International ITG Conference on, 2007, pp. 110-114.

[14] R. Zekavat and R. M. Buehrer, Handbook of position location: Theory, practice and advances vol. 27: John Wiley & Sons, 2011.

[15] P. Hui, C. G. Hynes, J. V. Wonterghem, and D. G. Michelson, "3D autocorrelation coefficients of dipole antenna," Electronics Letters, vol. 42, pp. 257-258, 2006.

[16] W. F. Tsen and H. J. Li, "Spatial correlation of half-wavelength dipole arrays using spherical mode expansion," in Personal, Indoor and Mobile Radio Communications, 2009 IEEE 20th International Symposium on, 2009, pp. 1074-1077.

[17] P. C. Hsieh and F. C. Chen, "A New Spatial Correlation Formulation of Arbitrary AoA Scenarios," IEEE Antennas and Wireless Propagation Letters, vol. 8, pp. 398-401, 2009.

[18] C. Jansen, S. Priebe, C. Moller, M. Jacob, H. Dierke, M. Koch, et al., "Diffuse

Scattering From Rough Surfaces in THz Communication Channels," Terahertz Science and Technology, IEEE Transactions on, vol. 1, pp. 462-472, 2011.

[19] P. Beckmann and A. Spizzichino, "The scattering of electromagnetic waves from rough surfaces," Norwood, MA, Artech House, Inc., 1987, 511 p., 1987.

[20] L. Tsang and J. A. Kong, Scattering of Electromagnetic Waves, Advanced Topics vol. 26: John Wiley & Sons, 2004.

[21] A. Ishimaru, Wave propagation and scattering in random media vol. 2: Academic press New York, 1978.

[22] S. A. Tabatabaeenejad, "Forward and inverse models of electromagnetic scattering from layered media with rough interfaces," UNIVERSITY OF MICHIGAN, 2008.

[23] S. Priebe, M. Jacob, C. Jansen, K. T, x00Fc, and rner, "Non-specular scattering modeling for THz propagation simulations," in Antennas and Propagation (EUCAP), Proceedings of the 5th European Conference on, 2011, pp. 1-5.

[24] D. Didascalou, M. Dottling, N. Geng, and W. Wiesbeck, "An approach to include stochastic rough surface scattering into deterministic ray-optical wave propagation modeling," IEEE Transactions on Antennas and Propagation, vol. 51, pp. 1508-1515, 2003.

[25] T. M. Elfouhaily and C.-A. Gurin, "A critical survey of approximate scattering wave theories from random rough surfaces," Waves in Random Media, vol. 14, pp. R1-R40, 2004/10/01 2004.

[26] A. G. Voronovich, Wave scattering from rough surfaces vol. 17: Springer Science & Business Media, 2013.

[27] R. Piesiewicz, C. Jansen, D. Mittleman, T. Kleine-Ostmann, M. Koch, and T. Krner, "Scattering analysis for the modeling of THz communication systems," Antennas and Propagation, IEEE Transactions on, vol. 55, pp. 3002-3009, 2007.

[28] J. A. Ogilvy and J. Ogilvy, Theory of wave scattering from random rough surfaces: Hilger Bristol et al., 1991.

[29] M. A. Demir, "PERTURBATION THEORY OF ELECTROMAGNETIC SCATTERING FROM LAYERED MEDIA WITH ROUGH INTERFACES," The Ohio State University, 2007.

[30] I. F. Akyildiz, W. Su, Y. Sankarasubramaniam, and E. Cayirci, "Wireless sensor networks: a survey," Computer Networks, vol. 38, pp. 393-422, 2002.

[31] A. Martinez-Sala, J.-M. Molina-Garcia-Pardo, E. Egea-Ldpez, J. Vales-Alonso, L. Juan-Llacer, and J. Garcia-Haro, "An accurate radio channel model for wireless sensor networks simulation," Communications and Networks, Journal of, vol. 7, pp. 401-407, 2005.

[32] G. G. Joshi, C. B. Dietrich, C. R. Anderson, W. G. Newhall, W. A. Davis, J. Isaacs, et al., "Near-ground channel measurements over line-of-sight and forested paths," Microwaves, Antennas and Propagation, IEE Proceedings, pp. 589-596, 2005.

[33] Y. S. Meng, Y. H. Lee, and B. C. Ng, "Path loss modeling for near-ground vhf radio-wave propagation through forests with tree-canopy reflection effect," Progress In Electromagnetics Research M, vol. 12, pp. 131-141, 2010.

[34] M. Yu Song, L. Yee Hui, and N. Boon Chong, "Empirical Near Ground Path Loss Modeling in a Forest at VHF and UHF Bands," Antennas and Propagation, IEEE Transactions on, vol. 57, pp. 1461-1468, 2009.

[35] J. G. Andrews, S. Buzzi, C. Wan, S. V. Hanly, A. Lozano, A. C. K. Soong, et al., "What Will 5G Be?," Selected Areas in Communications, IEEE Journal on, vol. 32, pp. 1065-1082, 2014.

[36] T. S. Rappaport, S. Shu, R. Mayzus, Z. Hang, Y. Azar, K. Wang, et al., "Millimeter Wave Mobile Communications for 5G Cellular: It Will Work!," Access, IEEE, vol. 1, pp. 335-349, 2013.

[37] M. R. Akdeniz, L. Yuanpeng, S. Rangan, and E. Erkip, "Millimeter wave picocellular system evaluation for urban deployments," in Globecom Workshops (GC Wkshps), 2013 IEEE, 2013, pp. 105-110.

[38] A. Al-Rasheed and S. A. Zekavat, "Rough surface impact on spatial correlation: 30, 60 and 300 GHz," in Global Communications Conference (GLOBECOM), 2013 IEEE, 2013, pp. 3965-3970.

[39] I. F. Akyildiz, S. Weilian, Y. Sankarasubramaniam, and E. Cayirci, "A survey on sensor networks," Communications Magazine, IEEE, vol. 40, pp. 102-114, 2002.

[40] F. P. Fontn and P. M. Espieira, Modelling the wireless propagation channel: a simulation approach with MATLAB vol. 5: John Wiley & Sons, 2008.

[41] M. Rodriguez, R. Feick, H. Carrasco, R. Valenzuela, M. Derpich, and L. Ahumada, "Wireless Access Channels with Near-Ground Level Antennas," Wireless Communications, IEEE Transactions on, vol. 11, pp. 2204-2211, 2012.

[42] G. G. Joshi, C. B. Dietrich, C. R. Anderson, W. G. Newhall, W. A. Davis, J. Isaacs, et al., "Near-ground channel measurements over line-of-sight and forested paths," Microwaves, Antennas and Propagation, IEE Proceedings, vol. 152, pp. 589-596, 2005.

[43] J. R. Hampton, N. M. Merheb, W. L. Lain, D. E. Paunil, R. M. Shuford, and W. Kasch, "Urban propagation measurements for ground based communication in the military UHF band," Antennas and Propagation, IEEE Transactions on, vol. 54, pp. 644-654, 2006.

[44] L. DaHan and K. Sarabandi, "Terminal-to-Terminal Hybrid Full-Wave Simulation of Low-Profile, Electrically-Small, Near-Ground Antennas," Antennas and Propagation, IEEE Transactions on, vol. 56, pp. 806-814, 2008.

[45] L. DaHan and K. Sarabandi, "Simulation of Near-Ground Long-Distance Radiowave Propagation Over Terrain Using Nystrom Method With Phase Extraction Technique and FMM-Acceleration," Antennas and Propagation, IEEE Transactions on, vol. 57, pp. 3882-3890, 2009.

[46] M. I. Aslam and S. A. Zekavat, "New channel path loss model for near-ground antenna sensor networks," Wireless Sensor Systems, IET, vol. 2, pp. 103-107, 2012.

[47] R. A. Foran, T. B. Welch, and M. J. Walker, "Very near ground radio frequency propagation measurements and analysis for military applications," in Military Communications Conference Proceedings, 1999. MILCOM 1999. IEEE, 1999, pp. 336-340 vol.1.

[48] L. DaHan and K. Sarabandi, "Near-Earth wave propagation characteristics of electric dipole in presence of vegetation or snow layer," Antennas and Propagation, IEEE Transactions on, vol. 53, pp. 3747-3756, 2005.

[49] S. A. R. Zekavat, "Channel Modeling and Its Impact on Localization," Handbook of Position Location: Theory, Practice, and Advances, pp. 105-135.

[50] T. S. Rappaport, Wireless communications: principles and practice vol. 2: Prentice Hall PTR New Jersey, 1996.

[51] A. Goldsmith, Wireless communications: Cambridge university press, 2005.

[52] W. S. Ament, "Toward a Theory of Reflection by a Rough Surface," Proceedings of the IRE, vol. 41, pp. 142-146, 1953.

[53] L. Boithias and L.-J. Libols, Radio wave propagation: North Oxford acad. London, 1987.

[54] F. T. Dagefu and K. Sarabandi, "Analysis and Modeling of Near-Ground Wave Propagation in the Presence of Building Walls," Antennas and Propagation, IEEE Transactions on, vol. 59, pp. 2368-2378, 2011.

[55] K. Sarabandi and C. Tsenchieh, "Electromagnetic scattering from slightly rough surfaces with inhomogeneous dielectric profiles," Antennas and Propagation, IEEE Transactions on, vol. 45, pp. 1419-1430, 1997.

[56] L. DaHan and K. Sarabandi, "On the Effective Low-Grazing Reflection Coefficient of Random Terrain Roughness for Modeling Near-Earth Radiowave Propagation," Antennas and Propagation, IEEE Transactions on, vol. 58, pp. 1315-1324, 2010.

[57] M. J. Feuerstein, K. L. Blackard, T. S. Rappaport, S. Y. Seidel, and H. Xia, "Path loss, delay spread, and outage models as functions of antenna height for

microcellular system design," Vehicular Technology, IEEE Transactions on, vol. 43, pp. 487-498, 1994.

[58] A. Torabi, S. A. Zekavat, and K. Sarabandi, "Wideband Wireless Channel Characterization for Multi-Antenna Systems over a Random Rough Dielectric Ground," submitted to Wireless Communications, IEEE Transactions on.

[59] J. T. Johnson, "Computer simulations of rough surface scattering," in Light Scattering and Nanoscale Surface Roughness, ed: Springer, 2007, pp. 181-210.

[60] M. A. Weissberger, "An initial critical summary of models for predicting the attenuation of radio waves by trees," DTIC Document1982.

[61] COST 235, Radio propagation effects on next-generation fixed-service terrestrial telecommunication systems, Luxembourg, 1996, Final Rep.

[62] CCIR, "Influences of terrain irregularities and vegetation on troposphere propagation," Geneva, 1986, pp. 235236, CCIR Rep.

[63] M. O. Al-Nuaimi and R. B. L. Stephens, "Measurements and prediction model optimisation for signal attenuation in vegetation media at centimetre wave frequencies," Microwaves, Antennas and Propagation, IEE Proceedings, vol. 145, pp. 201-206, 1998.

[64] M. Rahman, M. Moran, D. Thoma, R. Bryant, E. Sano, C. Holifield Collins, et al., "A derivation of roughness correlation length for parameterizing radar

backscatter models," International Journal of Remote Sensing, vol. 28, pp. 3995-4012, 2007.

[65] J. Shang, J. Umana, F. Bartlett, and J. Rossiter, "Measurement of complex permittivity of asphalt pavement materials," Journal of transportation engineering, vol. 125, pp. 347-356, 1999.

[66] K. Sarabandi, E. S. Li, and A. Nashashibi, "Modeling and measurements of scattering from road surfaces at millimeter-wave frequencies," Antennas and Propagation, IEEE Transactions on, vol. 45, pp. 1679-1688, 1997.

[67] Mica2 MOTES,http://www.moog-crossbow.com.

[68] F. T. Ulaby, D. G. Long, W. J. Blackwell, C. Elachi, A. K. Fung, C. Ruf, et al., Microwave Radar and Radiometric Remote Sensing: University of Michigan Press, 2014.

[69] N. R. Peplinski, F. T. Ulaby, and M. C. Dobson, "Dielectric properties of soils in the 0.3-1.3-GHz range," Geoscience and Remote Sensing, IEEE Transactions on, vol. 33, pp. 803-807, 1995.

[70] N. R. Peplinski, F. T. Ulaby, and M. C. Dobson, "Corrections to "Dielectric Properties of Soils in the 0.3-1.3-GHz Range"," Geoscience and Remote Sensing, IEEE Transactions on, vol. 33, p. 1340, 1995.

[71] L. Pu, H. Zhang, J. Oostveen, and E. Fledderus, "MIMO-OFDM performance in relation to wideband channel properties," in Personal Indoor and Mobile Radio Communications (PIMRC), 2010 IEEE 21st International Symposium on, 2010, pp. 2381-2386.

[72] C. Leo and L. Sergey, "Impact of multipath angular distribution on performance of MIMO systems," in Electrical and Computer Engineering, 2004. Canadian Conference on, 2004, pp. 853-857 Vol.2.

[73] M. R. J. A. E. Kwakkernaat and M. H. A. J. Herben, "Angular dispersion of radio waves due to rough surface scattering in mobile channels," in Antennas and Propagation (EuCAP), 2010 Proceedings of the Fourth European Conference on, 2010, pp. 1-5.

[74] H. Bolcskei, M. Borgmann, and A. J. Paulraj, "Impact of the propagation environment on the performance of space-frequency coded MIMO-OFDM," IEEE Journal on Selected Areas in Communications, vol. 21, pp. 427-439, 2003.

[75] H. Sampath, S. Talwar, J. Tellado, V. Erceg, and A. Paulraj, "A fourth-generation MIMO-OFDM broadband wireless system: design, performance, and field trial results," IEEE Communications Magazine, vol. 40, pp. 143-149, 2002.

[76] J. G. Andrews, S. Buzzi, W. Choi, S. V. Hanly, A. Lozano, A. C. K. Soong, et al., "What Will 5G Be?," IEEE Journal on Selected Areas in Communications, vol. 32, pp. 1065-1082, 2014.

[77] K. Zhou and Y. H. Chew, "On the Achievable Diversity Gain by the Optimal Subcarrier Allocations in Multiuser OFDM System," in Military Communications Conference, 2006. MILCOM 2006. IEEE, 2006, pp. 1-6.

[78] P. Svedman, S. K. Wilson, L. J. Cimini, and B. Ottersten, "A simplified opportunistic feedback and scheduling scheme for OFDM," in Vehicular Technology Conference, 2004. VTC 2004-Spring. 2004 IEEE 59th, 2004, pp. 1878-1882 Vol.4.

[79] H. Yang and M. Herben, "Spatial dispersion and performance evaluation of indoor MIMO channels at 2.25 GHz," in Proceedings of the 11th IEEE Symposium on Communications and Vehicular Technology in the Benelux, 2004.

[80] S. Da-Shan, G. J. Foschini, M. J. Gans, and J. M. Kahn, "Fading correlation and its effect on the capacity of multielement antenna systems," IEEE Transactions on Communications, vol. 48, pp. 502-513, 2000.

[81] H. Zhang, O. Mantel, M. Kwakkernaat, and M. Herben, "Analysis of wideband radio channel properties for planning of next-generation wireless networks," in Antennas and Propagation, 2009. EuCAP 2009. 3rd European Conference on, 2009, pp. 3259-3263.

[82] A. Torabi, S. A. Zekavat, and A. Al - Rasheed, "Millimeter wave directional channel modeling," in Wireless for Space and Extreme Environments (WiSEE), 2015 IEEE International Conference on, 2015, pp. 1-6.

[83] I. Hwang, B. Song, and S. S. Soliman, "A holistic view on hyper-dense heterogeneous and small cell networks," IEEE Communications Magazine, vol. 51, pp. 20-27, 2013.

[84] A. L. Swindlehurst, E. Ayanoglu, P. Heydari, and F. Capolino, "Millimeter-wave massive MIMO: the next wireless revolution?," IEEE Communications Magazine, vol. 52, pp. 56-62, 2014.

[85] S. Wu, C. X. Wang, H. M. A. e, M. M. Alwakeel, and Y. He, "A Non-Stationary 3-D Wideband Twin-Cluster Model for 5G Massive MIMO Channels," IEEE Journal on Selected Areas in Communications, vol. 32, pp. 1207-1218, 2014.

[86] E. G. Larsson, O. Edfors, F. Tufvesson, and T. L. Marzetta, "Massive MIMO for next generation wireless systems," IEEE Communications Magazine, vol. 52, pp. 186-195, 2014.

[87] V. Jungnickel, K. Manolakis, W. Zirwas, B. Panzner, V. Braun, M. Lossow, et al., "The role of small cells, coordinated multipoint, and massive MIMO in 5G," IEEE Communications Magazine, vol. 52, pp. 44-51, 2014.

[88] N. Anand, R. E. Guerra, and E. W. Knightly, "The case for UHF-band MU-MIMO," in Proceedings of the 20th annual international conference on Mobile computing and networking, 2014, pp. 29-40.

[89] A. L. Swindlehurst, E. Ayanoglu, P. Heydari, and F. Capolino, "Millimeter-wave

massive MIMO: the next wireless revolution?," Communications Magazine, IEEE, vol. 52, pp. 56-62, 2014.

[90] E. Larsson, O. Edfors, F. Tufvesson, and T. Marzetta, "Massive MIMO for next generation wireless systems," Communications Magazine, IEEE, vol. 52, pp. 186-195, 2014.

[91] C. Oestges, N. Czink, P. De Doncker, V. Degli-Esposti, K. Haneda, W. Joseph, et al., "Radio channel modeling for 4G networks," in Pervasive Mobile and Ambient Wireless Communications, ed: Springer, 2012, pp. 67-147.

[92] A. Torabi and S. A. Reza Zekavat, "MIMO channel characterization over random rough dielectric terrain," in Personal, Indoor, and Mobile Radio Communication (PIMRC), 2014 IEEE 25th Annual International Symposium on, 2014, pp. 161-165.

[93] R. Verdone and A. Zanella, Pervasive Mobile and Ambient Wireless Communications: COST Action 2100: Springer Science & Business Media, 2012.

[94] V. Degli-Esposti, D. Guiducci, A. de'Marsi, P. Azzi, and F. Fuschini, "An advanced field prediction model including diffuse scattering," Antennas and Propagation, IEEE Transactions on, vol. 52, pp. 1717-1728, 2004.

[95] A. Torabi and S. Zekavat, "Near-Ground Channel Modeling for Distributed Cooperative Communications," IEEE Transactions on Antennas and Propagation, vol. PP, pp. 1-1, 2016.

[96] M. I. Sancer, "Shadow-corrected electromagnetic scattering from a randomly rough surface," Antennas and Propagation, IEEE Transactions on, vol. 17, pp. 577-585, 1969.

[97] M. T. Hallikainen, F. T. Ulaby, M. C. Dobson, M. A. El-rayes, and L. k. Wu, "Microwave Dielectric Behavior of Wet Soil-Part 1: Empirical Models and Experimental Observations," IEEE Transactions on Geoscience and Remote Sensing, vol. GE-23, pp. 25-34, 1985.

[98] N. R. Peplinski, F. T. Ulaby, and M. C. Dobson, "Dielectric properties of soils in the 0.3-1.3-GHz range," IEEE Transactions on Geoscience and Remote Sensing, vol. 33, pp. 803-807, 1995.

[99] A. Stogryn, "Equations for Calculating the Dielectric Constant of Saline Water (Correspondence)," IEEE Transactions on Microwave Theory and Techniques, vol. 19, pp. 733-736, 1971.

[100] D. Singh, "Effect of soil moisture on microwave scattering for remote sensing," Sadhana, vol. 24, pp. 485-493, 1999.

[101] S. Saatchi and U. Wegmuller, "Modeling and measurement of microwave emission and backscattering from bare soil surfaces," 1992.

[102] H. Meikle, Modern radar systems: Artech House, 2008.

[103] J. Fuhl, A. F. Molisch, and E. Bonek, "Unified channel model for mobile radio systems with smart antennas," Radar, Sonar and Navigation, IEE Proceedings -, vol. 145, pp. 32-41, 1998.

[104] D. Lopez-Perez, M. Ding, H. Claussen, and A. H. Jafari, "Towards 1 Gbp-s/UE in Cellular Systems:Understanding Ultra-Dense Small Cell Deployments," Communications Surveys & Tutorials, IEEE, vol. PP, pp. 1-1, 2015.

[105] A. Torabi and S. A. Zekavat, "Directional Channel Modeling for Millimeter Wave Small Cell Access Points," to be published.

[106] T. Zwick, T. J. Beukema, and N. Haewoon, "Wideband channel sounder with measurements and model for the 60 GHz indoor radio channel," Vehicular Technology, IEEE Transactions on, vol. 54, pp. 1266-1277, 2005.

[107] X. Hao, V. Kukshya, and T. S. Rappaport, "Spatial and temporal characteristics of 60-GHz indoor channels," Selected Areas in Communications, IEEE Journal on, vol. 20, pp. 620-630, 2002.

[108] T. Manabe, Y. Miura, and T. Ihara, "Effects of antenna directivity and polarization on indoor multipath propagation characteristics at 60 GHz," Selected Areas in Communications, IEEE Journal on, vol. 14, pp. 441-448, 1996.

[109] Z. Hong, S. Venkateswaran, and U. Madhow, "Channel Modeling and MIMO Capacity for Outdoor Millimeter Wave Links," in Wireless Communications and Networking Conference (WCNC), 2010 IEEE, 2010, pp. 1-6.

[110] H. Zhang and U. Madhow, "Statistical modeling of fading and diversity for outdoor 60 GHz channels," presented at the Proceedings of the 2010 ACM international workshop on mmWave communications: from circuits to networks, Chicago, Illinois, USA, 2010.

[111] E. Torkildson, Z. Hong, and U. Madhow, "Channel modeling for millimeter wave MIMO," in Information Theory and Applications Workshop (ITA), 2010, 2010, pp. 1-8.

[112] S. Akoum, O. El Ayach, and R. W. Heath, "Coverage and capacity in mmWave cellular systems," in Signals, Systems and Computers (ASILOMAR), 2012 Conference Record of the Forty Sixth Asilomar Conference on, 2012, pp. 688-692.

[113] Z. Hang, R. Mayzus, S. Shu, M. Samimi, J. K. Schulz, Y. Azar, et al., "28 GHz millimeter wave cellular communication measurements for reflection and penetration loss in and around buildings in New York city," in Communications (ICC), 2013 IEEE International Conference on, 2013, pp. 5163-5167.

[114] D. Didascalou, M. Dottling, N. Geng, and W. Wiesbeck, "An approach to include stochastic rough surface scattering into deterministic ray-optical wave propagation modeling," Antennas and Propagation, IEEE Transactions on, vol. 51, pp. 1508-1515, 2003.

[115] A. Torabi and S. A. Zekavat, "A Rigorous Model for Predicting the Path Loss in

Near-Ground Wireless Sensor Networks," to be presented at Vehicular Technology Conference (VTC Fall), 2015 IEEE 82th.

[116] A. K. Fung, W. Y. Liu, K. S. Chen, and M. K. Tsay, "An Improved Iem Model for Bistatic Scattering From Rough Surfaces," Journal of Electromagnetic Waves and Applications, vol. 16, pp. 689-702, 2002/01/01 2002.

[117] M. Steinbauer, A. F. Molisch, and E. Bonek, "The double-directional radio channel," Antennas and Propagation Magazine, IEEE, vol. 43, pp. 51-63, 2001.

[118] G. S. Brown, "Scattering from randomly rough surfaces and the far field approximation," Radio Science, vol. 18, pp. 71-81, 1983.

[119] E. S. Li and K. Sarabandi, "Low grazing incidence millimeter-wave scattering models and measurements for various road surfaces," Antennas and Propagation, IEEE Transactions on, vol. 47, pp. 851-861, 1999.

[120] S. Saunders and A. Aragn-Zavala, Antennas and propagation for wireless communication systems, 2nd ed.: John Wiley & Sons, 2007.

[121] S. G. Larew, T. A. Thomas, M. Cudak, and A. Ghosh, "Air interface design and ray tracing study for 5G millimeter wave communications," in Globecom Workshops (GC Wkshps), 2013 IEEE, 2013, pp. 117-122.

[122] M. Kyro, S. Ranvier, V. Kolmonen, K. Haneda, and P. Vainikainen, "Long range wideband channel measurements at 81-86 GHz frequency range," in Antennas and

Propagation (EuCAP), 2010 Proceedings of the Fourth European Conference on, 2010, pp. 1-5.

[123] W. Chao and Z. Xiaojuan, "Second-Order Perturbative Solutions for 3-D Electromagnetic Radiation and Propagation in a Layered Structure With Multilayer Rough Interfaces," Selected Topics in Applied Earth Observations and Remote Sensing, IEEE Journal of, vol. 8, pp. 180-194, 2015.

[124] W. Chao, Z. Xiaojuan, and F. Guangyou, "Bistatic Scattering From Three-Dimensional Layered Structures With Multilayer Rough Interfaces," Geoscience and Remote Sensing Letters, IEEE, vol. 11, pp. 676-680, 2014.

[125] K. Chih-hao and M. Moghaddam, "Scattering From Multilayer Rough Surfaces Based on the Extended Boundary Condition Method and Truncated Singular Value Decomposition," Antennas and Propagation, IEEE Transactions on, vol. 54, pp. 2917-2929, 2006.

[126] K. Chih-hao and M. Moghaddam, "Electromagnetic Scattering From Multilayer Rough Surfaces With Arbitrary Dielectric Profiles for Remote Sensing of Subsurface Soil Moisture," Geoscience and Remote Sensing, IEEE Transactions on, vol. 45, pp. 349-366, 2007.

[127] X. Duan and M. Moghaddam, "Bistatic Vector 3-D Scattering From Layered Rough Surfaces Using Stabilized Extended Boundary Condition Method," Geoscience and Remote Sensing, IEEE Transactions on, vol. 51, pp. 2722-2733, 2013.

[128] H. J. Eom and W. M. Boerner, "Scattering from a Layered Medium Connected with Rough Interfaces: Matrx Doubling Method," Geoscience and Remote Sensing, IEEE Transactions on, vol. GE-24, pp. 937-939, 1986.

[129] G. Franceschetti, P. Imperatore, A. Iodice, D. Riccio, and G. Ruello, "Scattering From Layered Structures With One Rough Interface: A Unified Formulation of Perturbative Solutions," Geoscience and Remote Sensing, IEEE Transactions on, vol. 46, pp. 1634-1643, 2008.

[130] Y. Goykhman and M. Moghaddam, "Retrieval of Parameters for Three-Layer Media with Nonsmooth Interfaces for Subsurface Remote Sensing," International Journal of Antennas and Propagation, vol. 2012, 2012.

[131] P. Imperatore, A. Iodice, and D. Riccio, "Transmission Through Layered Media With Rough Boundaries: First-Order Perturbative Solution," Antennas and Propagation, IEEE Transactions on, vol. 57, pp. 1481-1494, 2009.

[132] P. Imperatore, A. Iodice, and D. Riccio, "Electromagnetic Wave Scattering From Layered Structures With an Arbitrary Number of Rough Interfaces," Geoscience and Remote Sensing, IEEE Transactions on, vol. 47, pp. 1056-1072, 2009.

[133] P. Imperatore, A. Iodice, and D. Riccio, "Physical Meaning of Perturbative Solutions for Scattering From and Through Multilayered Structures With Rough Interfaces," Antennas and Propagation, IEEE Transactions on, vol. 58, pp. 2710-2724, 2010.

[134] P. Imperatore, A. Iodice, and D. Riccio, "Volumetric-Perturbative Reciprocal Formulation for Scattering From Rough Multilayers," Antennas and Propagation, IEEE Transactions on, vol. 59, pp. 877-887, 2011.

[135] P. Imperatore, A. Iodice, and D. Riccio, "Second-Order Volumetric-Perturbative Reciprocal Scattering Theory," Antennas and Propagation, IEEE Transactions on, vol. 60, pp. 1505-1520, 2012.

[136] P. Imperatore, A. Iodice, and D. Riccio, "Consistency and Validity of Perturbative Formulations for Scattering From Rough Multilayers," Antennas and Propagation, IEEE Transactions on, vol. 60, pp. 2019-2027, 2012.

[137] A. Tabatabaeenejad and M. Moghaddam, "Bistatic scattering from three-dimensional layered rough surfaces," Geoscience and Remote Sensing, IEEE Transactions on, vol. 44, pp. 2102-2114, 2006.

[138] A. Tabatabaeenejad and M. Moghaddam, "Inversion of Subsurface Properties of Layered Dielectric Structures With Random Slightly Rough Interfaces Using the Method of Simulated Annealing," Geoscience and Remote Sensing, IEEE Transactions on, vol. 47, pp. 2035-2046, 2009.

[139] A. Tabatabaeenejad and M. Moghaddam, "Study of Validity Region of Small Perturbation Method for Two-Layer Rough Surfaces," Geoscience and Remote Sensing Letters, IEEE, vol. 7, pp. 319-323, 2010.

[140] A. Tabatabaeenejad, D. Xueyang, and M. Moghaddam, "Coherent Scattering of Electromagnetic Waves From Two-Layer Rough Surfaces Within the Kirchhoff Regime," Geoscience and Remote Sensing, IEEE Transactions on, vol. 51, pp. 3943-3953, 2013.

[141] M. C. Vuran and I. F. Akyildiz, "Channel model and analysis for wireless underground sensor networks in soil medium," Physical Communication, vol. 3, pp. 245-254, 12// 2010.

[142] I. F. Akyildiz and E. P. Stuntebeck, "Wireless underground sensor networks: Research challenges," Ad Hoc Networks, vol. 4, pp. 669-686, 11// 2006.

[143] I. F. Akyildiz, Z. Sun, and M. C. Vuran, "Signal propagation techniques for wireless underground communication networks," Physical Communication, vol. 2, pp. 167-183, 9// 2009.

[144] K. Y. Yazdandoost and K. Sayrafian-Pour, "Channel model for body area network (BAN)," IEEE P802, vol. 15, 2009.